Astronomy Unit
School of Physics and Astronomy
Queen Mary University of London

Particle acceleration with associated generation and absorption of electromagnetic radiation in solar plasmas

Roman Pechhacker

Supervised by David Tsiklauri

Submitted in part fulfilment of the requirements for the degree of
Doctor of Philosophy (PhD)
of the University of London

Declaration

I, Roman Pechhacker, confirm that the research included within this thesis is my own work or that where it has been carried out in collaboration with, or supported by others, that this is duly acknowledged below and my contribution indicated. Previously published material is also acknowledged below.

I attest that I have exercised reasonable care to ensure that the work is original, and does not to the best of my knowledge break any UK law, infringe any third party's copyright or other Intellectual Property Right, or contain any confidential material.

I accept that the College has the right to use plagiarism detection software to check the electronic version of the thesis.

I confirm that this thesis has not been previously submitted for the award of a degree by this or any other university.

The copyright of this thesis rests with the author and no quotation from it or information derived from it may be published without the prior written consent of the author.

Roman Pechhacker
March 25^{th}, 2014.

Publications

The work and findings accumulated during the course of the PhD have been published in the following refereed journal papers:

- D. Tsiklauri and R. Pechhacker, *Heating of solar chromosphere by electromagnetic wave absorption in a plasma slab model*, Phys. Plasmas 18, 042901 (2011).
- R. Pechhacker and D. Tsiklauri, *Electron cyclotron maser emission mode coupling to the z-mode on a longitudinal density gradient in the context of solar type III bursts*, Phys. Plasmas 110702 (2012).
- R. Pechhacker and D. Tsiklauri, *The effect of electron beam pitch angle and density gradient on solar type III radio bursts*, Phys. Plasmas 19, 112903 (2012).
- R. Pechhacker and D. Tsiklauri, *Three dimensional particle-in-cell simulations of electron acceleration by Langmuir waves in an inhomogeneous plasma*, Phys. Plasmas 21, 012903 (2014).

Research and results have been presented at the following conferences:

- National Astronomy Meeting 2011 (Talk)
- International School/Symposium for Space Simulations 2011 (Poster)
- SEPNET Meeting 2011 (Talk)
- National Astronomy Meeting 2012 (Poster)
- SEPNET Meeting 2012 (Talk)
- Royal Astronomical Society Meeting 2012 (Talk)
- American Geophysical Union Fall Meeting 2012 (Poster)
- European Geophysical Union Meeting 2012 (Poster)
- National Astronomy Meeting 2013 (Talk)

Abstract

The heating of solar chromospheric internetwork regions is investigated by means of the absorption of electromagnetic (EM) waves that originate from the photospheric black body radiation. It is studied in the framework of a plasma slab model. The absorption is provided by the electron-neutral collisions in which electrons oscillate in the EM wave field and electron-neutral collisions damp the EM wave. It is shown that for plausible physical parameters, the absorbed heating flux is between 20% and 45% of the chromospheric radiative loss flux requirement.
Further, 1.5D particle-in-cell simulations of a hot, low density electron beam injected into magnetized, Maxwellian plasma were used to further explore the alternative non-gyrotropic beam driven EM emission mechanism, which was first studied in Ref.[83]. Variation of beam injection angle and background density gradient showed that the emission is caused by the perpendicular component of the beam injection current, whereas the parallel component only produces Langmuir waves, which play no role in the generation of EM waves in our mechanism. When the beam is injected perpendicularly to the background magnetic field, any electrostatic wave generation is turned off and a purely EM signal is left.
Finally, a possible solution to the unexplained high intensity hard x-ray emission observable during solar flares was investigated via 3D particle-in-cell simulations. A beam of accelerated electrons was injected into a magnetised, Maxwellian, homogeneous and inhomogeneous background plasma. The electron distribution function was unstable to the beam-plasma instability and was shown to generate Langmuir waves, while relaxing to plateau formation. Three different background plasma density gradients were investigated. The strong gradient case produced the largest fraction of electrons beyond $15v_{th}$. Further, Langmuir wave power is shown to drift to smaller wavenumbers, as found in previous quasi-linear simulations.

Acknowledgements

I would like to acknowledge the help of my supervisor, David Tsiklauri, who was a reliable source of knowledge and advice throughout the course of my PhD, showed great support and kept my laziness in check. I would like to thank the Queen Mary University of London and its staff for the support I received. My gratitude goes to Christopher T. Haynes, who has been an inspiration and a great friend for over three years. Special thanks go to Joseph R. Findlay for welcoming me so warmly to London and succeeding in making me feel at home.
This work was funded by the South East Physics Network (SEPNET).

To the friends I gained and the one I lost.

Contents

List of Figures

1 Introduction

1.1 The Sun

The Sun is the star that is located at the heart of the Solar System. Its diameter, $d_\odot$, is roughly 109 times that of the earth ($d_\odot = 1.39 \times 10^6$ km) while its mass is ≈ 330000 times that of the Earth ($m_\odot = 1.989 \times 10^{30}$ kg). It is the most massive object in the solar system, accounting for about 99% of the total mass. It consists for the most part ($\approx$ 98%) of hydrogen and helium, with only traces of heavier elements like oxygen, carbon, etc. On investigation, the Sun reveals an onion-like structure, therefore, it can be divided into layers, see Fig.1.1.

1.1.1 Solar Interior

Starting from the inside, the *core* is a very dense but comparably small region where nuclear fusion processes generate energy from combining hydrogen nuclei to helium at temperatures of the order of 10^7 K. The dominant process for nuclear burning is the proton-proton (pp) chain. The released energy does not only provide heating, but it is also responsible for radiation from the Sun. Beyond the core, in the *radiative zone* energy is transported outward by means of radiative diffusion, where photons that are emitted by ions travel only a short distance before they are absorbed by another ion, only to be re-emitted again at a lower energy. Above this layer, there is the *convection zone*, where the transport of energy happens through convection. This happens because great temperature gradients and lesser degrees of ionization make convective energy transfer favourable over radiative. Convection occurs when the temperature gradient exceeds the adiabatic gradient. Effectively, a hot volume of material rises into higher layers, where it is surrounded by cooler material. Hence, it continues ascending, expanding and cooling accordingly. Those convective motions can be observed on the surface in the form of granules and supergranules. On top of the convection zone, there is what is perceived to be the surface of the sun, the *photosphere*. By the top of photosphere, the temperature has dropped down to ≈ 6000 K. The photosphere shows almost a perfect black body radiation spectrum

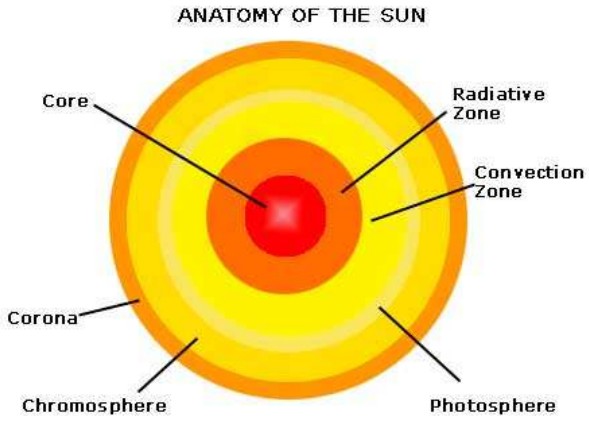

Figure 1.1: Solar structure qualitatively.
Source: *http://www.astronomyknowhow.com/sun.htm*

and is responsible for the generation of the majority of visible light that is emitted from the Sun.

1.1.2 Solar Atmosphere

Layers beyond the photosphere can collectively be called *solar atmosphere*. It consists of the *chromosphere*, the *transition region* and the *solar corona*. The chromosphere deserves its name due to its prominent emission line spectrum. The brightest line - the 656.3 nm H_α line - gives the chromosphere its reddish colour. However, it is generally outshone by the sheer brightness of the photosphere and can only be (easily) observed during a total eclipse. It is in the photosphere that the temperature profile of the Sun shows a minimum, but then increases with distance from the core throughout the chromosphere and transition region. The outer region of the solar atmosphere is called corona. Magnetic fields that reach out far beyond the photosphere often form structures which are referred to as coronal loops. These loops often extend up to ≈ 100 Mm out into the heliosphere. During eclipses these structures can be observed most easily and have lead to the name of corona (=crown). Temperatures in the corona can be of the order of 10^6 K. There are many theories on what kind of mechanism is responsible for this increase in temperature. We will discuss these in more detail in chapter 2. The Sun also releases a constant flow of particles into the heliosphere; the *solar wind*. It consists mainly of electrons and protons that have sufficient energies to escape the solar atmosphere. The mass outflow is supersonic with respect to the speed of sound within the solar wind.

1.1.3 Solar Magnetic Field

The solar magnetic field is believed to be generated by a magnetic dynamo, situated in a region between radiative and convection zone. This layer is called the *tachocline*, where radiative and convective energy transfer zones come into contact. The differentially rotating tachocline causes great shear, which gives rise to an electric current that drives the solar magnetic field. This process is called *solar dynamo*. The structure of the magnetic field is highly complex, but some regularities and effects can be studied. For example, sunspots are areas of lesser brightness on the photospheric surface. They are believed to be a result of locally increased magnetic field strength, which inhibits convection and therefore the energy transfer, creating a spot of reduced temperature, hence, lesser brightness. Usually, sunspots come in pairs of opposite polarities. Interestingly, the magnetic field's polarity changes every 11 years. This is referred to as the Hale's law and a full 22 year cycle is accordingly named Hale cycle. With a change of direction comes an increased solar activity, noticeable for example in the amount of observable sunspots. The next solar maximum is supposed to occur at the time of the completion of this thesis, namely in autumn of 2013.

1.2 Solar Observations

The Sun can be observed in a broad range of frequencies (respectively wavelengths). Most relevant to the effects studied in this thesis are *Solar Flares* and accompanying phenomena. Solar flares are characterized as events of sudden high brightness in a region on the solar surface or the solar limb, see Fig.1.2. The brightening in the spectrum is associated with an strong increase in energy release. This is known to happen particularly around sunspots, where strong magnetic fields are able to build a 'bridge' from the solar interior to the corona. The strong field strengths and complex structures of the magnetic field can trigger magnetic reconnection, which causes the sudden release of energy associated with a solar flare. Mainly the energy is released either in form of radiation or ejection of vast clouds of mass, so called coronal mass ejection (CME). In the latter scenario, the flare ejects a large amount of electrons and ions into the heliosphere. These particles can travel all the way to the Earth's magnetosphere, evoke geomagnetic storms and cause major disruptions in the electricity and/or satellite networks, etc. The radiation generated in correlation with solar flares spans from the radio frequency spectrum, over visible

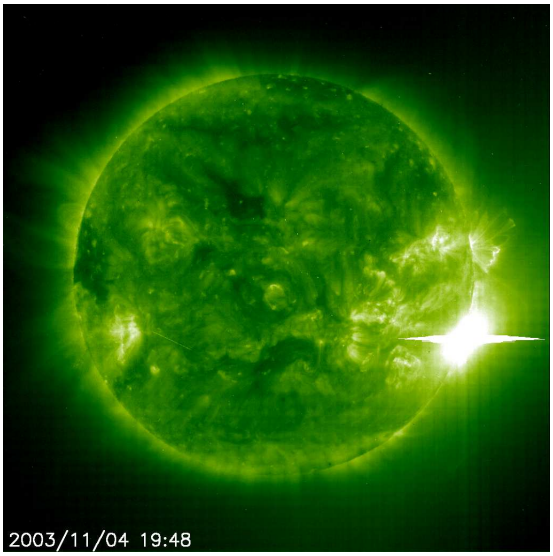

Figure 1.2: Solar flare on November 4^{th} 2003. Taken by SOHO's Extreme ultraviolet Imaging Telescope. Horizontal white line is not real.
Source : Ref.[57]

light and x-rays to gamma rays. This makes it necessary to observe solar activity in a variety of instruments in order to gain insight into the physics at play among all orders of frequencies and wavelengths. The complex structure and dynamics of the solar interior result in many interesting phenomena, which can be observed both terrestrial telescopes and instruments in outer space. Waves of large enough wavelength are able to penetrate the Earth's atmosphere and can be observed with ground based devices. Radio waves fulfil that requirement and their signatures are being monitored in multiple locations around the earth. For example, the Low Frequency Array (LOFAR) was completed in 2012. It consists of a network of sites that are located in the UK, the Netherlands, Germany, France, and Sweden. Solar physics is only one aspect of the LOFAR project, others being cosmic magnetism, ultra high energy cosmic rays, transients and pulsars, etc [43]. Further examples of ground based radio telescopes around the globe are the Nancay Radioheliographe (NRH) in France, the Owens Valley Solar Array (OVSA) in California, USA, or the Siberian Solar Radio Telescope (SSRT) in Russia, and others. In order to observe radiation of wavelengths that are too short to pass through the earth's atmosphere, telescopes need to be placed into space. In this thesis, particular interest is taken in hard x-ray radiation in the context of solar flares (see chapter 5). Spacecraft missions that have contributed observations in the relevant frequency bands are e.g. the Reuven Ramaty High Energy Solar Spectral Imager (RHESSI), the Solar and He-

liospheric Observatory (SOHO), Yohkoh, and the Nuclear Spectroscopic Telescope Array (NuSTAR).
The hostile environment of the solar atmosphere makes it very difficult to dive into the star and perform any measurements 'inside' the Sun. However, the upcoming *Solar Probe Plus* mission will be aiming at diving into the outer regions of the solar corona to take samples of the local plasma in order to shed light on some of the unsolved puzzles of solar physics; e.g how is the solar corona heated? or what accelerates the solar wind? [57]

1.3 Solar Radio Bursts

One of the most significant phenomena that accompany solar flares are radio bursts. These refer to events that are often observed together with or shortly after flares and show characteristic emission spectra in the radio frequency range. Generally, they can be categorized by the way the emission frequency develops over time as well as by what they are caused by (see Fig.1.3). The timescales on which solar radio manifest range from seconds to several days and often occur in bunches.

Not all known radio bursts occur in association with solar flares, however. *Type I Bursts* are sources of radio emission with brightness temperatures (= the temperature a black body is required to have, in order to emit radiation of a similar intensity) of the order of 10^{7-9} K. They are sometimes also called 'noise storms' and not subject to be triggered by a flare going off in the burst vicinity. Typically, they occur in magnetic loops that connect active regions of the Sun to the quieter ones. They are thought to be caused by electrons being accelerated to energies of few keV. Type I bursts can last for days at a time and are the most common type of radio bursts.
Type II Bursts are results of outward travelling shock waves. These are much shorter lived than type I bursts and can last up to minutes. Type IIs tend to result from solar flares or CMEs, however the exact correlation is still subject to ongoing debate. There is accepted evidence for a connection to chromospheric Moreton waves [56] as well as coronal transient waves (so-called EIT-waves) [47]. The shock front pushes material ahead, accelerating particles in the process. If the shock travels fast enough, the accelerated electrons trigger the bump-on-tail plasma instability, which results in electrostatic Langmuir wave growth. Subsequently, the generated Langmuir waves can be converted into electromagnetic waves via nonlinear Landau

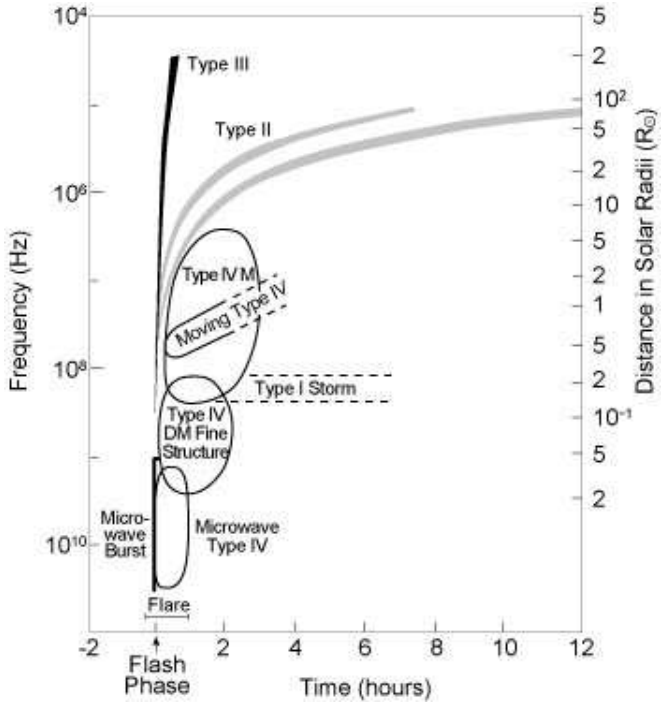

Figure 1.3: Categorization of solar radio bursts.
Source: Ref.[39]

damping (where Langmuir waves scatter off thermal ions, shifting the wave power to smaller wavenumbers/higher phase velocities and can even be scattered backwards either step-wise or in just one step [50], donating energy to the thermal background) or non-linear wave-wave interactions [27] including Langmuir waves (L), backscattered Langmuir waves (L'), ion-acoustic waves (S), and transverse electromagnetic waves (T). The possible conversions are

$$\begin{aligned} L &\longrightarrow T(f_{pe}) \pm S \\ L &\longrightarrow L' \pm S \\ L + L' &\longrightarrow T(2f_{pe}) \end{aligned}$$

where f_{pe} denotes the electron plasma frequency and its harmonic $2f_{pe}$. Type II dynamical spectra (frequency over time graphs) show a characteristic drop of frequency at a rate of ≈ 1 MHz/s over a span of $10^2 - 10^5$ kHz with the harmonic usually being the stronger emission. The drop of the observed frequency happens due to the fact that the plasma frequency is proportional to the square root of the plasma density. As the shock front pushes material outward, the density drops along the propagation path, hence, the frequency of the generated waves drop accordingly.

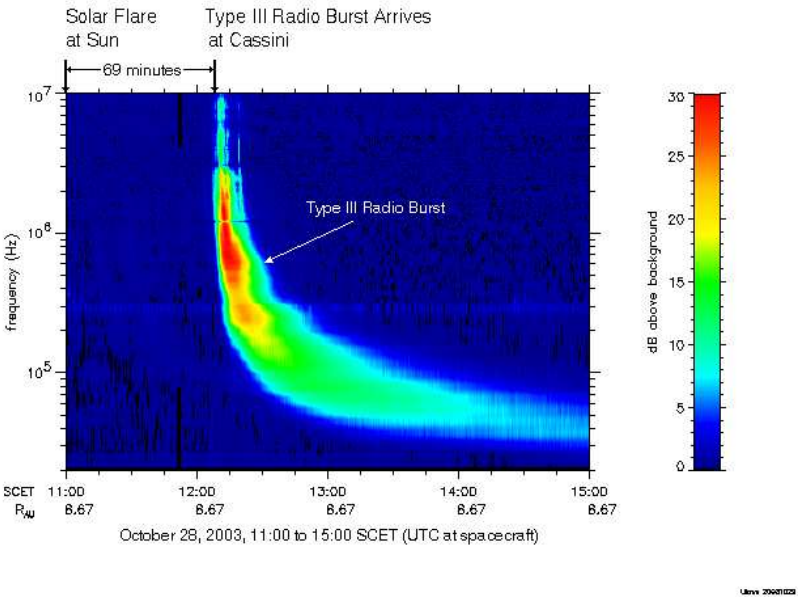

Figure 1.4: Characteristic dynamical spectrum of a type III burst.
Source: *http://www-pw.physics.uiowa.edu/space-audio/typeIII.html*

Type III bursts are at the center of attention in chapters 3 and 4 of this thesis. They can occur singly or in groups of many in active regions and solar flares. Similarly to type IIs, their dynamical spectra show a frequency drift to lower frequencies and a presence of the second harmonic. However, for type III bursts this drift happens at much faster timescales (100 MHz/s) and stretches over a broader bandwidth of frequencies of 10 kHz up to 8 GHz. This can be explained by the fact that type III bursts are being caused by accelerated electrons of velocities $0.2 - 0.6$c. The fast particles race outwards through the solar atmosphere on open magnetic field lines emitting electromagnetic waves in the process. Conventionally, there are three main ways in which the resulting electromagnetic emission escapes. All rely on the fact that the fast electrons trigger a plasma instability (bump-on-tail or beam-plasma instability) to generate Langmuir waves, which in turn trigger EM emission as described above in the case of type IIs. In chapters 3 and 4 these mechansims are briefly reviewed and another alternative mechanism that does not require Langmuir wave generation is introduced and explored.

J-Type, U-Type and RS Bursts are analogous to type III bursts, in the sense that they are being driven by beams of accelerated electrons. However, the name U-type burst stems from the characteristic U-shape of the dynamical spectrum. As the type III burst only shows a drop of frequency over time, the U-type shows a 'U'.

This is due to the fact that in this case, the electron beam propagates along closed magnetic field lines, i.e. loops that initially lead the beam away from the coronal base, but then back into the solar atmosphere. In the case that the beam releases all its energy along the stream path and it ceases to cause EM emission before it reaches the foot point of a loop, the dynamical spectrum will show not a full 'U', but a 'J', hence, J-type burst. A burst that travels strictly downwards shows a reversed slope (RS) and is referred to as RS burst.
Type IV bursts manifest themselves as continuum radiation that is very broad-band and usually follow a flare. The emitted radiation is strongly polarized, pulsating and shows fine structures (also called 'zebra stripes'). The frequency range of the observed emission is $20 - 2000$ MHz. The emission mechanism is not fully understood yet, but is thought to involve electrons trapped in magnetic clouds. Consequently, the trapping of the energetic electrons is expected to cause gyro-synchrotron emission. Type IV bursts can last from minutes to days.
Type V Bursts are short-lived (up to few minutes) bursts of continuum radiation in sequence of a type III burst. They never appear in isolation. Emission frequencies are around $10 - 200$ MHz.

1.4 Solar Radio Emission

Radio emission from the Sun is not restricted to solar flares. Sources of radio waves range from the quiet Sun to flares, coronal mass ejections and even interplanetary particles. Generation mechanisms of radio waves can generally be divided into two categories, distinguished by whether the emission is *coherent* or *incoherent*. Coherent emission is generated by kinetic plasma instabilities that arise from unstable particle distributions. Such distributions include cases where the electron velocity distribution function $f(v_\parallel, v_\perp)$ shows a positive slope either a) in forward direction (i.e. along the magnetic field), $\partial f/\partial v_\parallel > 0$, or b) in perpendicular direction, $\partial f/\partial v_\perp > 0$. The former corresponds to the aforementioned bump-on-tail or beam plasma instabilities resulting from electron beams and is generally referred to as *plasma emission*, the latter gives rise to the *electron cyclotron maser* (ECM) instability that are triggered by e.g. losscone, ring, or Dory-Guest-Harris distributions (for example see Ref.[92]), which occur for example through mirroring in a magnetic trap geometry. In the previous section, the theory behind plasma emission from the bump-on-tail and beam-plasma instabilities was discussed. The ECM instability will be dealt with in more detail in chapters 3 and 4, while the beam plasma instability

is investigated in chapter 5. There, it is also shown that a beam of electrons that shows a perpendicular velocity component may also trigger the ECM instability. The beam plasma instability is investigated in the context of hard x-ray emission from solar flares in chapter 5. Most coherent emission mechanisms occur in flares, where processes of particle acceleration allow for a sufficient number of electrons being accelerated to high enough energies in order to achieve the necessary shapes in distribution functions. The generated emission then acts back on the particle distribution via wave-particle interactions, pushing it towards stability and eventually quenching the instability and, hence, wave growth. The unstable particle distributions are altered such that the positive gradients are minimized and eventually a plateau is formed and the growth requirements are no longer met.
Incoherent radio emission mechanisms may be distinguished into emission from a) thermal electrons, which cause *free-free emission* (bremsstrahlung) or b) *gyroemission* (gyroresonance and gyrosynchrotron). Bremsstrahlung is a result of a deflection of an test particle (e.g. electron) in the Coulomb field of field particles (e.g. ions), due to the Coulomb force acting on the test particle. Since, in a plasma both the electron as well as the ions can be considered free particles, the resulting emission is referred to as free-free emission. If both the test particle and the field particle are of the same thermal distribution the bremsstrahlung is referred to as *thermal* and is detectable in soft x-ray spectra. *Nonthermal* bremsstrahlung can occur when the test particles are either accelerated to high energies in a collisionless plasma and then encounter a collisional thermal plasma (*thick-target bremsstrahlung*), or are steadily accelerated in a collisional plasma (*thin-target bremsstrahlung*). Nonthermal bremsstrahlung produces emission in the microwave and hard x-ray spectra. Gyroemission results from the fact that magnetic fields cause charged particles to gyrate around magnetic field lines. The circular motion enforced by the Lorentz force is an acceleration of a charged particle, which causes gyroresonance emission in the non-relativistic case (Lorentz $\gamma \approx 1$), gyrosynchrotron emission in the mildly relativistic case ($1 > \gamma > 3$), and synchrotron emission for highly relativistic particles. For gyroemission, the emission does not act back onto the particle. In this way it differs from coherent emission mechanisms, where the generated emission triggers wave-particle interactions, which change the shape of the particle distribution function. In order to be significant, gyroemission requires high magnetic field strengths, which can be found near sunspots, making gyroemission the dominant mechanism for emission generation in those regions. Gyrosynchrotron emission, stems from mildly relativistic particles, which are common in flares, because particle acceleration mechanisms achieve a sufficient number of electrons in order for the

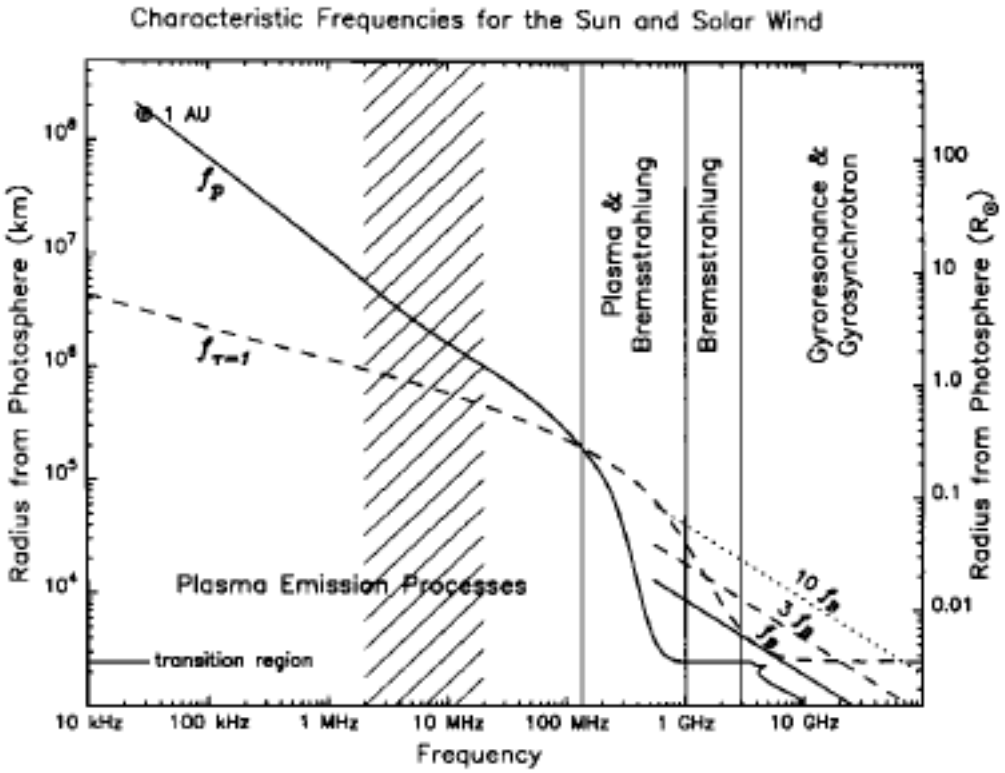

Figure 1.5: Schematic of dominance of various kinds of radio emission types as a function of frequency for the Sun and solar wind. Taken from Ref.[25].

emission intensity to be significant compared to other observable types of emission. The thermal free-free emission dominates in quite Sun regions, coronal holes, and prominences. It is also present in active regions, but due to the dominant brightness of emission from solar flares, free-free emission from active regions can only be observed in the absence of flares. Subsequently, emission from the quite Sun can only be observed in the absence of active regions.

Fig.1.5 (taken from Ref.[25]) shows the dominance of the various radio emission mechanisms as a function of the plasma frequency $f_p(h)$ at height h, ranging from ≈ 1 GHz in the transition region to ≈ 30 kHz at around 1 AU. The optically thick layer, $\tau = 1$, was also modelled and shows that the corona is optically thick up to few 100 MHz. Gyroemission at the gyrofrequency and its harmonics dominates for high frequencies up to ≈ 70 GHz (gyrosynchrotron harmonics $s < 10$).

1.5 Particle Acceleration Mechanisms in Solar Flares

The previous section discussed mechanisms for generation of radio emission from thermal and nonthermal particle distributions. Observations show that large parts of the emission in solar flares result from nonthermal particles, i.e. particles that have been accelerated out of the background thermal particle distribution. This section tackles the question of how particles can be accelerated in flares and aims to give an overview of the main mechanisms. This question and relevant models have been discussed extensively in the literature, e.g. [2, 12, 14, 22, 99]. Traditionally, the presence of accelerated particles in flares has been inferred from hard x-ray (HXR), gamma-ray and radio frequency observations as well as detection of solar energetic particles directly in space. Acceleration is not restricted to electrons. The acceleration of ions is known to be proportional in the relativistic regime [72]. Ref.[64] discusses observational data acquired by the Reuven Ramaty High Energy Solar Spectroscopic Imager (RHESSI). Flares release energies in the range of $10^{20} - 10^{25}$ J. The HXR signature dominates at the start of a flare and shows impulsive character. The distribution function shows a power law tail above 10 keV, allowing electrons to reach relativistic values. HXR emission is predominantly generated at the footpoints of magnetic field structures (coronal loops). The thick target model, discussed in the previous section, offers a plausible explanation for the generation of the emission, reasoning that the electrons are accelerated in an approximately collisionless coronal loop, stream downwards towards the footpoints, where they encounter a collisional regime that eventually generates the characteristic emission. This effect will be discussed in more detail in chapter 5. Gamma-ray emission was also found in loop footpoints, but is generally attributed to high energy ions. Soft x-rays peak a few seconds after the HXR, which hints at a slower/gradual acceleration mechanism.

Acceleration mechanisms can be divided into a) DC electric field acceleration, b) stochastic acceleration, and c) shock acceleration. *DC electric field acceleration* mechanisms cover a variety of mechanisms, which generate a electric field that accelerates charged particles via the Lorentz force. Such fields may be realized in current sheets in magnetic reconnection processes or current carrying loops. An electric field will accelerate particles of different sign into different directions. However, the Coulomb force will counter this acceleration, leading to the equation of motion, $dv/dt = eE/m_e - \nu_{ei}v$, for an electron travelling at the velocity v, with unit

charge e, electron mass m_e and electron-ion collision frequency ν_{ei}. For large relative velocities the effect of the drag force (Coulomb force) can be overcome and particles are accelerated away from one another and out of a thermal distribution (runaway). The critical electric field is referred to as the Dreicer Field. In super-Dreicer DC electric fields all particles with velocities higher than the thermal velocity, $v > v_{th}$, are accelerated, while in sub-Dreicer fields only particles of $v > v_{th}[E/E_D]^{1/2}$, with the Dreicer field E_D, gain energy. Sub-Dreicer fields are rather weak and require large scales, which imposes an issue of stability of the geometry (current sheet tearing modes) as well as the temporal evolution of the acceleration process.

Magnetic reconnection is thought to be the prime mechanism of energy release in solar flares. Vast amounts of energy are stored in the magnetic structure of the solar corona. The idea of magnetic reconnection is that previously independent magnetic field lines suddenly connect to reshape the magnetic field topology. In this process, free energy that was stored in the magnetic field is released and can accelerate particles. The coronal magnetic field is strong and the magnetic energy can build up over a long time, only to be released in a sudden reconnection event, causing the bursty feature of a solar flare. Competing models for the description of the physics of a magnetic X-point in a 2D geometry are the Sweet-Parker model, which describes the formation of an elongated current sheet, and the Petschek model, which involved a much smaller diffusion region around the x-point. In the Sweet-Parker model close, oppositely directed field lines are associated with plasma inflows in perpendicular direction to the field lines. The increasing magnetic pressure is relieved by reconnection in a small region on the plane of field reversal. This allows plasma to leave the diffusion region towards the sides and current sheet formation. However, this model predicted a rather slow reconnection rate, $v_i/v_A \propto 1/R_m \ll 1$ (with reconnection rate v_i, Alfven speed v_A and magnetic Reynolds number R_m), which was later improved in the Petschek model. The Petschek model described the escape of shocks from the diffusion region, reducing its size and increasing the reconnection rate, $v_i \approx v_A$, considerably compared to the Sweet-Parker model.

Stochastic acceleration processes consider particle acceleration from wave-particle interactions. Contrary to the effect discussed above, here acceleration happens via an AC field of waves in plasmas. Particularly efficient energy transfer from wave to particle occurs when the wave frequency is close to in resonance with a particle's gyromotion. Due to the abundance of waves and the broad spectrum of frequencies, some waves will act constructively on the particle population, while others will not. This introduces a randomness to the process. If some part of the particle population are resonant with a part of the wave spectrum, they receive a net gain

in energy. This process is called stochastic acceleration. As previously mentioned, wave-particle interactions can also be triggered from coherent emission mechanisms, where an unstable distribution function triggers wave growth, that acts back on the initial distribution. In the theory of stochastic acceleration the evolution of the particle distribution function can be expressed in a Fokker-Planck equation, that is coupled to the evolution of the wave photon spectrum. The energization term in the case of solar flares can be governed by plasma wave turbulence [29] or cascading MHD-turbulence [55]. Ref.[29] shows that an imposed level of plasma wave turbulence on a plasma can accelerate ambient particles stochastically and - for flare parameters - thermal background electrons reach the necessary high energies within the short time scales observed in HXR observations. The acceleration is most efficient at low energies and very strong magnetic fields. MHD-turbulence refers to fast-mode MHD waves travelling through plasma. The associated magnetic compressions act as scattering centres. The wavelength cascades from large to small until wave dissipation due to transit-time damping becomes dominant. Neighbouring waves may be in resonance and cause energy change, which may cause resonance with yet another wave etc [55]. Electrons can, hence, be accelerated from thermal up to relativistic speeds just by a sequence of resonant interactions with fast-mode waves. The main point of criticism for stochastic models is the assumption of pre-existing wave modes, which are necessary to kickstart simulations. The level of turbulence as well as the efficiency of the MHD-turbulence cascading effect are assumptions that have to be made in order to reproduce observed spectra.

Shocks are the driving force behind type II bursts. In this case, the shock front travels strictly outward and generates the characteristic frequency drop in the observed emission. However, type II bursts are only one example of particle acceleration by shocks. Shocks are waves with nonlinear amplitudes and propagation speeds that exceed the ambient sound speed. It is possible to generate slow- and fast-mode waves in the outflowing regions of reconnection sites during magnetic reconnection, which could be of high relevance for particle acceleration in solar flares. Fermi described the shock acceleration as a collision of a particle with a de facto magnetized cloud that acts as a magnetic mirror. Depending on how often the shock wave interacts with the particle, one distinguishes between single encounters (first-order Fermi acceleration) or multiple encounters (second-order/diffusive Fermi acceleration).

1.6 EPOCH

Computational modelling is a necessary tool in almost any field of plasma physics. The complexity of plasmas and its governing equations are often found to be beyond fully analytical calculations. Numerical models are able to make accurate predictions for plasma systems and with ever increasing processor powers and data storage space, numerical simulations of plasmas are becoming ever more precise and closer to a real system. Generally, there are two different ways of describing a plasma: i) fluid descriptions (e.g. Magneto-Hydro-Dynamics MHD, multi-fluid description, etc), which treats the plasma as one would treat a fluid; ii) kinetic descriptions, which either a) solve kinetic Vlasov or Fokker-Planck equations or b) take the approach of self-consistently solving Maxwell's equations for particles and electromagnetic fields and their interaction. A distinction from test particle simulations needs to be drawn. In the test particle case, the equation of motion of the test particles is governed by background electromagnetic fields, however, the fields generated by the test particles do not act back on the background fields. The kinetic approach to computational plasma physics tends to be more expensive than a fluid one, however, it allows investigation of many phenomena that remain inaccessible for fluid codes. For example, the effects treated in chapters 3, 4, and 5 of this thesis cause wave generation from plasma instabilities (e.g. beam-plasma instability, electron cyclotron maser instability), which are caused by non-Maxwellian electron velocity distribution functions. The distribution function in fluid codes always remains Maxwellian. Therefore, if one needs to describe particle acceleration or study the generation of radio emission that involves plasma micro-instabilities that necessarily demand deviations from Maxwellian distributions, a kinetic plasma description is needed. The correct choice of code generally depends on the problem one is investigating. MHD or multi-fluid codes solve mass, momentum and energy conservation equations of physically small volumes, ascribing to them bulk properties such as bulk velocity, density and pressure. Generally, a kinetic description is imperative when scales of spatial and temporal variation of the problem approach kinetic scales such as electron or ion inertial lengths, Debye length, or plasma/cyclotron frequencies.

Plasma simulations in this work are carried out with EPOCH. EPOCH is a fully relativistic particle-in-cell (PIC) code, which falls in the category of kinetic codes. In the PIC method, the population of real physical particles is represented by a (much smaller) number of computational pseudoparticles. The motion of these pseudoparticles is then calculated by their interaction with external electromagnetic fields on a finite difference time domain technique on a spatial grid. First, the fields are de-

termined from the pseudoparticles' positions and motions. Then the forces that are being generated by these fields are applied to the pseudoparticles, updating their velocities. Lastly, the new velocities are used to determine the new pseudoparticle positions. This scheme is repeated for every timestep. The code uses Boris' scheme [7, 10] for advancing the particles together with the charge conserving method by Esirkepov [20] for calculating the currents. The shape function of the particles, and thus the order of the weighting scheme, can be chosen between tophat (second order), triangular (third order), and spline interpolation (5th order). The electromagnetic fields are solved using the finite difference time domain (FDTD) algorithm on a Yee grid [76, 95].

1.7 Thesis Outline

This thesis is structured as follows:
In chapter 2, the chromospheric heating problem is tackled. A slab model of the solar plasma is introduced. Absorption, reflection and transmission coefficients are calculated and applied to solar parameters. Chapter 3 deals with solar type III radio bursts. It investigates the role of the perpendicular component of the momentum of an electron beam on the produced electromagnetic emission. The emission mechanism is studied by 1.5D PIC simulations. In chapter 4, a parametric study is performed in order to determine the effect of the background density gradient and beam pitch angles on the emission. Chapter 5 treats the acceleration of electrons from generation of Langmuir waves in the context of the unexplained large amount of high energy x-ray (HXR) radiation from solar flares. 3D PIC simulations of a mono-energetic beam injected into a maxwellian homogeneous and inhomogeneous plasma are performed. The background density gradient is varied in order to estimate its importance in the role of electron acceleration.

2 Heating of the Solar Chromosphere

The main findings of this chapter have been published in Ref.[86].

2.1 Introduction

The problem of heating of the solar atmosphere - the sharp temperature rise from photospheric 6000K to few 10^6K in the corona - has been a long standing problem of solar physics. There is no lack of possible heating mechanisms in the *corona* with the two main candidates being so-called direct current (DC) models that are based on magnetic reconnection and alternating current (AC) models that are based on magnetohydrodynamic (MHD) wave dissipation [2], alongside with few dozen other, less widely accepted [70, 82] or less successful ones [81]. In the *chromosphere*, however, until recently, a general agreement was that it is heated by the absorption of acoustic waves. A distinction needs to be drawn between wave heating of different parts of the chromosphere. The chromosphere of the quiet Sun can be broadly split into two parts: (i) the magnetic network, which marks the boundaries in between the super-granulation cells; and (ii) the inter-network regions, which constitute the bulk surface area of the chromosphere (i.e. the super-granulation cell interiors).

In the magnetic network the magnetic field is nearly radial (vertical) and quite strong (of the order of few kG). Since the strong magnetic field there provides a substantial amount of free energy, in principle it seems reasonable to believe that the magnetic network can be heated by the dissipation of MHD waves [30]. However, the role of magnetic reconnection in the heating of the magnetic network cannot be discounted. For example, there seems to be an evidence of forced magnetic reconnection taking place in the photosphere [33], as well as in chromosphere [15]. The estimates of the heating flux produced by plausible reconnection models seem to fall short by up to two orders of magnitude from the quiet chromosphere and coronal heating requirements [44]. At the same time Ref.[30] and other similar

works, that base their conclusions on the numerical simulation results, do not make precise predictions for the heating rates produced by the dissipation of MHD waves in the chromospheric magnetic network.

The situation with the heating of inter-network regions where magnetic fields are weak is even worse than with the magnetic network. On one hand, this is because of the lack of the magnetic energy. On the other hand, the results of Ref.[23] indicate that the acoustic energy flux of the high-frequency (10-50 mHz) acoustic waves (that were previously believed to constitute the dominant heating mechanism of the chromosphere) falls short, by a factor of at least ten, to balance the radiative losses in the solar chromosphere. This led them to a conclusion that the acoustic waves cannot constitute the dominant heating mechanism of the solar chromosphere. This conclusion has been challenged by Ref.[34], who suggests that the observations reported by Ref.[23] only detect 10% of the acoustic wave flux perhaps because of the limited spatial resolution. Ref.[5] report somewhat higher than usual flux carried by the acoustic waves at photospheric heights (250 km) as well as compile a useful list of up to date acoustic heating flux measurements.

In this context, in this work we explore an alternative to the acoustic wave heating idea of the quiet chromosphere. In particular, we investigate the following proposition:

(i) It is known that the solar irradiance spectrum, that comes out of photosphere, is well approximated by an effective blackbody at a temperature of $T = 5762$ K, in the frequency range of $f = 30 - 1667$ THz (corresponding to the wavelengths range of $10 - 0.18$ μm) (see e.g. Figure 2.3 from Ref.[2]). Therefore, we assume that the radiative heating flux with the Planckian brightness distribution as a function of frequency penetrates the lower part of the solar atmosphere (photosphere, $h = 0 - 500$ km and chromosphere, $h = 500 - 2200$ km).

(ii) Instead of solving radiative transfer equations, we take the photospheric blackbody flux of $T = 5762$ K, and quantify how much electromagnetic (EM) radiative flux is absorbed using a plausible model for EM wave absorption, which is based on Ref.[77] plasma slab model combined with the VAL-C model of the chromosphere [88]. The Ref.[77] plasma slab model is based on splitting a smoothly varying, non-uniform density, weakly ionised plasma with the uniform magnetic field along the density gradient, into a set of thin sub-slabs with a uniform density in each sub-slab - thus providing a discretized version of the smooth density profile. The absorption of the EM radiation is based on two physical effects: electron-neutral collisions and electron cyclotron resonance. For the considered radial magnetic field value of 0.2 kG, electron cyclotron frequency is $f_{ce} = eB/2\pi m_e = 0.00056$ THz. Also, for the

considered model parameters, the ratio of electron-neutral collision frequency and electron cyclotron frequency, $\nu_{en}/f_{ce} << 1$, which ensures that the collisions would not affect any electron cyclotron resonance damping. Therefore EM wave absorption via electron cyclotron resonance is negligibly small in the considered range of frequencies $2 - 2000$ THz. We refer the interested reader to Ref.[77] for the details of the plasma slab model. However, we re-iterate the key points of the model in Section 2.

As a result we find that for plausible physical parameters, the heating flux produced by the absorption of EM waves in the chromosphere is between $20 - 45$ % of the VAL-C radiative loss flux requirement. We also establish that a collision cross-section of 5×10^{-18} m^2 produces the maximal heating flux of 1990 Wm^{-2}.

This chapter is organised as follows: In Section 2 we describe the model. In Section 3 we present the numerical results and we close with the Conclusions in Section 4.

2.2 The model

The interaction of EM wave with a plasma slab has been a subject of a number of studies see e.g. Ref.[77], references therein, and a more recent work [98].

Following the general approach of Ref.[77], we consider a slab that contains 22 sub-slabs each having thickness of 100 km. In each sub-slab density and temperature are assumed to be uniform, but these vary as we go from one slab to the next. This variation is prescribed by the VAL-C model [88]. This way, in the first slab, that corresponds to the 50 km above photospheric level, we have temperature of T=5840 K, neutral hydrogen number density $n_H = 9.203 \times 10^{22}$ m^{-3}, electron number density of $n_e = 2.122 \times 10^{19}$ m^{-3}. In the final 22nd slab, that corresponds to the 2200 km above photospheric level the plasma parameters are T=24000 K, $n_H = 1.932 \times 10^{16}$ m^{-3}, $n_e = 2.009 \times 10^{16}$ m^{-3}. In between these values we use linear interpolation for the thermodynamic parameters. The uniform magnetic field with $B = 0.02$ T (0.2 kG) is directed through all sub-slabs in the vertical (radial) direction. We use a relatively small value of B that is commensurate with the chromospheric internetwork regions. However, we note that the model outcomes (such as e.g. the resultant EM wave absorption) depend weakly on the magnetic field value used (at least in the plausible range of variation of the field in the chromosphere). Also the fact that the magnetic field is vertical describes the quiet Sun reasonably well. Ref.[74] found no evidence for any predominance of horizontal fields on the quiet Sun.

They find that (i) the angular distribution of the field varies steeply with flux density. (ii) For the largest flux densities the distribution is extremely peaked around the vertical direction. (iii) For the smaller vertical flux densities the distribution widens to become asymptotically isotropic in the limit of zero flux density. The apparent dominance of horizontal fields for flux densities below 5 G is shown to be an artifact of noise.

Our representation of the number density and temperature variation in the photosphere and chromosphere by means of uniform sub-slabs is valid when the variation of those quantities over the height of a slab is small, i.e. for temperature $\Delta T/T << 1$, where ΔT is the change of temperature from one slab to the next. This is indeed the case in the photosphere and chromosphere (we exclude the transition region and corona from our consideration, also on the grounds that the dispersion relation that we use below is applicable for *weakly* ionised plasma). The expression for the complex dielectric constant for the weakly ionised, magnetised plasma with the angle between the propagation direction of the incident EM wave and the magnetic field B, $\theta = 0$ is taken from Ref.[77]:

$$\tilde{\varepsilon}_r = 1 - \frac{\omega_{pe}^2/\omega^2}{[1 - i\nu_{en}/\omega] \pm \omega_{ce}/\omega}. \tag{2.1}$$

Here $\omega_{pe} = \sqrt{n_e e^2/(\varepsilon_0 m_e)}$, $\omega_{ce} = eB/m_e$ and ν_{en} (see Eq.2.7 below for the definition) are the electron plasma frequency, electron cyclotron angular frequency and electron-neutral collision frequency, respectively. The angular frequency ω of the EM harmonic is related to the frequency, f, in the usual way $\omega = 2\pi f$. The sign $\pm$ refers to the left- and right-hand polarisation of the EM wave and i is the imaginary unit. The EM wave reflection coefficient at the $(k+1)$th sub-slab interface is given by

$$\Gamma(k+1) = \frac{\sqrt{\tilde{\varepsilon}_r(k)} - \sqrt{\tilde{\varepsilon}_r(k+1)}}{\sqrt{\tilde{\varepsilon}_r(k)} + \sqrt{\tilde{\varepsilon}_r(k+1)}}. \tag{2.2}$$

One can calculate the reflected and transmitted power, P_r and P_t, respectively, using formulae:

$$\begin{aligned} P_r(f) &= P_i(f)\Bigg[|\Gamma(1)|^2 + \\ &\sum_{j=2}^{22}\left(|\Gamma(j)|^2 \prod_{i=1}^{j-1}\left[e^{-4\alpha(i)d}\left(1 - |\Gamma(i)|^2\right)\right]\right)\Bigg] \end{aligned} \tag{2.3}$$

$$P_t(f) = P_i(f) \prod_{i=1}^{22} \left[e^{-2\alpha(i)d} \left(1 - |\Gamma(i)|^2\right)\right], \tag{2.4}$$

where P_i is the incident EM wave power, d is the sub-slab thickness and $\alpha(i)$ is the real part of the complex propagation constant of a plane wave in a magnetised plasma corresponding to slab i

$$\alpha(i) = \frac{\omega}{c} \mathrm{Re}\left[\sqrt{-\tilde{\varepsilon}_r(i)}\right] = \frac{\omega}{c}\sqrt{\frac{|\tilde{\varepsilon}_r(i)| - \mathrm{Re}[\tilde{\varepsilon}_r(i)]}{2}}. \tag{2.5}$$

Note that Eqs.2.1-2.4 are identical to the corresponding equations from Ref.[77]. As in Ref.[77] we neglect the effect of multiple reflections of waves, i.e. each wave gets reflected at a maximum of one slab interface; however, it may be absorbed in any location.

The total absorbed power, P_a is then given by

$$P_a(f) = P_i(f) - P_r(f) - P_t(f). \tag{2.6}$$

Note that for $\theta = 0$ the above expressions for the reflection, transmission and absorption coefficients are independent of the EM wave polarisation, except for the $\pm$ sign in Eq.2.1 for the left- and right-hand polarisation of the EM wave (see e.g. Ref.[31], pp. 71-94). A simple numerical code was written to calculate the above absorbed, reflected and transmitted EM power. We have tested the code by successfully reproducing Figures 1-9 from Ref.[77], using their set of physical parameters.

The above formulae contain the electron-neutral collision frequency ν_{en}. For the latter we use the standard expression from Ref.[32], p.39,

$$\nu_{en} = n_0 \sigma \sqrt{kT_e/m_e}, \tag{2.7}$$

where n_0 is the neutral number density, σ is the collision cross-section and the square root is essentially the electron thermal speed. For n_0 we use values of neutral hydrogen number density n_H in each sub-slab, and for T_e we use the temperature T; both according to the VAL-C model. Thus, in each presented numerical model run we regard σ as fixed. However, since ν_{en} is a function of density and temperature, each sub-slab has its own set value.

In order to calculate the absorbed EM flux we use equal 1/2 statistical weights of the left- and right-hand polarised EM wave total absorbed powers $P_{a,L}$ and $P_{a,R}$ as following

$$P_a(f) = \frac{1}{2} P_{a,L}(f) + \frac{1}{2} P_{a,R}(f). \tag{2.8}$$

Thus, the total absorbed EM flux can be calculated using the following integral

$$F_a[\mathrm{Wm}^2] = \pi \int_{\mathrm{f_{min}}}^{\mathrm{f_{max}}} \mathrm{A(f)B_f(f)df}, \tag{2.9}$$

where $B_f(f)$ is the Planck function $B_f(f) = 2hf^3/\left[c^2(\exp[hf/(kT)] - 1)\right]$ and $A(f)$ is the total absorption coefficient as a function of frequency given by the following expression

$$P_a(f) = P_i(f)A(f). \tag{2.10}$$

2.3 Results

The dissipation coefficients in the solar atmosphere are not known precisely. There are good reasons to believe that the dissipation coefficients, such as resistivity and viscosity, which in turn depend on plasma species mutual collision cross-sections and collision frequencies (including ν_{en}), have so-called "anomalous" values. The "anomaly" is in the sense of their departure (mostly increase) from the classical (laminar) plasma transport theory values. It is believed that the anomalous dissipation coefficients result from the plasma micro-turbulence. The latter provides additional centres of scattering for the plasma particles in addition to their mutual collisions. In the theory of turbulence (e.g. [9]) scattering centres arise from perturbations created from smooth flow. These perturbations may be interpretted as plasma instabilities that develope on small scales and their effects. For example, the Kelvin-Helmholtz instabilty may be triggered from velocity gradients within a plasma flow. While the frozen-in condition of the magnetic field is often fulfilled in plasmas, finite resistivity may free the flow from the field just enough to cause small scale perturbations. In the solar photosphere and chromosphere, the dominant effect is thought to be the tearing mode [24, 40]. In effect this means that in Eq.2.7 we should use $\sigma = \sigma_{en} + \sigma_{turbulent}$, i.e. the effective anomalous cross-section is a sum of usual electron-neutral and turbulent plasma cross-sections. Note that $\sigma_{en} \approx 5 \times 10^{-19}$ m^2 and is weakly dependent on temperature [32]. Little is known about the $\sigma_{turbulent}$ apart from it can be orders of magnitude larger than σ_{en}. Since the theory of plasma micro-turbulence is not complete, we simply vary the collision cross-section σ in Eq.2.7 by a few orders of magnitude, in order to study the effects of anomalous dissipation coefficients on the quiet chromosphere heating. We start presentation of the results by plotting, in Fig.2.1, the EM wave absorption coefficient, $A(f)$, as a function of frequency for various values of σ. The considered

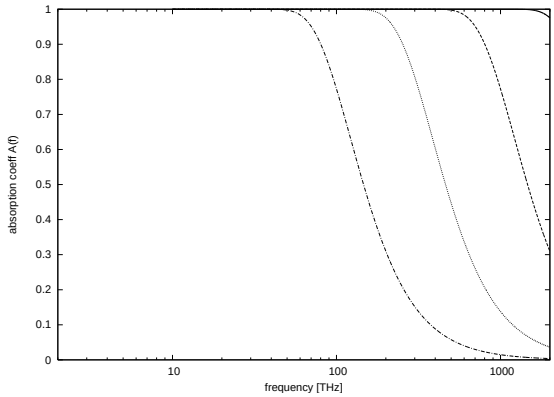

Figure 2.1: Absorption coefficient $A(f)$ is a function of EM wave frequency f for different values of the cross-section σ. Solid line corresponds to $\sigma = 5 \times 10^{-16}$ m^2, dashed $\sigma = 5 \times 10^{-17}$ m^2, dotted $\sigma = 5 \times 10^{-18}$ m^2, dot-dashed $\sigma = 5 \times 10^{-19}$ m^2.

frequency range is commensurate with the range $f = 30 - 1667$ THz where the solar irradiance spectrum, that comes out of photosphere, is well approximated by an effective blackbody at $T = 5762$ K (see e.g. Figure 2.3 from Ref.[2]).

We gather from Fig.2.1 that (i) a decrease in σ generally results in an overall reduction of the absorption coefficient; and (ii) different frequencies are absorbed differently - high frequencies show weaker absorption than low ones. As to the observation (i), the explanation can be provided by analysing by Eqs. 2.1 - 2.4. It is clear from Eqs. 2.3 and 2.4 that the electron-neutral collision frequency ν_{en} provides the only dissipation effect. The exponential factor $e^{-\alpha d}$ dominates the heat flux absorption. For the considered model parameter range, it can be shown by calculating $\partial\alpha/\partial\nu_{en}$ derivative numerically that $\partial\alpha/\partial\nu_{en} > 0$. Therefore one can deduce that the heat flux absorption decreases with the decrease in cross-section. As to the observation (ii), a possible physical explanation could be that when the frequency of the EM radiation is increased, electrons due to their small but finite inertia do not have time to catch up with (i.e. couple to) the EM wave. Hence the EM wave frequency increase results in a decrease of the absorption coefficient.

In Fig.2.2 we show the behaviour of the integrand of Eq.2.9, $\pi A(f)B_f(f)$, which has a physical meaning of the absorbed EM flux density (i.e. flux per unit frequency) as a function of frequency for various values of σ. We observe that due to the frequency dependence of $B_f(f)$ that has a peak, the absorbed EM flux density is also peaked. The two conclusions that follow are: the decrease in the cross-section results in (i) the overall reduction of the the absorbed EM flux density; and (ii) shift of the absorbed EM flux density's peak towards the smaller frequencies.

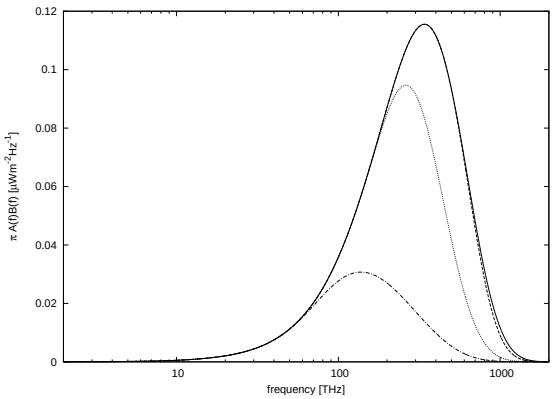

Figure 2.2: The absorbed EM flux density, $\pi A(f)B_f(f)$, as a function of frequency for various values of σ. Solid line corresponds to $\sigma = 5{\times}10^{-16}$ m^2, dashed $\sigma = 5 \times 10^{-17}$ m^2, dotted $\sigma = 5 \times 10^{-18}$ m^2, dot-dashed $\sigma = 5 \times 10^{-19}$ m^2.

Next we calculate the volumetric heating rate produced by the absorption of the EM waves. Above we have presented the behaviour of the total absorption coefficient and the absorbed EM flux density for the full set of 22 slabs as a function of frequency. We obtained the expression for the total absorbed flux by integrating over the relevant interval of frequencies using Eq.2.9. In order to obtain the distribution of the absorbed EM energy as a function of height, we perform a numerical differentiation of the calculated total absorbed flux values. The differentiation yields the heating rate $H(k)$ in slab k,

$$H(k) = \frac{F_a(k) - F_a(k-1)}{d} \tag{2.11}$$

where the $F_a(k)$ are calculated by ignoring the existence of slabs above slab number k.

In Fig.2.3 we plot the heating rate for the different values of σ as a function of height above the photosphere. Clearly, the model predictions for the heating rate fall short in matching the empirical radiative loss calculated by the VAL-C model of the chromosphere. We gather that (i) the heating rate decreases rapidly with height; and (ii) in the region of 500 km - 2200 km above photosphere there is an optimal value for σ that produces a maximal heating rate. The latter is evidenced by the fact that $\sigma = 5 \times 10^{-18}$ m^2 (dotted) curve is above the both $\sigma = 5 \times 10^{-17}$ m^2 (long-dashed) and $\sigma = 5 \times 10^{-19}$ m^2 (dot-dashed) curves. Note that the model predictions for the heating rate presented in Fig.2.3 underestimate the actual heating rate produced by the absorption of EM waves. This is due to the following reasons: (i) an error

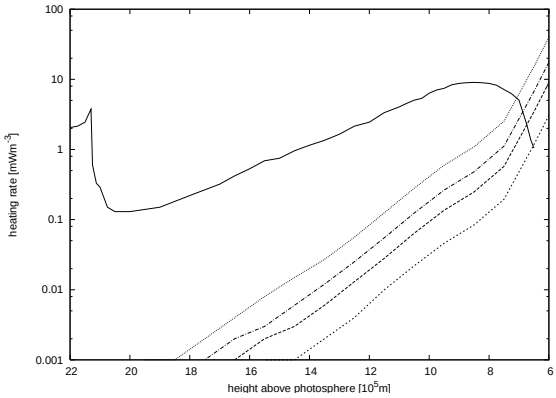

Figure 2.3: The heating rate for the different values of σ as a function of height above photosphere. The VAL-C empirical model (solid); the next four curves are calculated using Eq.2.11 $\sigma = 5 \times 10^{-17}$ m^2 (long-dashed), $\sigma = 5 \times 10^{-18}$ m^2 (dotted), $\sigma = 5 \times 10^{-19}$ m^2 (dot-dashed), $\sigma = 5 \times 10^{-20}$ m^2 (short-dashed).

introduced by the numerical differentiation with respect to height (it is known that the numerical differentiation always introduces the numerical diffusion); and (ii) ignoring the contribution to the absorption due to reflected waves. The former is unavoidable, while the latter can be regarded as a shortcoming of our heating rate calculation. Our motivation for calculating the (volumetric) heating rate as a function of height was to compare our model predictions to the results of VAL-C empirical radiative cooling rate (see their Figure 49). Naturally, we can improve our calculation by *directly* calculating the total heating flux of the chromosphere. We do this by applying Eq.2.9 for all 22 sub-slabs that cover entire the photosphere and chromosphere (heights of $0 - 2200$ km) and then subtracting contribution from the first 5 photospheric sub-slabs ($0 - 500$ km), because we are concerned only with the chromosphere. Such *heating flux* [Wm^{-2}] calculation is free from the above two sources of the underestimation that arose in the calculation of the *(volumetric) heating rate* [Wm^{-3}]. Further, the most exact calculation of the total absorbed EM flux is as follows:

In order to extract the total absorbed flux of a slab interval $[a; b]$, we have to account for the possibility of waves being reflected at an interface higher up than slab b and being absorbed within the interval on their way back. In the following we will use the notation $A|_a^b$ for the absorption coefficient of a plasma slab bounded by slabs number a and b, both included in the interval. Further we define

$$A|_a^b = 1 - R|_a^b - T|_a^b \tag{2.12}$$

where $R|_a^b$ and $T|_a^b$ represent reflection and transmission coefficients of the interval and can be calculated by Eq.2.3-2.4. At this point we stress that by using Eq.2.3-2.4 we neglect the effect of multiple reflections of waves, meaning that each wave gets reflected at a maximum of one slab interface, however may be absorbed in any location. Further we define that only coefficients that follow $1 \leq a \leq b \leq N$, where N is the total number of slabs, are non-zero. First we consider the case $a = 1$ and b arbitrary. We write for the absorption coefficient

$$A|_1^b = A|_1^N - A|_{b+1}^N T|_1^b \tag{2.13}$$

where the last term on the right hand side accounts for absorption of waves within layers higher up than slab b that have passed through the interval. Extending the formalism to arbitrary a it holds true that

$$A|_a^b = A|_1^N - A|_{b+1}^N T|_1^b - A|_1^{a-1} - T|_1^{a-1} R|_a^N (A|_1^{a-1})^* \tag{2.14}$$

where

$$(A|_1^{a-1})^* = 1 - T|_1^{a-1} = 1 - \prod_{i=1}^{a-1} \left[e^{-2\alpha(i)d}\right]. \tag{2.15}$$

The factor $(A|_1^{a-1})^*$ accounts for the absorbed radiation within the interval $[1; a-1]$ but neglects the multiple reflections. We gather from Eq.2.14 that we have added a term that gives absorptions at layers lower than a and another term that accounts for waves that have initially been transmitted through those lower layers, then get reflected at higher levels and absorbed below level a on their way back down.

The results of the these calculations, inserting $N = 22$, $a = 6$ and $b = 22$, are shown in Fig.2.4, where we plot the total absorbed EM flux as a function of σ. We gather from Fig.2.4 that (i) there is an optimal value for $\sigma = 5 \times 10^{-18}$ m^2 that produces the maximal heating flux of 1990 Wm^{-2}. The latter is about 45 % of the chromospheric radiative losses; (ii) For the value of $\sigma = 5 \times 10^{-19}$ m^2 that is predicted by the classical (laminar) plasma transport theory [32], which ignores contribution from the plasma-microturbulent transport, the total heating flux by the absorption of EM waves in the chromosphere our model predicts 880 Wm^{-2}. Which is only 20% percent of the heating flux requirement of 4280 Wm^{-2} [88]. Since precise value of σ is unknown due to a lack of the detailed plasma-microturbulent transport theory, we conclude that the actual heating flux produced by the absorption of EM waves in the chromosphere is between $20-45$ % of the VAL-C radiative loss flux requirement. Note that the behaviour described in Fig.2.4 that the heating flux has a maximum

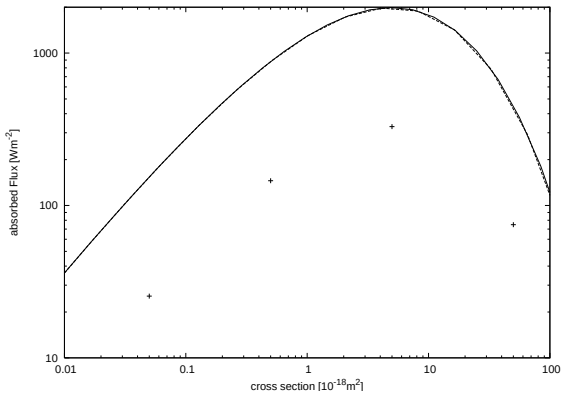

Figure 2.4: The total absorbed EM flux as a function of σ. The solid curve corresponds to the precise calculation according to Eq.2.14. The dashed curve corresponds to the the calculation by applying Eq.2.9 for all 22 sub-slabs that cover entire photosphere and chromosphere (heights of $0-2200$ km) and then subtracting the contribution from the first 5 photospheric sub-slabs ($0-500$ km). Four crosses correspond to the area under the long-dashed, dotted, dot-dashed and short-dashed curves in Fig.2.3 that cover chromospheric heights between 6th and the 22nd sub-slabs $500-2200$ km.

when plotted as a function of cross-section σ is true when only chromospheric sub-slabs $6-22$ are considered (i.e. when contribution from the photospheric sub-slabs $1-5$ is not included). We also remark that the difference between the solid curve that corresponds to the precise calculation according to Eq.2.14 and the dashed curve that corresponds to the the calculation by applying Eq.2.9 for all 22 sub-slabs that cover entire photosphere and chromosphere (heights of $0-2200$ km) and then subtracting the contribution from the first 5 photospheric sub-slabs ($0-500$ km) is rather small and barely distinguishable to the plotting accuracy. The close overlap of the two curves is an indication of the last term in Eq.2.14 being negligibly small. This term accounts for the radiation that is initially transmitted into slabs 6 and higher, reflected somewhere in the higher slabs and then again absorbed within the slabs 1-5. It is clear from Fig.2.3 that the absorption in the lower layers is higher compared to the upper ones. Hence, the last term in Eq.2.14 will not make a considerable contribution when the reflection and transmission coefficients $R|_a^N$ and $T|_1^{a-1}$ are sufficiently small, such that the overall product $T|_1^{a-1}R|_a^N(A|_1^{a-1})^*$ is negligible. For for the chromospheric parameters the last term in Eq.2.14 is negligibly small, thus the plotted curves in Fig.2.4 are barely distinguishable.

2.4 Conclusions

In this chapter we put to test a simple proposition that some of the problems of the chromospheric inter-network regions (regions with weak magnetic field which constitute the bulk of solar chromosphere surface), discussed in the Introduction section can be alleviated by inclusion of the absorption of photospheric EM radiation in the plasma sub-slab based model.

On one hand, we know that that the solar irradiance spectrum, that comes out of photosphere, is well approximated by an effective blackbody at a temperature of $T = 5762$ K, in the frequency range of $f = 30 - 1667$ THz. Therefore, we can assume that the radiative heating flux with the Planckian brightness distribution as a function of frequency illuminates lower part of the solar atmosphere (photosphere, $h = 0 - 500$ km and chromosphere, $h = 500 - 2200$ km).

On the other hand, instead of solving radiative transfer equations, we can take photospheric blackbody flux of $T = 5762$ K, and quantify how much electromagnetic (EM) radiative flux is absorbed using a plausible model for the EM wave absorption which is based on Ref.[77] plasma slab model combined with VAL-C model of chromosphere [88]. Our model is based on splitting a weakly ionised plasma slab with the uniform magnetic field along a smooth density gradient, into a set of narrow sub-slabs with a uniform density in each slab - hence providing a discretized version of the smooth density gradient. In the relevant frequency range ($2 - 2000$ THz), the absorption of the EM radiation is due to the electron-neutral collisions, while the electron cyclotron resonance can be ignored. The absorption of the EM radiation due to the electron-neutral collisions happens because the electrons oscillate in the EM wave field and electron-neutral collisions (i.e. their mutual friction) then results in the damping of the EM wave.

We also include a contribution to the cross-section from the anomalous plasma micro-turbulence, which we incorporate in an additive way.

Our model has two potential weaknesses: (i) to what extent the radiative heating flux of the photosphere deviates from the Planckian brightness distribution as a function of frequency? and (ii) whether the *absorption* of EM radiation can be described by the plasma sub-slab model which assumes local thermodynamic equilibrium (LTE)? Concerning the first question we state that it is well known that the solar irradiance spectrum, that comes out of photosphere, is well approximated by an effective blackbody at a temperature of $T = 5762$ K, in the frequency range of $f = 30 - 1667$ THz. Also, there are plausible models of solar photosphere that use LTE assumption (see e.g. Ref.[28]) that implies the applicability of the Planck-

ian brightness function. As to the second question we remark that indeed in order to properly work out the chromospheric (radiative) *losses*, one needs to consider non-LTE effects. Strong radiation field in the chromosphere can drastically alter the occupation numbers of the energy levels in atoms, thus producing non-LTE net radiative loss [54]. We assert, however, that the chromospheric *heating* process can be regarded as an LTE process, given the *steady* inflow of EM radiation from the photosphere. After all, the chromospheric heating models that are based on the absorption of acoustic shock wave energy use equations of hydrodynamics which imply LTE, and it is only the radiative *losses* that are treated by the non-LTE radiative transport as in e.g. Ref.[23].

It is known from thermodynamics that a hot body cannot be heated by a cold one via radiation. On first glance, this model may seem to violate the laws of thermodynamics, however, the assumptions of the photosphere acting as a blackbody radiator is justified, as well as the model of absorption within the chromosphere. It should be stressed that this model neglects the effect of re-emission of absorbed radiation, which is certainly not realistic, because radiation of frequencies that should be totally absorbed according to Fig.2.1 obviously escapes from the Sun. The model only takes into account the absorption of photospheric blackbody radiation in chromospheric plasma for different electron-neutral collision cross sections. The variation is due to the unknown level of turbulence in the solar chromosphere. However, it is known that turbulence may create additional scattering centres, which in turn enhance resistivity and, hence, absorption coefficients via triggering of resistivity and conductivity instabilities as well as tearing modes and magnetically trapped conductivity regions [8, 40]. The level of turbulence is difficult to estimate, as it is not directly accessible for measurements, thus a range of collision cross sections was investigated.

As a result we find that:

(i) for plausible physical parameters, the heating flux produced by the absorption of EM waves in the chromosphere is between $20-45$ % of the VAL-C model radiative loss flux requirement. The variation range is because of the uncertainties in the collision cross-section due to the plasma micro-turbulence.

(ii) We also established that for absorption in the region 500 km - 2200 km above photosphere there is an optimal value for $\sigma = 5 \times 10^{-18}$ m^2 that produces the maximal heating flux of 1990 Wm^{-2}.

From the observational point of view, if the absorption of EM waves in the frequency range $2 - 2000$ THz has a significant role to play in the heating of quiet chromosphere, as suggested by our findings, then the plasma slab model also pre-

dicts that:

(i) There is a good case for the electron-neutral anomalous collision cross-section to be a factor of 10 larger than the value predicted by the classical plasma transport. Ref.[80] presented plasma resistivity (which is proportional to both the collision frequency and cross-section) measurements in the reconnection current sheet of the Magnetic Reconnection Experiment. They established that in some regimes, the measured resistivity values can be more than an order of magnitude larger than the classical Spitzer value. Therefore it would seem likely that the collision cross-section in the chromosphere would also assume some anomalous value.

(ii) There should be a good correlation of the total solar irradiance with the Mg-index (which represents the chromospheric excess radiation relative to the photosphere) on a long-term (1 month or more) timescale. This is because our model takes photospheric blackbody EM wave flux as the source of energy, that irradiates chromosphere from below (a torch shining from the below analogy is relevant here). In fact, this is exactly what is observed: Ref.[73] presents the data that shows that the total solar irradiance and the Mg-index have a correlation coefficient of 0.8 using monthly data averages (see their Figure 1 and pertinent discussion). The correlation is somewhat worse of a shorter timescales, e.g. daily data averages – this has a good explanation in that contribution from the solar features such as sunspots and faculae (that affect photospheric total solar irradiance) and plages (that affect chromospheric brightness and are in fact mapped closely to the faculae below) average out on the long timescales and generally track to solar activity cycle (that has a proxy of number of sunspots).

(iii) Unlike in the photosphere, the chromospheric brightness should not decrease with the increase of the magnetic field. This is because in our model EM wave absorption depends on the magnetic field rather weakly. This is also what is observed: Ref.[69] find that CaII K line core contrast (the relative difference between the intensity at a given magnetogram and the quiet Sun intensity) that is a measure of chromospheric brightness is weakly increasing with the magnetic field as $\propto B^{0.6}$. In the photosphere the contrast of a continuum in the green part of the solar spectrum initially increases with B up to 0.02 T but then sharply decreases with B above 0.05 T. Ref.[73] explain chromospheric rise of brightness with the increase of magnetic field for small B's (0.01 T) is due to the density increase of the magnetic flux tubes, and for large B's (> 0.05 T) subsequent slower rise is due to the quenching of the wave activity. As Ref.[78] have shown, the strong magnetic fields inhibit average horizontal flow speeds in the granules. Thus in conclusion the plasma slab model predictions seem also to conform with the available observational data.

3 Electron Cyclotron Maser Emission Mode Coupling to the Z-Mode on a Longitudinal Density Gradient in the Context of Solar Type III Bursts

The main findings of this chapter have been published in Ref.[60].

3.1 Introduction

Electron beam injection is common in many plasma situations. Examples are solar flares [18], cavity magnetrons that generate microwaves [4, 89] or various radar applications. Beams of relativistic, hot electrons are also likely to be the source of solar type III radio bursts. In the common theory their parallel momentum is causing Langmuir wave growth through the 'bump-on-tail' instability, and subsequent electromagnetic (EM) wave generation (and emission) via three main possibilities 1) non-linear wave-wave interactions [27], 2) linear mode conversion on density gradients [36], and 3) the antenna mechanism [45]. Recently, particle-in-cell simulations have been carried out on this topic [67, 83]. The above mentioned mechanisms focus on the contribution of the parallel component of the beam momentum, however, in situations, where the beam is not completely aligned with the magnetic field, there is likely to be a contribution from the perpendicular component. It is conceivable that non-field aligned, unstable electron beam distributions are possible in the solar atmosphere under some conditions. In this case, a bump on the distribution function will form in the perpendicular direction of momentum space. If the bump is strong enough to achieve a positive slope, the cyclotron maser is triggered. The cyclotron

maser is known to generate EM emission in x-,o-, and z-mode, depending on the ratio of plasma frequency to electron gyrofrequency [92]. It has been studied by PIC simulations in the context of the auroral kilometric radiation in Ref.[63].

3.2 Electron Cyclotron Maser

Coherent radio emission stems from kinetic plasma instabilities that are caused by unstable particle velocity distribution functions. In cases where $\partial f/\partial v_\perp > 0$, electron cyclotron maser emission is possible. Adequately shaped distribution functions typically arise from energetic particles in magnetic traps, e.g. flare loop that show characteristics of magnetic mirrors above the footpoints due to diverging magnetic field with height. In particular, the electron cyclotron maser instability was attributed to be driving mechanism behind a number of observed radio emissions from astrophysical sources, such as the auroral kilometric radiation [52, 91, 93], solar microwave spike bursts [51, 71], and related bursts from flare stars and close binaries [17, 26]. In these examples, fast electrons are trapped in magnetic flux tubes and propagation into higher density areas causes loss of small pitch angle electrons, which can lead to a velocity distribution function that shows the necessary positive slope perpendicular to the magnetic field. If this is achieved, the positive slope provides free energy that may grow waves via gyroresonant wave-particle interactions, where the Doppler resonance condition, $\omega - s\omega_{ce}/\gamma - k_\parallel v_\parallel = 0$, (where ω is the angular wave frequency, ω_{ce} is the electron cyclotron frequency, s is an integer, γ is the Lorentz factor, and $k_\parallel$ the parallel wavenumber) is fulfilled. This condition expresses the relation of the wave vector to the particle gyromotion, i.e. $\omega = s\omega_{ce}$. The case $s = 0$ is referred to as Landau damping or Cerenkov resonance. Wave growth can occur in x-, o-, and z-mode. Which mode is excited, is determined by the ratio of electron plasma frequency to electron cyclotron frequency, and has been studied in the literature [53, 94]. For $\omega_{ce}/\omega_{pe} > 1/0.3$ growth in the x-mode at ω_{ce} is dominant, for $1/0.3 > \omega_{ce}/\omega_{pe} > 1$ growth can also occur in the o- and z-mode. For ratios $\omega_{ce}/\omega_{pe} < 1$ wave growth at the fundamental is largely suppressed and waves at harmonics s of ω_{ce} are excited. The growth rates of o- and x-modes decrease strongly for harmonics, moreover, there is no growth in o- and x-modes expected for ratios of $\omega_{ce}/\omega_{pe} < 1/1.7$. Therefore, in this regime - which is the regime considered in chapter 3 and 4 of this thesis - wave growth in the z-mode is favourable.

3.3 O-, X- and Z-Modes

O- and x-modes are solutions to the dispersion relations for magnetized plasmas and define possible relations of electromagnetic wave angular frequency ω to wavenumbers $k_{\parallel}$, $k_{\perp}$. Traditionally, the ordinary (O-) and extraordinary (x-) mode are labelled free space modes because of their ability to smoothly connect to free space. However, the x-mode consists of two branches, one called the free branch referred to as x-mode, the other being the z-mode (sometimes called the *slow branch*, as its propagation speed is limited to being less than the speed of light in vacuum). The term *z-mode* originates from ionospheric studies, where along with the well known ionospheric reflections caused by the o- and x-modes, there was also a further reflection found with polarization similar to the o-mode [6]. Fig.3.1 is representation

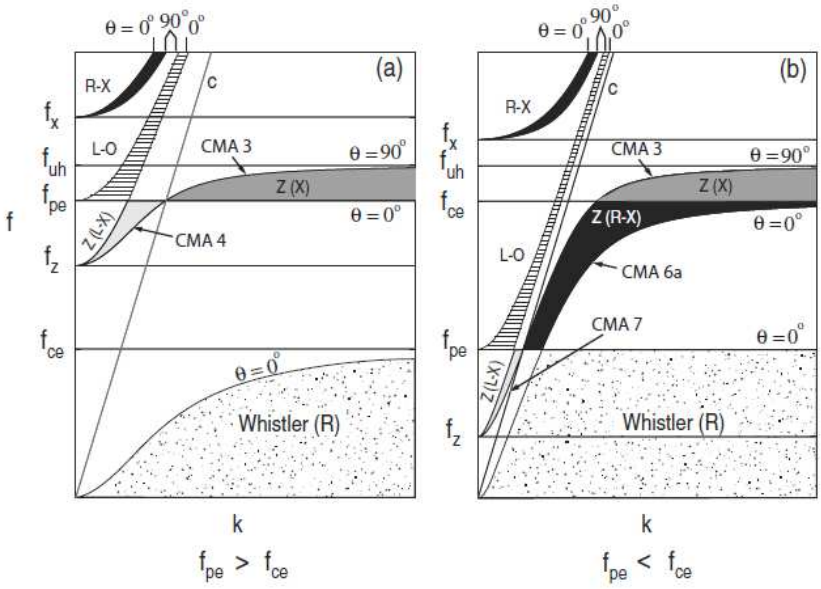

Figure 3.1: Modes in homogeneous, cold, magnetized plasma. Taken from Ref.[6]

of dispersion relations for a homogeneous, cold, magnetized plasma with $\omega = 2\pi f$. Qualitatively, lines in this figure correspond to propagation directions with $\theta = 0$ and $\theta = \pi/2$ with respect to the background magnetic field. The coloured/shaded areas (z-mode regions are labelled CMAs in accordance with Ref.[75]) in between the lines indicate existence of a mode (of oblique propagation). L and R correspond to left or right hand polarization along the magnetic field, X and O respectively for the perpendicular case. If only one letter is given (e.g. Z(X)), the cold plasma approximation does not allow for modes of the omitted polarization, i.e. in the Z(X) area, the cold plasma approximation predicts no waves that travel at $\theta = 0$,

however, in the hot case there may well be a possible mode along the magnetic field. It is evident from the figure that the z-mode is confined to frequencies between the z-mode cut-off $\omega_z = -\frac{1}{2}\omega_{ce} + \frac{1}{2}\sqrt{\omega_{ce}^2 + 4\omega_{pe}^2}$ and the upper hybrid frequency $\omega_{UH} = (\omega_{pe}^2 + \omega_{ce}^2)^{1/2}$. Fig.3.1 follows the cold plasma approximation and generally offers a good guide to dispersion relations in the ionosphere being successfully applied to a variety of ionospheric phenomena, despite the ionosphere being neither cold, nor homogeneous. However, Ref.[90] shows that the shape of dispersion relations can strongly differ from this approximation for non-zero temperature as well as in the presence of beams.

3.4 Methodology

A beam of fast electrons is injected into a plasma perpendicularly to the magnetic field. A 1.5D Maxwellian plasma is considered, allowing spatial variation in x only, while EM fields and particle momenta have all three components. The dimensions are chosen in order to turn off all contributions from Langmuir waves and analyse the purely EM signal (see chapter 4). Time-distance plots as well as time evolution of emission wavelet transforms and distribution function are investigated. Typical values for the important ratio $\frac{\omega_{ce}}{\omega_{pe}}$ are $0.1-10^{-3}$. We choose our parameters as to satisfy this requirement. The background magnetic field is constant $B = B_x = 0.0003$ T= 3 G, setting the electron gyrofrequency to $\omega_{ce} = 5.28 \times 10^7$ Hz rad everywhere. We ignore the radial decrease of the magnetic field in first approximation, while keeping a density gradient, which we believe to be crucial for the mode coupling mechanism here. Moreover, the constraint of $\nabla \cdot \mathbf{B} = 0$ in 1.5D does not allow for $B = B(x)$ given that $y-$ and $z-$ components are ignorable. The background temperature is $T = 3 \times 10^5$ K and isotropic. The background plasma density at $x = 0$ is $n_0 = 10^{14}$ m^{-3}, giving $\omega_{pe} = 5.64 \times 10^8$ Hz rad. This sets $\frac{\omega_{ce}}{\omega_{pe}} = 0.0935 \ll 1$. Further, the electron Debye length is $\lambda_{De} = 3.78 \times 10^{-3}$ m, while the grid size is $\lambda_{De}/2$. The simulation setup is such that we study a single magnetic field line connecting Sun and Earth. It is predicted that in the limit $r \gg R_{critical}$ the plasma density $n_e(r) \propto r^{-2}$ [48, 59], therefore, we use the following density profile

$$n_{e,i}(x) = n_0 \left[\left(\frac{x - x_{max}/2}{x_{max}/2 + n_+} \right)^2 + n_- \right] \tag{3.1}$$

with x_{max} being the total system length, mimicking the distance of the Sun to the Earth, and

$$n_+ = \frac{x_{max}}{2}\frac{1-\sqrt{1-n_-}}{\sqrt{1-n_-}}, \quad n_- = 10^{-8}. \tag{3.2}$$

In order to use periodic boundary conditions, the region $x_{max}/2 \leq x \leq x_{max}$ is set to an appropriate density increase. Data analysis will, therefore, focus on the region $0 \leq x \leq x_{max}/2$ only. The simulation is carried out using EPOCH.

A beam of fast electrons is injected perpendicularly to the magnetic field at simulation time $t = 0$. This is because Ref.[61] (see chapter 4) established that the parallel momentum (and the associated Langmuir waves) plays no role in the generation of EM emission. The beam carries a momentum of $p_b = p_y = m_e\gamma\frac{c}{2}$ with $\gamma \approx 1.155$. The beam temperature is $T_b = 6 \times 10^6$ K. The peak beam density is $n_{b0} = 10^{11}\mathrm{m}^{-3}$, while its spatial profile is defined as $n_b(x) = n_{b0}\exp(-[(x - x_{max}/25)/(x_{max}/40)]^8)$ with the beam density maximum at $x_{max}/25$. Fig.3.2 shows the density profiles

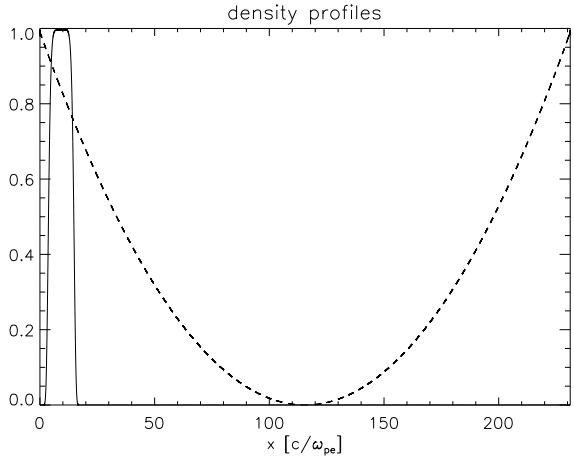

Figure 3.2: beam (solid) and background (dashed) density profiles at $t = 0$. Densities are normalized to their maxima.

for $t = 0$. Note that the beam is injected only at $t = 0$. In total we simulate up to $t = 150\omega_{pe}^{-1}$. As a result of the above defined quantities, at $x = 0$, the plasma beta is $\beta = 0.0115$. The mass ratio is $m_i/m_e = 1836$. The distribution functions are initially Maxwellian. With $p_\parallel = p_x$, $p_\perp = \sqrt{p_y^2 + p_z^2}$, this leads to $f_{b0}(\mathbf{p}) = \tilde{n}_b \exp(-[p_\parallel^2 + (p_\perp - p_{b\perp})^2]/(2m_e k_B T_b))$ for the beam, where k_B is Boltzmann's constant and $\tilde{n}_b$ is a normalization constant.

The initial parameters chosen are not a true representation of the solar corona, as such a setup would be beyond the scope of computational resources available to the

author. However, Ref.[83] has shown that for temperature $T = 3 \times 10^5$, the choice of plasma density $n_0 = 10^{14}$ m^{-3} sets the Debye length to $\lambda_{De} = 3.78 \times 10^{-3}$ m $= 7.11 \times 10^{-3} c/\omega_{pe}$. Adjusting the density to $n_0 = 10^{-5}$ m^{-3} yields $\lambda_{De} = 1.2 \times 10^7$ m $= 7.11 \times 10^{-3} c/\omega_{pe}$. Therefore, it is possible to scale the physical domain to an arbitrary size by use of (unrealistic) densities. In this sense, the used parameters represent a compromise between a realistic representation of the solar corona and a setup that makes treatment with PIC code feasible.
Further, it should be stressed that the used initial value for beam momentum perpendicular to the magnetic field is unrealisticly large. Typical beam speeds range from $0.3 - 0.6c$ and are expected to be almost in parallel direction, however, Ref.[65] has shown that beams travel at a nonzero pitch angle. The aim of the present study is to investigate the role of the perpendicular beam momentum component. This chapter shows that EM emission can be generated from a perpendicular beam momentum, while chapter 4 presents a parametric study of various pitch angles and background density profiles. The beam momentum in this chapter was chosen in order to be consistent with the parametric study in chapter 4.

3.5 Results

For a $\theta = 90°$ beam injection angle with respect to the magnetic field, in a spatial 1D simulation, the beam is trapped at its injection point. Fig.3.3 shows time-distance plots for EM field components, E_x and E_y, and changes in plasma density (left column), as well as spatial wavelet transforms of snapshots of E_y at times $t = 1.8, 80, 150\omega_{pe}^{-1}$ (right column), referring to the first pulsation maximum (top), the point where the wave packet passes the local plasma frequency (middle), and free propagation (bottom). Electric field strengths are given in units of $\omega_{pe} c m_e/e$, while distance and time are measured in c/ω_{pe} and ω_{pe}^{-1}, accordingly, where ω_{pe} is the plasma frequency at $x = 0$. The wavelet software was provided by C. Torrence and G. Compo [79], and is available at URL: http://paos.colorado.edu/research/wavelets/. The wavelet transforms can be interpreted in the same way as described in section IV of Ref.[61] (see chapter 4).
Conventional plasma emission processes rely on the generation of Langmuir waves in order to invoke EM emission. Such a signal would be found in the parallel component of the electric field E_x, as shown in Ref.[83]. It is evident from Fig.3.3, that there is no electrostatic Langmuir signal produced, yet clear wave structures can be found in the transverse components of the EM field, see E_y panel. The wave

front of those transverse signals suggest propagation of a signal with the speed of light (units are chosen such that a slope of ≈ 1 corresponds to a propagation at the speed of light), therefore, the transverse emission is electromagnetic. The lack of the Langmuir signal excludes the possibility that the generation of the EM emission stems from 'conventional' plasma emission mechanisms as mentioned in the introduction. This is due to the fact that in 1.5D plasma emission is not possible [83]. Contribution from the antenna mechanism is also excluded by the fact that there is no density cavity created at any time in the simulation, as shown in the bottom left panel of Fig.3.3. Fig.3.4 is a representative snapshot of the investigated

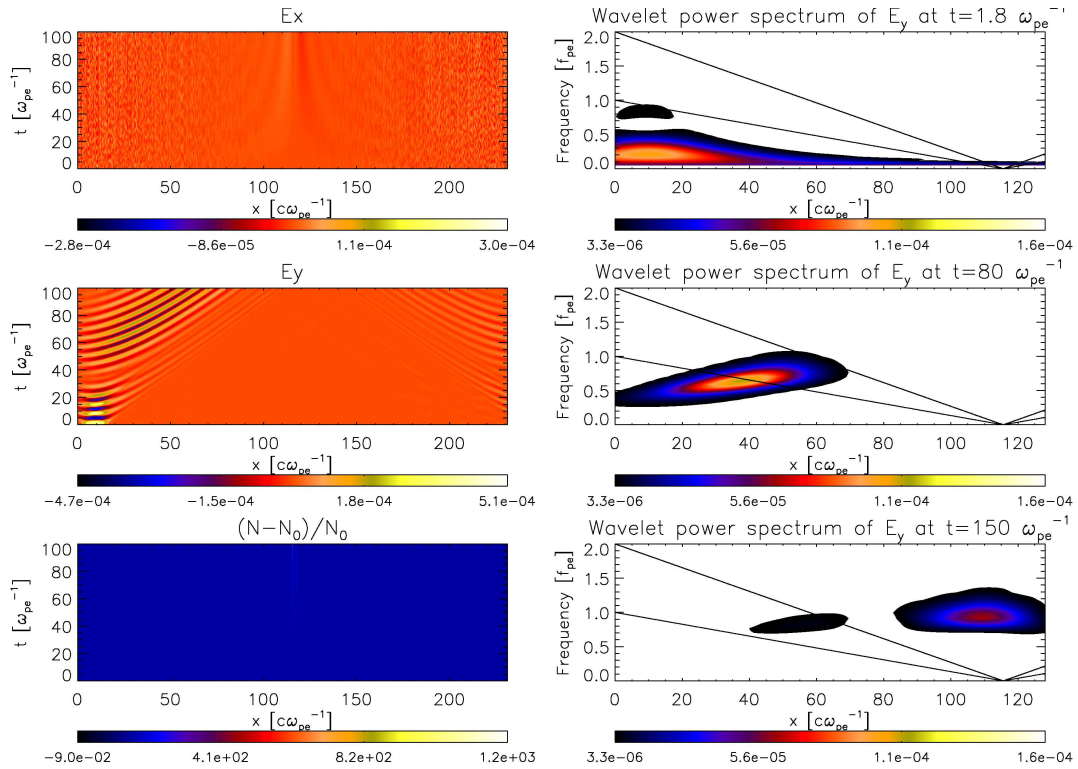

Figure 3.3: Left column: time-distance-plots of electric field components E_x (top panel) and E_y (middle panel), as well as change in density (bottom panel). Right: wavelet transform of E_y for $t = 1.8\omega_{pe}^{-1}$ (top panel), $t = 80\omega_{pe}^{-1}$ (middle panel), $t = 150\omega_{pe}^{-1}$ (bottom panel). Note that the background for the wavelet transform was set to white colour and does not refer to maximum amount of emission on the sides of the plots. Further, the black lines track the local plasma frequency and its second harmonic.

quantities of the electron distribution function at $t = 5\omega_{pe}^{-1}$. The time evolution of the wavelet transform of the transverse electric component E_y is shown in movie 1 [60] (including lines to indicate the local plasma frequency, its second harmonic and

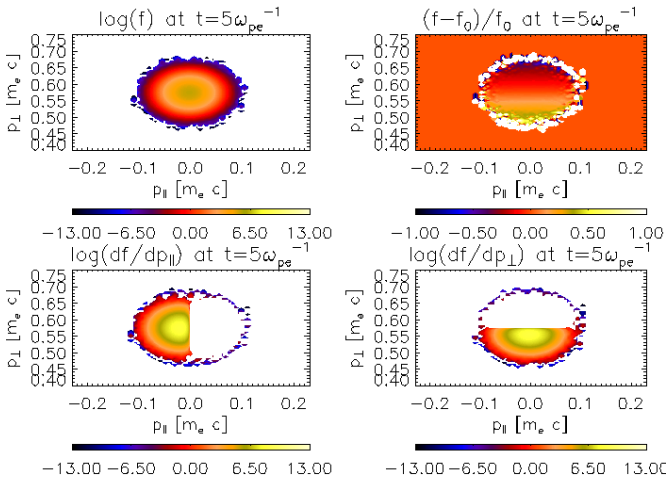

Figure 3.4: top left: $f(p_\parallel, p_\perp; t)$. top right: $\frac{f(t)-f(0)}{f(0)}$. bottom left: $\frac{\partial f(t)}{\partial p_\parallel}$. bottom right: $\frac{\partial f(t)}{\partial p_\perp}$ at $t = 5\omega_{pe}^{-1}$. Gradients are shown in logarithmic scales, which cannot show negative values, therefore, they appear white as the background.

the z-mode cutoff at $\omega_z = -\frac{1}{2}\omega_{ce} + \frac{1}{2}\sqrt{\omega_{ce}^2 + 4\omega_{pe}^2})$, while the respective evolution of the distribution function is given in movie 2 [60]. We can see from the distribution function, that the requirement for cyclotron maser emission, $\frac{\partial f}{\partial p_\perp} > 0$, is fulfilled at all times. This generates waves at the electron cyclotron frequency, which can be seen in the wavelet transforms. Those frequencies are too far below the plasma frequency and do not allow the wave to propagate. It, therefore, decays again. The quick generation and decay of waves at $0 \leq t \lesssim 30\omega_{pe}^{-1}$ appears as a pulsation. The frequency of this pulsation is found to be roughly twice the relativistic cyclotron frequency. It is likely that an energy exchange between beam and field, as shown in Ref.[97], is happening at this stage, as the distribution function shows subtle but complex dynamics in this time interval. Eventually, at $\approx 40\omega_{pe}^{-1}$, a stable wave packet is formed that rises in frequency, while it slowly moves away from the injection region. This is indicative of a mode coupling process on the density gradient. At some instant, (ω, k) of the emitted cyclotron emission coincides with that of the z-mode, an effect similar to the one discussed in e.g. Figs.1 and 2 of Ref.[16]. When the stable wave packet is formed, the distribution function shifts towards momenta higher than its initial maximum at $\approx 0.5775 m_e c$ and remains rather stable. At $t \approx 70\omega_{pe}^{-1}$ the wave packet reaches the lower cut-off frequency of the z-mode, at this point the distribution function shifts to lower momenta again. The wave packet keeps increasing its frequency until it reaches roughly the plasma frequency at the beam injection point.

We calculate the EM field energy, $w(t) = \int [\epsilon_0 \mathbf{E}(x,t)^2/2 + \mathbf{B}(x,t)^2/2\mu_0]dx$. We take care to exclude contributions from the background magnetic field B_0. We relate the field energy to the initial kinetic energy of the beam, $E_{kin}^{beam}(0) = 7.89 \times 10^{-3}$J. The overall efficiency is $\approx 10^{-3} E_{kin}^{beam}(0)$, as shown in Fig.3.5.
We also find the wave to be of left-handed polarization [61] (see chapter 4). In the case of $(\omega_{ce}/\omega_{pe} \ll 1)$, the cyclotron maser is known to generate z-mode waves, at frequencies that are harmonics of the cyclotron frequency [92]. The z-mode is left-hand polarized for $\omega < \omega_{pe}$ [90]. In movie 1 [60], it is shown that the wave packet is stabilized just below the local plasma frequency, therefore, it is no surprise to find the emitted wave to be of left-hand polarization.

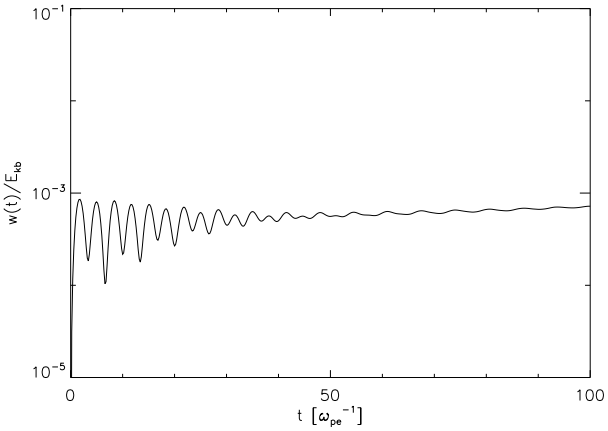

Figure 3.5: Total EM field energy, $w(t)$, normalized to the initial beam kinetic energy, $E_{kin}^{beam}(0)$.

3.6 Conclusions

In Ref.[83], it was shown that a non-gyrotropic beam injection into plasma can generate EM emission. Ref.[61] (see chapter 4) has shown that only the perpendicular momentum component of the injected electron beam causes the generation of EM emission. The main focus of Ref.[61] was a parametric study, i.e. how different beam injection pitch angles and different gradients affect the EM emission generation. Here the main goal is to focus on the physics of the EM emission *generation mechanism*. Thus, we carried out a 1.5D PIC simulation of a beam of relativistic, hot electrons injected with only a momentum component perpendicular to the background magnetic field into a Maxwellian plasma with a density gradient. The choice

of 1.5D turns off all EM emission generated by the classic plasma emission mechanism for all pitch angles, as it needs at least 2 spatial dimensions to work. The lack of parallel beam momentum meant that there was no electrostatic Langmuir wave generation, yet there was still EM emission due to the cyclotron maser. Therefore, there is no need for generation of Langmuir waves in order to generate EM emission via non-gyrotropic beam injection. The cyclotron maser generates emission at the electron cyclotron frequency, which - in the beam injection region of our simulation - is far below the plasma frequency, hence cannot propagate and decays. Generation and decay result in a pulsating emission generation until a stable wave packet is formed, that mode couples on the density gradient to what is likely to be a z-mode, until it reaches cut-off frequencies that allow for propagation. It may well be, that the quasi-linear relaxation, which would result in a plateau forming of the distribution function and eventual shutting down of the emission mechanism, happens on the same time scales as the inverse growth rate. Calculations of growth rates are not part of this study. We do not see a continuous generation of emission, because the injected beam has no temporal extent (as it would have in a real solar type III burst situation) and beam electrons are not replenished, i.e. injection happens only at $t = 0$. Further, a propagating beam would trigger the presented mechanism along its trajectory and, hence, produce the characteristic type III burst shape in the dynamical spectrum. Naturally, real life is not 1.5D, and generally there will be contributions from classic plasma emission mechanisms and the antenna radiation (if density cavities are formed) as well as the cyclotron maser. However, in cases of strong magnetic fields and straight field lines, situations can be well approximated by a 1D spatial model. In any case, there is likely a perpendicular beam momentum component, that will contribute to the overall emission. The interplay between EM emission generation mechanisms needs to be studied for various parameter spaces, but is not part of this work. Since the proposed mechanism has many applications (e.g. magnetrons, radar), we believe it could be interesting for the physics community at large.

4 The Effect of Electron Beam Pitch Angle and Density Gradient on Solar Type III Radio Bursts - A Parametric Study

The main findings of this chapter have been published in Ref.[61].

4.1 Introduction

Solar type III radio bursts are believed to be a result of relativistic electrons of $\approx 10 - 100$ keV, that propagate through solar plasma. The electrons might be accelerated in impulsive solar flares as they are observed to occur in groups of 10 and more [49]. Potential sources for acceleration include magnetic reconnection and dispersive Alfven waves [84, 85], which are both likely to be found in flare regions. Observationally, the electromagnetic emission spectrum of type III bursts show a characteristic drop of frequency over time in the 'dynamical spectrum' (frequency versus time intensity plot). The frequency of the observed electromagnetic signal typically drops a few orders of magnitude within minutes. The emission occurs at two separate frequencies, the fundamental plasma frequency and its second harmonic. It is observed that type III bursts are accompanied by electrostatic Langmuir waves as well as evidence for electron distribution functions that show a bump in the forward direction (parallel to the background magnetic field) in phase space [41]. Further, there is evidence for back propagating Langmuir waves as well as ion acoustic waves.

The common theory suggests that fast electrons, that propagate outward on an

open magnetic field line through the Sun's atmosphere, trigger the 'bump-on-tail' instability, which is responsible for the generation of the observed Langmuir waves. The Langmuir waves then, in turn, generate electromagnetic emission at the local plasma frequency and its second harmonic. As the beam of fast electrons propagates from denser into less dense regions, the frequency of the generated emission drops, because the plasma frequency is a function of the square root of the density. There are various theories on how the electromagnetic emission is generated. Those theories include non-linear wave-wave interactions (interactions of Langmuir waves with backward propagating Langmuir waves or ion-acoustic waves)[13, 27], linear mode conversion on density gradients (partial reflection and partial conversion of a Langmuir z-mode wave)[36], and the antenna mechanism (trapping of Langmuir waves in density cavities to drive currents at the second harmonic)[45, 46].
Recent works [67, 83] studied type III burst scenarios in particle-in-cell (PIC) type simulations. Ref.[67] investigated a magnetic field setup near a magnetic reconnection region in a 2.5D (2D in space, 3D in velocities, fields), Ref.[83] considered a generic magnetic field line connecting Sun to Earth in a 1.5D. Simulations in Ref.[83] were carried out with EPOCH, a fully relativistic, electromagnetic PIC code. In the present study of solar type III radio bursts, EPOCH was also used to simulate different beam injection angles into magnetised plasmas, as well as the effect of different background density gradients on the generated emission. The simulations were set up to inject a mildly relativistic, hot, low density beam into a spatially 1D plasma, that featured a constant background magnetic field as well as a parabolic density profile, both parallel to the spatial axis. The default setup and analysis tools were tested by successfully reproducing the results published in Ref.[83]. Ref.[83] established that generation of electromagnetic emission via a non-gyrotropic beam injection is possible. The primary goal of this study is the effect of different beam pitch angles and density gradients on the electromagnetic wave generation, as well as proving that EM emission can be generated without invoking Langmuir waves or the classical plasma emission mechanism, which involves Langmuir and ion-sound waves satisfying resonant beat conditions to mode convert into escaping transverse EM radiation.
In order to investigate the effect of different beam injection angles, components of the beam injection momenta were varied, while the total beam momentum (and hence the total kinetic energy of the beam) was kept constant in all cases. Results showed that a parallel beam momentum resulted in generation of an electrostatic Langmuir wave, visible in the parallel electric field component, travelling at the speed of the beam (essentially Langmuir turbulence following the beam). There

was no excitation of Langmuir waves found, when the beam is injected perpendicularly to the background magnetic field. In the perpendicular components of electric and magnetic fields, waves, that travel approximately with the speed of light, were found. This electromagnetic signal was also found for a perpendicular beam injection. Hence, the simulated generation of electromagnetic emission seems independent of the generation of electrostatic Langmuir waves.
It should be noted, that, in 1.5D geometry, the classic plasma emission mechanism is switched off, because it involves interaction of Langmuir, ion-acoustic and electromagnetic waves, that, when treated mathematically, involves a factor of $|\mathbf{k_L} \times \mathbf{k_T}|^2$, with $\mathbf{k_L}$ being wave vector of the Langmuir wave and $\mathbf{k_T}$ for the transverse electromagnetic wave. The angle between the two wave vectors for the 1.5D case is equal to zero, setting also the interaction probability to zero.
In the case of perpendicular beam injection, the electron distribution function will not show a bump in the forward direction, therefore, the instability, that is supposed to be responsible for the Langmuir wave generation, is never created. This result suggested an alternative emission mechanism.
Closer analysis of the distribution function in (parallel and perpendicular) momentum space showed, that, for non-parallel beam injection, a positive gradient was to be found in the perpendicular direction. Such shapes of distribution functions are referred to as cyclotron maser or loss-cone distributions. In special cases, if distribution functions are shaped appropriately, they are also called shell or horseshoe distributions, as studied in Ref.[19, 63] in the context of auroral kilometric radiation (AKR). It is known that these distributions allow for wave generation in most prominently x- and o-mode, but also z-mode [92]. Which mode is growing strongest is prescribed by the ratio ω_{ce}/ω_{pe}, i.e. how the magnetic field compares to plasma density, where ω_{ce} is the electron gyrofrequency and ω_{pe} is the plasma frequency.
This chapter is structured as follows: In Sec.4.2 we will discuss in detail the simulation setup. We will vary the beam injection angle in Sec.4.3 and demonstrate the impact of different background density gradients in Sec.4.4. In Sec.4.5, we will study the behaviour of the distribution function, while, in Sec.4.6, we will analyse the polarization of emitted waves as well as relate the generated field energy to the initial beam kinetic energy. Finally, we will summarize key points in 4.7.

4.2 Simulation Setup

All simulations, presented in this chapter, use EPOCH.
We are considering a 1.5D Maxwellian plasma, allowing spatial variation in x only, while electromagnetic fields and particle momenta have all three components. The background magnetic field along this line is kept constant $B = B_x = 0.0003$ T= 3 G, setting the electron gyrofrequency to $\omega_{ce} = 5.28 \times 10^7$ Hz rad everywhere. The background temperature is $T = 3 \times 10^5$ K and isotropic. The background plasma density at $x = 0$ is $n_0 = 10^{14}$ m^{-3}, giving $\omega_{pe} = 5.64 \times 10^8$ Hz rad. This sets $\frac{\omega_{ce}}{\omega_{pe}} = 0.0935 \ll 1$. Further, the electron Debye length is $\lambda_{De} = 3.78 \times 10^{-3}$ m.
The simulation setup is such that we simulate a single magnetic field line connecting Sun and Earth, while the grid size is $\lambda_{De}/2$. It is predicted that in the limit $r \gg R_\odot$ the plasma density $n_e(r) \propto r^{-2}$ ([48, 66]), therefore, we make use of

$$n_{e,i}(x) = n_0 \left[\left(\frac{x - x_{max}/2}{x_{max}/2 + n_+} \right)^2 + n_- \right] \tag{4.1}$$

with x_{max} being the total system length and

$$n_+ = \frac{x_{max}}{2} \frac{1 - \sqrt{1 - n_-}}{\sqrt{1 - n_-}}, \quad n_- = 10^{-8} \tag{4.2}$$

resembling a parabolic density drop off, such that $n_{e,i}(0) = n_{e,i}(x_{max}) = n_0$ and $n_{e,i}(x_{max}/2) = n_- n_0$. The unrealistic growing density in the region $x_{max}/2 \leq x \leq x_{max}$ is employed in order to use periodic boundary conditions. When analysing results we, therefore, draw conclusions from the region $0 \leq x \leq x_{max}/2$ only.
Further, in section 4.4, we consider modified plasma density profiles to study the effects of different density gradients. The following density profiles are used to study a *weak* and *strong* gradient

$$n_w(x) = n_0 \left[\left(\frac{x - x_{max}/2}{x_{max}/2 + n_+} \right)^2 + n_- \right], \quad n_- = 0.5 \tag{4.3}$$

$$n_s(x) = n_0 \left[\left(\frac{x - x_{max}/2}{x_{max}/2 + n_+} \right)^8 + n_- \right], \quad n_- = 10^{-8}. \tag{4.4}$$

A beam of accelerated electrons is injected at simulation time $t = 0$. It carries a momentum of $p_b = m_e \gamma \frac{c}{2}$ with $\gamma \approx 1.155$. The beam temperature is $T_b = 6 \times 10^6$ K. The peak beam density is $n_{b0} = 10^{11}$ m^{-3}, while its spatial profile is defined as

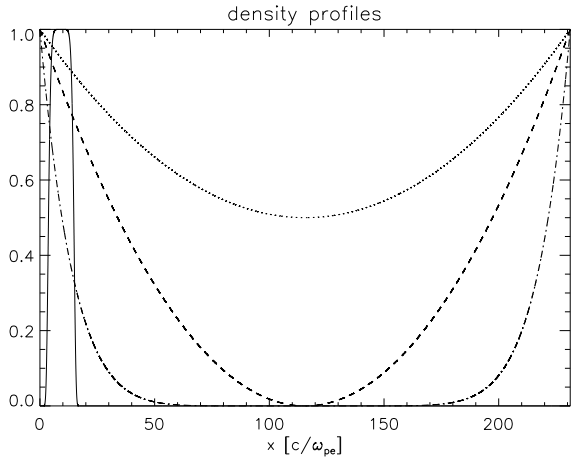

Figure 4.1: The electron beam (solid), weak (dotted), moderate (dashed), strong (dotted-dashed) density gradients at $t = 0$. Densities are normalized to their maxima.

$$n_b(x) = n_{b0} e^{-[(x - x_{max}/25)/(x_{max}/40)]^8} \tag{4.5}$$

setting the beam density maximum at $x_{max}/25$. In order to demonstrate the situation at $t = 0$ in terms of densities as a function of space, we plot the beam and background number density profiles in Fig.4.1. Note that the beam is injected only once, at $t = 0$, i.e. the beam electrons are not replenished.

As a result of the above defined quantities, at $x = 0$, the plasma beta is $\beta = 0.0115$. The mass ratio used is $m_i/m_e = 1836$.

Each simulation is run on 32 Dual Quad-core Xeon processors with 4 Tb of RAM. The simulation makes use of 65000 grid points and 10000 particles per cell in the case of the background electrons and ions. Despite the low beam electron density ($n_{e,i}(0)/n_b = 10^3$), the simulation achieves a reasonable number of beam electrons per cell, since the beam is focussed on only roughly 10 simulation cells, resulting in 100 beam electrons per cell. Herein lies, however, a shortcoming of the simulation setup as realistic background-to-beam electron ratios of $\approx 10^5 - 10^7$ cannot be achieved, because they would require considerably larger computational resources.

4.3 Varying Beam Injection Angle

In this section we analyse the effect of a variation of the beam injection angle (with respect to the background magnetic field) on the EM emission. We change the

injection pitch angles via variation of a perpendicular component in the beam momentum, $p_{by} = p_b \sin\theta$, while keeping the total momentum p_b constant in all cases. Therefore, an increase of the beam pitch angle θ is equivalent to an increase of perpendicular beam momentum p_{by}, respectively a decrease in parallel beam momentum $p_{bx} = p_b \cos\theta$, hence, a decrease in propagation speed. For the case $\theta = 90°$, the parallel component of the beam momentum vanishes and the beam is trapped at its point of injection. The background plasma density profile in this section is always represented by Eq.(4.1) which corresponds to the dashed line in Fig.4.1. We study cases of $\theta = 15°, 45°, 60°, 90°$. In order to analyse the simulation data, we make use of time-distance plots and spatial wavelet transforms of the electromagnetic field components. Time-distance plots offer the possibility of studying the development of a physical quantity with respect to space and time. We make use of this technique to plot components of electric and magnetic fields as well as the electron density. We observe waves in both electric and magnetic components. The slope that is being produced by the wave front in this plot can then shed light on the propagation speed of that wave. We choose units for spatial and temporal axis such that a slope of ≈ 1 corresponds to propagation with the speed of light. Hence, finding waves that travel with $\approx c$ suggests that the emission is electromagnetic.
Generally, dynamical spectra show a characteristic feature of solar type III bursts. These plots show the development of the emission frequency over time. As discussed previously, in the case of solar type III bursts, the dynamical spectrum shows a frequency drop over time. This drop is due to the decreasing background plasma density, that a beam of accelerated electrons encounters, while travelling away from the Sun. The drop in density correlates to a drop of the local plasma frequency, since $\omega_{pe} \propto \sqrt{n_e}$. As the beam triggers emission at the local plasma frequency (and its second harmonic), while it travels from denser into less dense plasma, it generates emission of dropping frequency that is characteristic for solar type III bursts. We investigate the frequency of the generated emission by performing a wavelet analysis of a perpendicular component of the electric field; we choose E_y. We take a snapshot of E_y at a given time and perform a spatial wavelet analysis. The wavelet software was provided by C. Torrence and G. Compo [79].

Figs.4.2,4.3,4.4,4.5 show time-distance plots of components of the electric field in the left column. The right column contains plots of changes in number density, the magnetic y-component and the wavelet transform of E_y taken at $t = 100\omega_{pe}^{-1}$. Electric and magnetic field strengths are normalized to units of $\omega_{pe} c m_e/e$ and $\omega_{pe} m_e/e$, respectively, while distance and time are measured in c/ω_{pe} and ω_{pe}^{-1}, accordingly, where ω_{pe} is the plasma frequency at $x = 0$. This is a good value of reference, as the

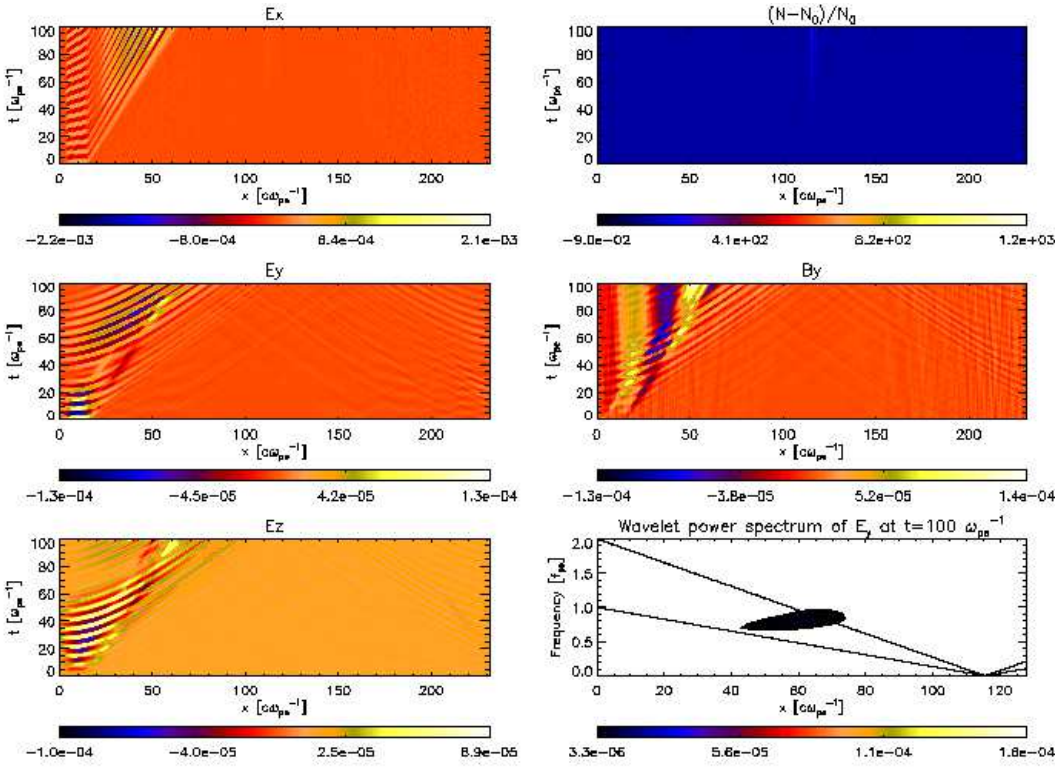

Figure 4.2: $\theta = 15°$. The moderate density profile, given by Eq.(4.1), was used. Left column: time-distance-plots of electric field components. Right: time-distance-plot of changes in density, magnetic field y-component, and the wavelet transform of E_y. Note that the background for the wavelet transform was set to white colour and does not refer to maximum amount of emission on the sides of the plot. Further, the black lines track the local plasma frequency and its second harmonic.

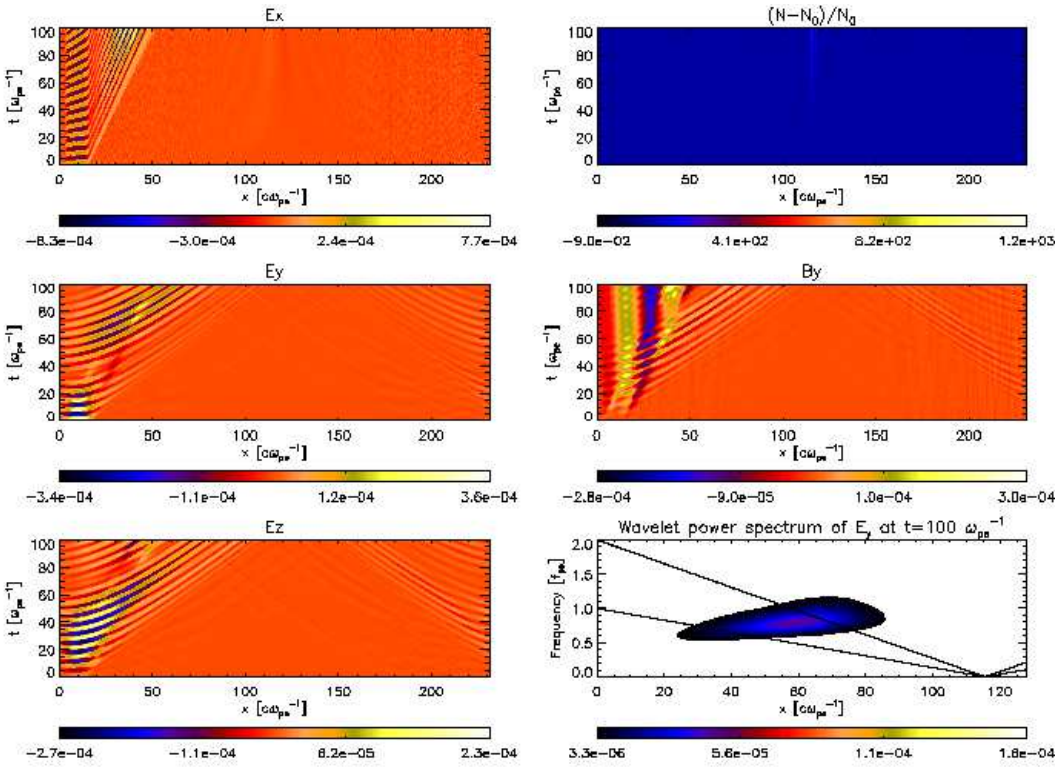

Figure 4.3: As in Fig.4.2, but $\theta = 45°$.

background density (and therefore the plasma frequency) at this point are equal in all simulations, regardless of which density profile for the background (see Fig.4.1) is used.

Comparing the time-distance-plots for electromagnetic fields, we find wave generation in the perpendicular components for all injection angles. The wave front shows a slope of ≈ 1, is therefore travelling with the speed of light and can be interpreted as electromagnetic emission. The wave propagation speed in the perpendicular components does not depend on the beam injection angle and is therefore independent of the beam propagation speed. Similar analysis of the parallel component E_x shows rather different behaviour. In the $\theta = 90°$ case (Fig.4.5), E_x does not show any wave features and no parallel component to the emission is generated. In the other cases (Fig.4.2,4.3,4.4), we can see generation of a standing wave as well as a travelling electrostatic wave, which shows different propagation speeds for each of the cases, and can be associated with the beam propagation speed. This signal also has components in the perpendicular plane, most notable in the magnetic B_y component, but also in (rather weakly) E_y and E_z, where it interferes with contributions of the electromagnetic emission. The width of the signal at $t = 0$ corresponds to the width

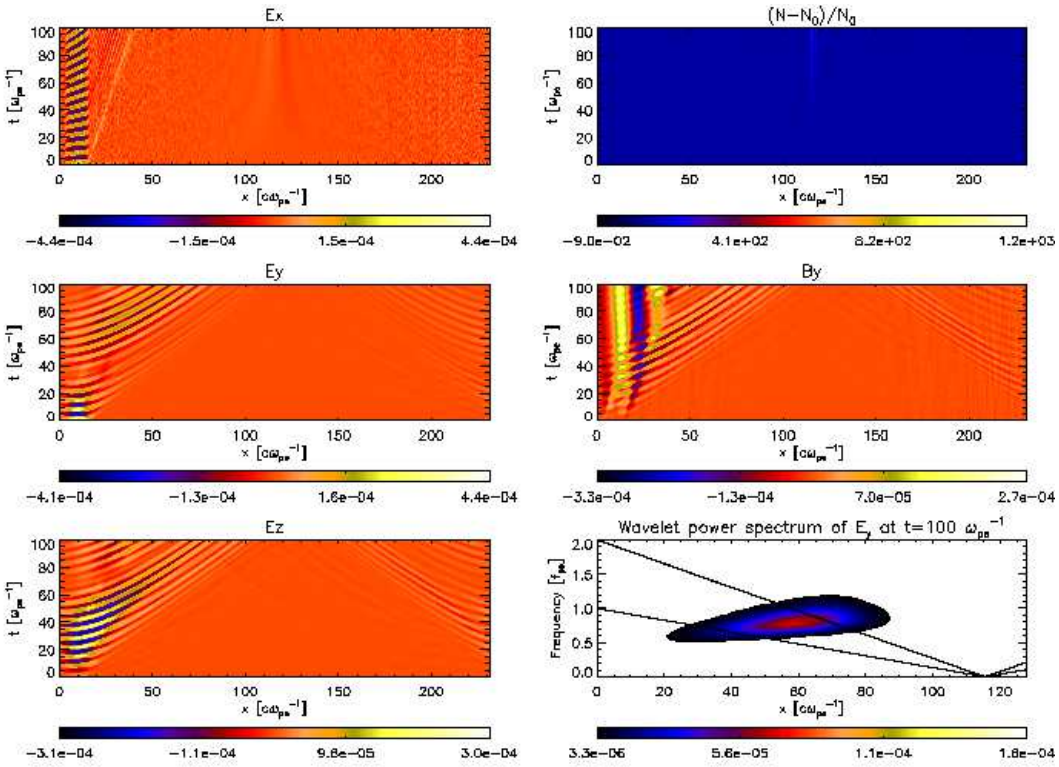

Figure 4.4: As in Fig.4.2, but $\theta = 60°$.

of the beam at the start of the simulation.

In all cases, the density profile remains unchanged (see top right panels on Figs.4.2-4.5). This is important as it excludes any possibility of developing density cavities in the plasma, which could trap Langmuir waves and contribute to the emission in form of the antenna mechanism [45]. Thus, in our simulations, EM emission is generated by a mechanism other than the antenna mechanism or plasma emission (the latter requires at least 2D in space).

Comparing wavelet transforms for various pitch angles, we clearly see that emission intensity is proportional to the perpendicular component of the beam momentum. Other than that, there is no evidence of change in the wavelet transform and emission characteristics as peak frequencies, emission times (respectively location) and wave packet shapes are all preserved. Analysis of the peak emission intensity as a function of pitch angle is shown in Fig.4.6.

The figure shows that the peak emission intensity (normalised to its maximum value at $\theta = 90°$) can be almost perfectly approximated by $\sin^2(\theta)$, and therefore p_{by}^2. This result suggests a direct correlation of the beam kinetic energy, $E_{kin}^b \propto p_b^2$ and the generated emission intensity.

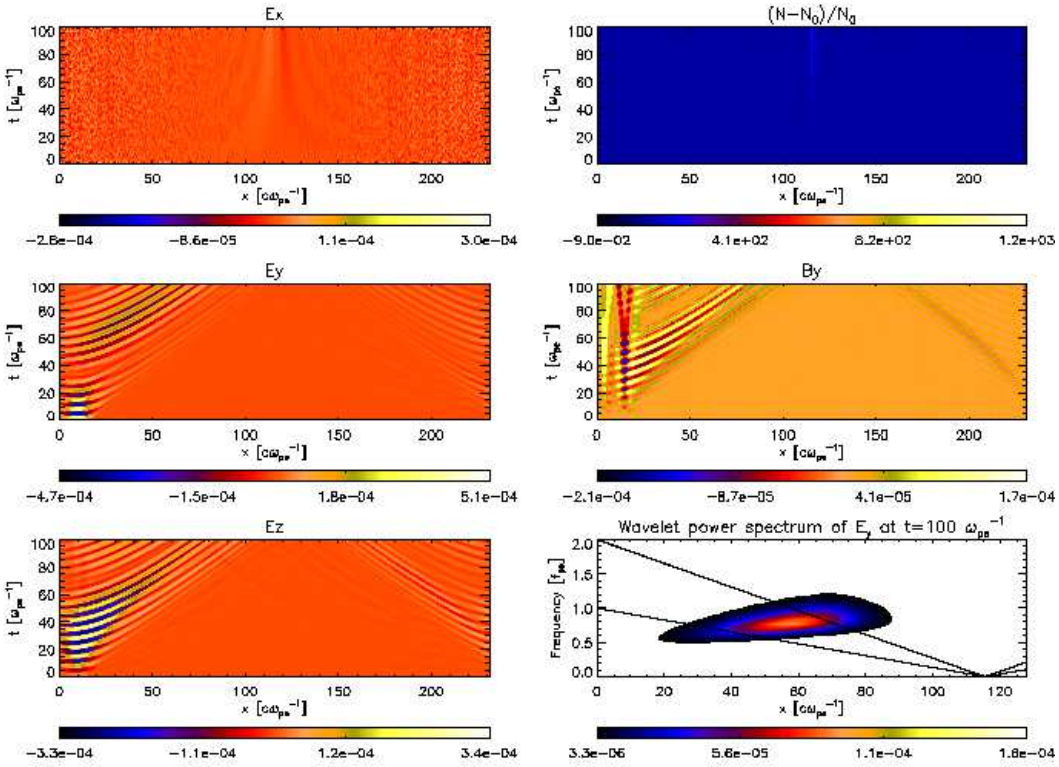

Figure 4.5: As in Fig.4.2, but $\theta = 90°$.

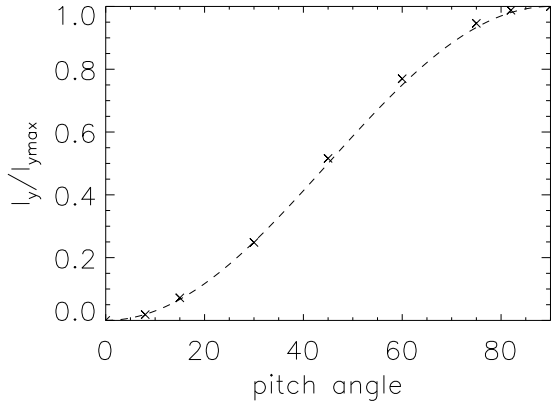

Figure 4.6: The maximum emission intensity $I_{max}(\theta)$ normalized to $I_{max}(90°)$ (crosses) and $\sin^2(\theta)$ (dashed) as a function of pitch angle θ in degrees.

4.4 Time Development and Varying the Background Density Profile

We now focus on the $\theta = 90°$ case, as it shows the maximum generated emission in E_y. In this section we investigate the role of the background density profile. We refer the reader to Fig.4.1 for the different density profiles. Additionally, we investigate a case without any density drop, where $n_c(x) = n_0$.

The time development of the wavelet transform allows insight into the emission generation process, wave propagation, as well as frequency drift. We generated movies to demonstrate this (movie 1, movie 2, movie 3, and movie 4 in Ref.[61]). Again we focus on the wavelet transform of E_y. We include curves that mark the local plasma frequency and its second harmonic, as well as $\omega_z = -\frac{1}{2}\omega_{ce} + \frac{1}{2}\sqrt{\omega_{ce}^2 + 4\omega_{pe}^2}$, which is the cut-off for the z-mode. From the movies, it is evident that as soon as the beam is injected, we observe a pulsating signal of generated emission. The frequency of this emission is much smaller than ω_{pe} and, therefore, does not allow instant propagation (note that $\omega_{ce}/\omega_{pe} \ll 1$). Instead, pulsation eventually dies down only before an apparently stable wave packet is formed. The stable packet then drifts to higher frequencies. This suggests mode coupling of the cyclotron emission on the gradient to (possibly) a z-mode. When the peak frequency of the wave packet is comparable to the local plasma frequency (which for our parameters is not significantly different from ω_z), the packet starts propagating. Interestingly, the increase in frequency does not stop at this point but only when the wave packet travels into a region where the second harmonic of the local frequency, $2f_{local}$, matches the fundamental of the plasma frequency at the injection point f_{inj}. (Note that the beam is not injected at $x = 0$, but has a finite width and f_{inj} is the plasma frequency at the beam density function's maximum at $x_{max}/25$.) From this point on the wave packet moves on with constant frequency.

It should be stressed, that the density increase in the right half (i.e. $x_{max}/2 \leq x \leq x_{max}$) of the simulation box was only employed in order to use periodic boundaries and has no physical meaning here. This study was limitted to negative density gradients as this is the case for solar type III radio bursts. It does not take into account effects that occur in the positive gradient region. The aim is to show that electromagnetic emission is generated from non-gyrotropic beam injection and can escape the beam injection region via the outlined mechanism.

In Fig.4.7, we show snapshots of wavelet transforms at different simulation times. We choose to look at an early snapshot of the pulsation phase, a second snapshot

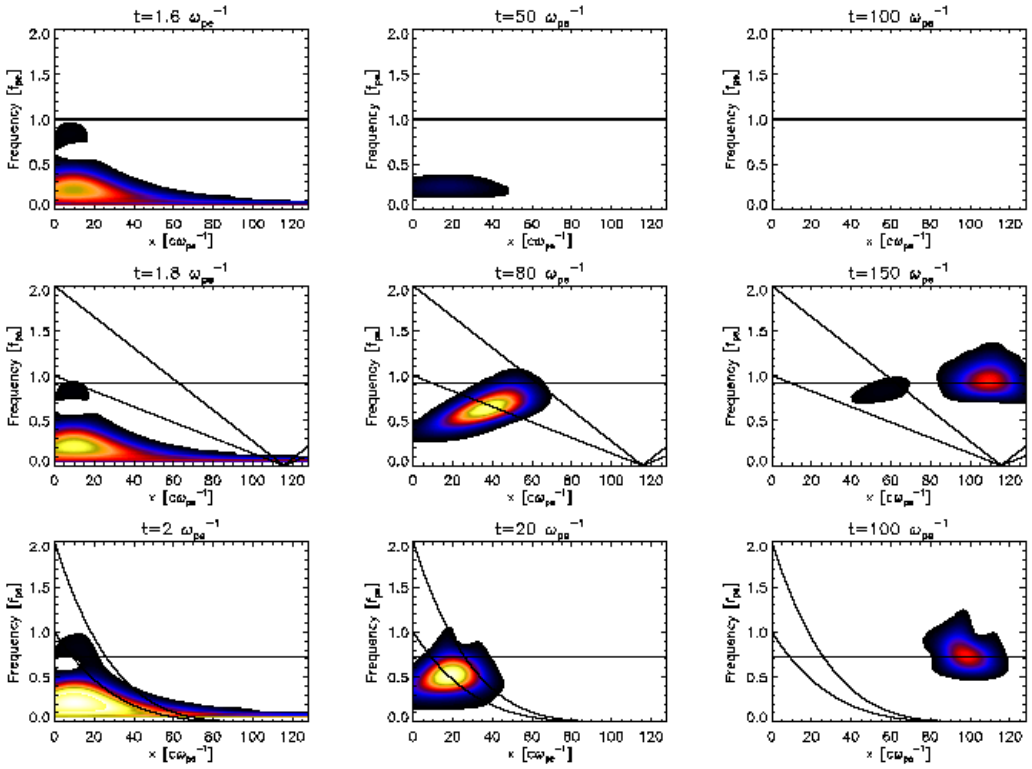

Figure 4.7: Wavelet transforms for different density gradients at different times. Top row: density is constant. Middle row: moderate gradient according to dashed line in Fig.4.1. Bottom row: strong gradient according to dotted-dashed line in Fig.4.1. Black curves correspond to local plasma frequencies and the second harmonic, the horizontal line is the plasma frequency corresponding to the point of the beam density maximum at the time of the beam injection, f_{inj}.

when the wave packet couples to frequencies $\approx f_{pe}$ and, ultimately, the final snapshot in the simulation. Note that for the mid row case, the total simulation time has been extended to $t = 150\omega_{pe}^{-1}$. In order to not get any interference due to periodic boundary conditions, the total system size was increased by a factor of 1.5 in this run.

We see that for constant density, there is no emission, as the wave packet never mode couples to frequencies that would allow propagation. At this point, we sum up the key findings: The beam injection evokes pulsating emission far below the local plasma frequency f_{pe}. Eventually, this cyclotron emission mode couples to the z-mode, which has a frequency comparable to the local plasma frequency, and that allows for escape of the emission. The wave packet frequency increases up to the point where it reaches the plasma frequency of the original beam injection point,

f_{inj}. This happens at the point where the second harmonic of the local plasma frequency, $2f_{local}$, is of the order of f_{inj}.
These observations enable us to draw the following conclusions with regards to the role of the density profile in our simulations: In case of the constant density profile, there is no escaping emission, as the generated emission cannot couple to a propagating wave mode. A steeper gradient in the density profile will result in earlier emission, because the mode coupling process couples to a frequency that is able to escape sooner than it does for weaker gradients.
We would like to note that Fig.4.7 as well as all movies of wavelet transforms in Ref.[61] suggest that the pulsation maximum is not at the y-axis value corresponding to f_{ce}. This is due to the fact that in order to be able to interpret the y-axis as frequency, one needs to be able to relate space and time via $x = ct$. The latter is only applicable to escaping electromagnetic radiation. In the left bottom corner of the wavelet transforms, i.e. the beam injection region, this relation does not hold, as we are dealing with a trapped mode far below f_{pe}. Therefore, whilst the wave packet resides in this region, the y-axis actually corresponds to the wave number k rather than the wave frequency. Numerical runs of wider (respectively narrower) beam width, not shown here, corroborate that the y-value of the spatial wavelet transform in regions well below f_{pe} scales as k. It is only after $f \approx f_{pe}$ and $x = ct$ applies, that the y-axis can be interpretted as wave frequency. Further, the fact that the initial pulsation is excited at the relativistic cyclotron frequency can be evidenced from figures equivalent to Figs.4.2,4.3,4.4,4.5 but for longer runs, which are not shown here. E_y panels of the figures shown here already suggest that there is a time interval of $\approx 60\omega_{pe}^{-1}$ between the bottom left wave structure and the one following. Thus, the frequency of the oscillation is $1/\Delta t = 2\pi f_{pe}/60 \approx 0.1 f_{pe} \approx f_{ce}$.

4.5 Distribution Function Dynamics

4.5.1 Cartesian Coordinates

At any given timestep, in EPOCH, distribution functions for every species are functions of space and momentum, i.e. $f(x, \mathbf{p})$. They satisfy the equation

$$\int f_\sigma(x, \mathbf{p})\, \mathrm{d}^3p\, \mathrm{d}x = N_\sigma \tag{4.6}$$

with N_σ being the total number of particles of a species σ (electrons, ions, beam electrons). The distribution functions of both the background plasma and the beam

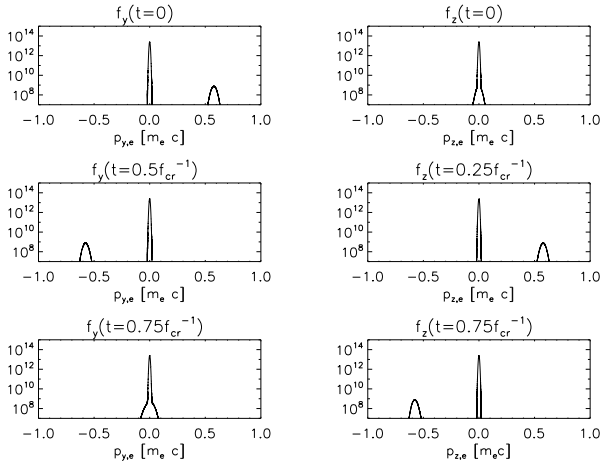

Figure 4.8: Distribution function for the background and beam electrons in momentum space at different times (from top to bottom) for $\theta = 90°$; $f(p_y)$ (left column) and $f(p_z)$ (right column).

electrons in momentum space are initially Maxwellian. This allows us to separate the spatial from the momentum part, by $f(x, \mathbf{p}) = \tilde{f}(x)\tilde{f}(\mathbf{p})$, at $t = 0$. The momentum part can, then, be described by

$$\tilde{f}_{e,i0}(\mathbf{p}) = \tilde{n}_{e,i} e^{-(p_x^2+p_y^2+p_z^2)/(2m_{e,i}k_B T)} \tag{4.7}$$

for the background and

$$\tilde{f}_{b0}(\mathbf{p}) = \tilde{n}_b e^{-[(p_x-p_{bx})^2+(p_y-p_{by})^2+p_z^2]/(2m_e k_B T_b)} \tag{4.8}$$

for the beam respectively, where k_B is Boltzmann's constant and $\tilde{n}_{e,i,b}$ are normalization constants corresponding to a species (electrons, ions, beam electrons).

EPOCH allows for distribution functions to be computed with respect to spatial and momentum coordinate components, as well as all desired combinations. It is therefore possible to generate arrays for distribution functions in all momentum components, $f(p_x, p_y, p_z)$, but also specific components, for example $f(p_x)$,$f(p_x)$... Here, the spatial dependency has already been integrated out by EPOCH. Following the time development of the distribution function for various angles, we refer to movie 5 and movie 6 in Ref.[61]. In the movies we show the development of the distribution function in three panels, top to bottom: $f(p_x)$, $f(p_y)$, $f(p_z)$.

Fig.4.8 shows snapshots of $f(p_y)$ and $f(p_z)$ at different times. Each panel, generally, shows two bumps. The larger one refers to the background electrons, while

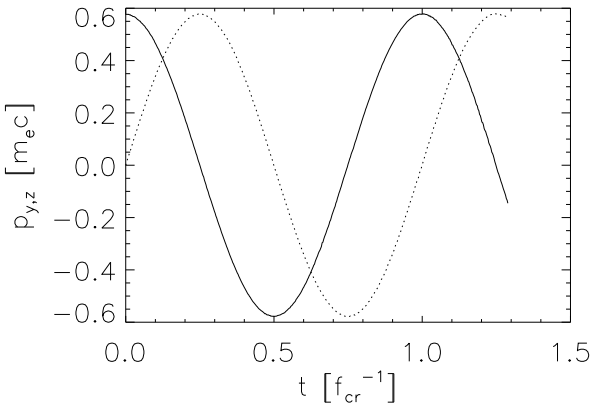

Figure 4.9: Position of beam maximum in momentum space as function of time for $\theta = 90°$; p_y (solid) and p_z (dotted) in units of $[m_e c]$.

the smaller one corresponds to the beam. We can clearly see that the background distribution function as well as the beam distribution in *parallel* momentum space (**B** along x) remain almost constant throughout our simulations. In *perpendicular* momentum space, however, we observe oscillation of the beam distribution, as well as a broadening and widening of the beam bump. We focus on the perpendicular panels and follow the position of the beam maximum in time, which is shown in Fig.4.9.

Fig.4.9 is representative for all cases studied. The maxima for this run are at $\frac{\gamma}{2} \approx 0.5775 m_e c$. (Note that for different injection angles, the maxima are shifted to different values on the ordinate, because different injection angles result in different values of p_y, but the functional characteristics will stay the same.) It shows that the maximum of the beam distribution function oscillates in the perpendicular components. The frequency of the oscillation is the relativistic cyclotron frequency, $\omega_{cr} = \omega_{ce}/\gamma$. It is trivial to deduce that the beam is gyrating around the magnetic field.

4.5.2 Parallel and Perpendicular Coordinates

While the cartesian form offers a valuable look into dynamics of the beam, investigation of instabilities often require a transformation of the distribution function to a momentum space with coordinates parallel and perpendicular to the background magnetic field, i.e. $f(p_\parallel, p_\perp)$. While in the more conventional plasma emission process, Langmuir waves are being generated via the 'bump-on-tail'-instability, referring

to a bump in the distribution function in *parallel* momentum space, $\frac{\partial f}{\partial p_\parallel} > 0$, the requirement for the triggering of cyclotron maser (or loss-cone) emission is a positive slope of the distribution function with respect to the *perpendicular* direction, $\frac{\partial f}{\partial p_\perp} > 0$. EPOCH does not allow for direct output of $f(p_\parallel, p_\perp)$, so a transformation algorithm was developed. The transformation relations are straight forward

$$\begin{aligned} p_\parallel &= p_x \\ p_\perp &= \sqrt{p_y^2 + p_z^2} \end{aligned} \tag{4.9}$$

The data volume accumulated by the simulation is prescribed by the resolution of the distribution function. A resolution of 300 points over an interval of $-0.91 m_e c < p_{x,y,z} < 0.91 m_e c$ was chosen, to retain reasonable resolution while keeping data volume comparatively small. The algorithm was tested by successfully reproducing Fig.1 in Ref.[92].

Movie 7 in Ref.[61] shows the time development of the distribution function for the $\theta = 90°$ case. The top left panel in Fig.4.10 shows a plot of the distribution function on a logarithmic scale at a given time step, while the top right panel plots the relative change with respect to the initial distribution, $\frac{f(t)-f(0)}{f(0)}$, in order to visualise dynamics. In the lower row, the gradients $\frac{\partial f}{\partial p_\parallel}$ (left) and $\frac{\partial f}{\partial p_\perp}$ (right) are shown. We can clearly see that the initial distribution fulfils the criterion $\frac{\partial f}{\partial p_\perp} > 0$. Further, the movie shows interesting dynamics in the shape of $f(p_\parallel, p_\perp)$. The left panel shows no drastic changes throughout the simulation time, while the relative change on the right panel suggest shifting to higher and lower perpendicular momenta. First, the distribution increases in momenta that lie below the initial maximum, $\approx 0.5775 m_e c$, then the movement is reversed. Until around $t \approx 30\omega_{pe}^{-1}$ we can see frequent change in the direction of shifting. Comparing this to movie 3 in Ref.[61], we see that the time scales correspond to the pulsating phase in the wavelet transform, suggesting an energy exchange between beam and EM fields, as found in Ref.[97]. Eventually the distribution shifts to momenta above the initial maximum and forms almost a straight line at $\approx 0.5775 m_e c$, separating regions of increased distribution from decreased ones, at $t \approx 40\omega_{pe}^{-1}$. Comparison with movie 3 in Ref.[61] shows that this is about the time, when we can see a stable (no longer pulsating) wave packet being formed. At $t \approx (70 - 90)\omega_{pe}^{-1}$, the distribution function shifts again to momenta below $\approx 0.5775 m_e c$. The wavelet transform shows that this is the time, when the wave packet passes over the local plasma frequency limit. Fig.4.10 is a representative snapshot at $t = 40\omega_{pe}^{-1}$. The gradients in the bottom row are

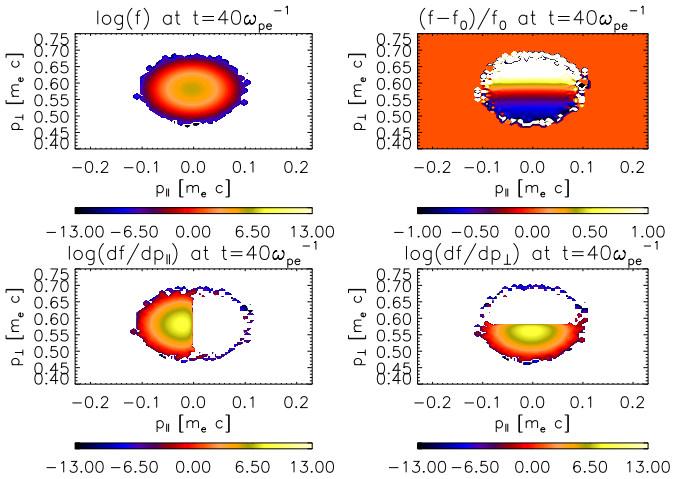

Figure 4.10: Top left: $f(p_\parallel, p_\perp, t)$. top right: $\frac{f(t)-f(0)}{f(0)}$. bottom left: $\frac{\partial f(t)}{\partial p_\parallel}$. bottom right: $\frac{\partial f(t)}{\partial p_\perp}$ at $t = 40\omega_{pe}^{-1}$. Gradients are shown on logarithmic scales, which cannot show negative values, therefore, they appear white as the background.

presented on a logarithmic scale, therefore, negative gradients cannot be shown and appear in the same white background colour.

4.6 Generated Electromagnetic Field Energy and Polarization

We calculate the electromagnetic field energy,

$$w(t) = \int [\frac{1}{2}\epsilon_0 \mathbf{E}(x,t)^2 + \frac{1}{2\mu_0}\mathbf{B}(x,t)^2]\,\mathrm{d}x \tag{4.10}$$

We take care to exclude contributions from the background magnetic field B_0. We relate the field energy to the initial kinetic energy of the beam, $E_{kin}^{beam}(0)$, which we calculate analytically using the expression for the mean relativistic kinetic energy

$$< E_{kin}^{beam}(0) >= \int n_b(x) m_e c^2 [\gamma(< \mathbf{p}_0 >) - 1]\,\mathrm{d}x \tag{4.11}$$

where $\gamma(< \mathbf{p}_0 >)$ is the Lorentz factor in terms of initial bulk momentum

$$\gamma(< \mathbf{p}_0 >) = \sqrt{1 + (\frac{< \mathbf{p}_0 >}{m_e c})^2} \tag{4.12}$$

with the initial bulk momentum $< \mathbf{p}_0 >$, given by

$$\begin{aligned} < \mathbf{p}_0 > &= \frac{\int \mathbf{p} f_0(x, \mathbf{p}) \, \mathrm{d}^3 p}{n(x)} \\ &= \frac{\tilde{f}_0(x) \int \mathbf{p} \tilde{f}_0(\mathbf{p}) \, \mathrm{d}^3 p}{n(x)} \end{aligned} \tag{4.13}$$

Using the relation

$$\int f(x, \mathbf{p}) \, \mathrm{d}^3 p = n(x) \tag{4.14}$$

along with the normalization condition

$$\int \tilde{f}(\mathbf{p}) \, \mathrm{d}^3 p = 1 \tag{4.15}$$

we see that the spatial part of the distribution function becomes the particle density distribution

$$\tilde{f}(x) = n(x) \tag{4.16}$$

Hence, the bulk momentum can be written as

$$< \mathbf{p}_0 > = \int \mathbf{p} \tilde{f}_0(\mathbf{p}) \, \mathrm{d}^3 p \tag{4.17}$$

where $\tilde{f}_0(\mathbf{p})$ is the initial beam distribution function and can be deduced from Eq.(4.8). For our simulation parameters, the initial kinetic energy of the beam is $E_{kin}^{beam}(0) = 7.89272 \times 10^{-3}$J. We use this result to see how much of the beam energy gets converted into magnetic energy, by plotting this in Fig.4.11.

The figure shows the time development of the ratio $w(t)/E_{kin}^{beam}(0)$ for different beam injection angles. We can see that the mechanism has a typical efficiency of $\approx 10^{-3}$-10^{-2}. Most notable is that, for our parameters, a smaller injection angle θ results in a higher efficiency. Note that this is not in contradiction with Fig.4.6. Here, we take all electromagnetic field components into account, whereas, in Fig.4.6,

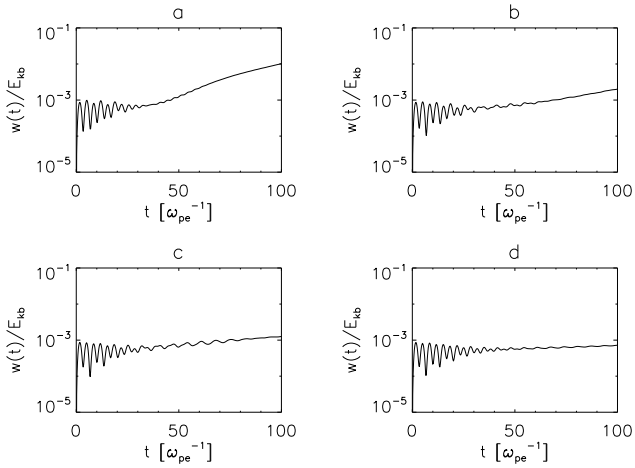

Figure 4.11: Total field energy generated, w, normalized to initial kinetic energy of the beam, $E_{kin}^{beam}(0)$ according to Eq.4.11, as a function of time for a) $\theta = 15°$ b) $\theta = 45°$ c) $\theta = 60°$ d) $\theta = 90°$.

we focused solely on the peak intensity of the electric y-component, namely the wavelet transform of E_y, and showed a direct relation to the y-component of the kinetic energy of the beam. Fig.4.6 is also in line with the previously presented time-distance plots Figs.4.2-4.5. Comparing the scales in the respective color bars shows that the parallel component of the electric field, hence the electrostatic wake of the beam, is dominant for the presented cases (except of course for the $\theta = 90°$-case, where the parallel component vanishes). Fig.4.11 shows the pulsating nature of the early stages of the emission generation. The pulsation can be associated with the electromagnetic part of the emission, because it is generated in all cases. In the $\theta = 90°$-case (Fig.4.11d), the initially generated electromagnetic emission stabilizes at $\approx 10^{-3} E_{kin}^{beam}(0)$. In the other cases, we see that eventually the electrostatic wake of the beam overpowers the electromagnetic part significantly and subsequently causes an increase in the total field energy up to $\approx 10^{-2} E_{kin}^{beam}(0)$ in the $\theta = 15°$-case (Fig.4.11a).

The degree of linear polarization L is defined similarly to Ref.[97]

$$L = \frac{w_\perp - w_\parallel}{w_\parallel + w_\perp} \tag{4.18}$$

and its time development is presented in Fig.4.12.

Fig.4.12 shows a strong dependence of L with respect to the injection angle. As shown in Fig.4.11, the parallel component of the field energy becomes dominant for

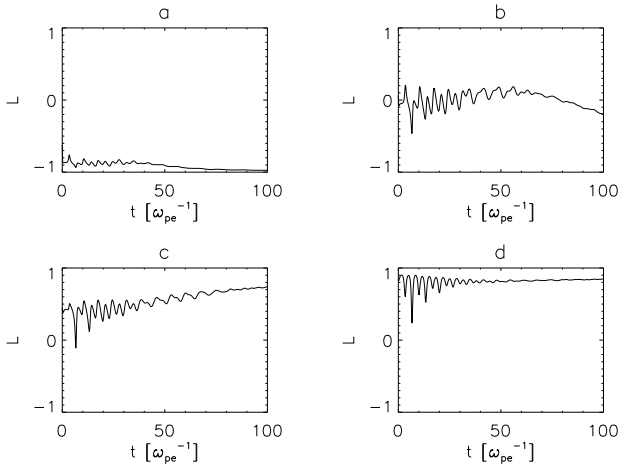

Figure 4.12: Degree of linear polarization L as a function of time for a) $\theta = 15°$ b) $\theta = 45°$ c) $\theta = 60°$ d) $\theta = 90°$.

small injection angles, but is negligible in the $\theta = 90°$-case. Not surprisingly, we see a very strong degree of linear polarization for this case.
Concentrating on $\theta = 90°$, we plot the time evolution of the electric field in the perpendicular (y,z-)plane in Fig.4.13. In the figure, the x-axis points out of the plane. The time development is then shown by a change of pixel color, therefore we see that the wave is left-hand polarized.

A cyclotron maser in our parameter space ($\omega_{ce}/\omega_{pe} \ll 1$) is expected to generate waves in the z-mode, at frequencies that are harmonics of the cyclotron frequency [92]. The polarization of the z-mode is left-handed for $\omega < \omega_{pe}$ and right-handed for $\omega > \omega_{pe}$ [90]. This is in line with our result, as the stable wave packet was generated below the plasma frequency, and is therefore expected to show left-hand polarization.

4.7 Conclusion

In this chapter, we study further the details of the non-gyrotropic beam driven emission mechanism, first outlined in Ref.[83]. We carried out 1.5D PIC simulations of a super-thermal electron beam being injected into a magnetised, Maxwellian plasma. We investigated the role of the injection angle (pitch angle) of the beam with respect to the constant background magnetic field.
The evolution of spatial wavelet transforms of E_y was demonstrated in movies. The movies show that, initially, pulsating emission well below the local plasma frequency

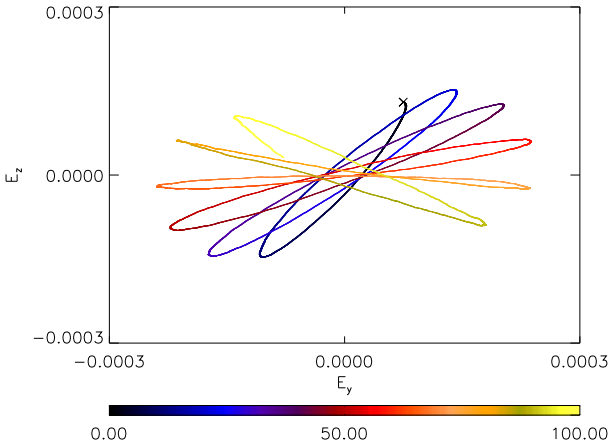

Figure 4.13: Polarization in the perpendicular (y,z-)plane as a function of time for $\theta = 90°$. The x-axis points out of the paper plane. The black 'x' marks the starting point, color corresponds to time in units of ω_{pe}^{-1}. Electric field components are given in units of $\omega_{pe} c m_e / e$.

is generated. Waves of such low frequencies cannot propagate in plasma, thus, in order for the waves to escape, a mode conversion has to take place. In the movies, mode conversion is identified by the formation of a stable wave packet, which drifts to higher frequencies, propagating only very slowly from the injection region. When the wave packet reaches frequencies of the order of the plasma frequency, propagation accelerates. The frequency drift, however, does not stop at this point, but only when the wave packet frequency reaches the frequency that corresponds to the plasma frequency at the beam injection point. Once this frequency is reached, the wave packet propagates without any frequency drift.

Four cases of different density gradients were studied: a) a constant background density b) a weak gradient c) the default case as used by Ref.[83] and d) a strong gradient. The characteristics of the emission mechanism were not changed by a different density profile. However, a steeper gradient means that the wave packet can reach frequencies that allow for propagation earlier, while the weak gradient has the opposite effect. In case of the constant background, no emission could escape the beam injection region, as the necessary frequencies were not reached within the simulated time. Thus we conclude, that the mode coupling, namely the cyclotron emission coupling to the allegedly z-mode, is facilitated by the *density gradient*.

We found that the intensity of the wavelet transform of E_y was proportional to the y-component of the kinetic energy of the injected beam. There was no other significant influence of the variation of the beam injection angle θ. However, in the $\theta = 90°$-

case, there was no electrostatic Langmuir wave signal found. This can be explained by the lack of a positive gradient in the distribution function with respect to parallel momentum. Nevertheless, generation of electromagnetic waves was evident. This sets the presented mechanism apart from conventional mechanisms, presented in the introduction.

Further, movies were generated to show the evolution of the distribution function in phase space. On one hand, when plotted in cartesian coordinates, gyration of the beam around the magnetic field could be seen; on the other hand, when plotted on a plane of parallel and perpendicular momentum axes, positive gradients as well as subtle dynamics of the distribution function was observed. The key finding is that, indeed, the requirement for the cyclotron maser instability, $\frac{\partial f}{\partial p_\perp} > 0$, is fulfilled throughout the simulation. Cyclotron masers in overdense plasmas ($\omega_{ce}/\omega_{pe} \ll 1$) are expected to generate waves in the z-mode, at harmonics of the electron cyclotron frequency [92].

We would like to comment, why we think there is no continuous generation of cyclotron maser emission, despite the fact that $\frac{\partial f}{\partial p_\perp} > 0$ throughout the simulation. The quasi-linear relaxation, i.e. the plateau formation shown in Ref.[63], that shuts off the instability, happens on the time scale of the inverse growth rate. The growth rate calculation of our parameter space will be presented elsewhere. The reason why the emission generation is not continuous is, that we do not replenish the beam, as it is only injected at $t = 0$. In solar flares, of course, the electron beam injection will have temporal (and spatial) extent.

The distribution function shows subtle dynamics throughout the simulation. Some correlations can be seen between the evolution of the wavelet transforms and the distribution function, such as in the initial pulsation phase as well as at the wave packet ejection point. This needs to be investigated further.

The degree of linear polarization of the escaping wave packet was strongly dependent on the injection angle. For the $\theta = 90°$-case, a left-handed polarization of the emitted wave was found. This is in line with z-mode wave generation, as the stable wave packet is actually formed below the plasma frequency and the polarization of the z-mode for $\omega < \omega_{pe}$ is left-handed [90]. At present we do not have definite proof that the generated emission is a z-mode. Such proof can be obtained by producing different numerical runs and producing (ω, k)-pairs and compare these to predictions of dispersion relations as in Ref.[90] which presents a comprehensive study, but not exactly for the same parameters, that are used here. The total generated electromagnetic field energy was of the order of 10^{-3} - 10^{-2} of the initial kinetic energy of the beam and varied as the pitch angle was altered. Ref.[65]

estimates the beam pitch angle to be only a few degrees. For a initial kinetic beam energy of 7.89×10^{-3} J and perpendicular injection, the brightness temperature would be $T_B = \frac{Ic^2}{2k_B\nu^2}$ with brightness $I = \frac{cn}{2}\epsilon_0 E^2$ and refractive index $n \approx 1$. We get $T_B = \frac{c}{2k_B}w \approx 8 \times 10^{25}$ K, which greatly exceeds values obtained from observational data, that estimate brightness temperatures to be of the order of $T_B \approx 10^{12} - 10^{15}$ K. As the electromagnetic energy w was shown to be proportional to $sin^2\theta$ and for small pitch angles $sin^2\theta \approx \theta^2$, we can deduce that only a small pitch angle of $\theta = 10^{-5}$ would suffice to achieve brightness temperatures of around 10^{15}.

The presented mechanism is relevant to solar type III radio bursts, as it is triggered by the *perpendicular* component of the electron beam, while the parallel component merely generates Langmuir waves. The present study focuses on the injection of a single beam as an initial value problem (i.e. without replenishing the beam), but in flares many beams are generated and due to the outward propagation, the cyclotron maser is triggered along the beam trajectory, which mode converts on the density gradient into the z-mode, thus generating electromagnetic emission of decreasing frequencies, that give the characteristic shape of the dynamical spectrum for type III bursts. Ref.[65] indicates that beam pitch angles are a few degrees. This means that Langmuir waves would be generated, and yet, as shown in Ref.[60] and chapter 3 of this thesis, Langmuir waves play no role in EM emission generation, because, in 1.5D, plasma emission is not possible. Reality is - of course - not 1.5D and, in higher dimensions, plasma emission will switch on; as well as the antenna mechanism, if density cavities are present. Additional studies are needed to measure relative strength/importance of the different mechanisms in different physical situations. Further analysis may also help to better understand the mechanism presented in this study. Such analysis may include the determination of the mode of the escaping emission as well as detailed analysis of the mode coupling process.

After this work was complete, we became aware of the following: (i) when a case of $T_{background} = 3 \times 10^8$ K is studied, eliminating the electron cyclotron maser (ECM) instability as $\frac{\partial f}{\partial p_\perp} < 0, \forall \mathbf{p}$, EM emission identical to the one in this study still occurs; (ii) when a ring-shaped (in p_y and p_z) beam distribution is considered, implying $\mathbf{j}_\perp = 0$, no EM emission is generated. These findings indicate that both effects - the ECM instability and EM emission from transverse currents - are present (and competing). It is probable that the ECM instability growth rate is so small that it cannot develop by the end of the simulation. Calculation of the growth rates commensurate to physical parameters of type III bursts and the ring distribution has been published elsewhere [68].

5 3D Particle-In-Cell Simulations of Electron Acceleration by Langmuir Waves in an Inhomogeneous Plasma

The main findings of this chapter have been published in [62].

5.1 Introduction

The so-called 'number problem' in the context of solar flares refers to the high number of accelerated electrons necessary in order to explain spectral observations of hard X-ray (HXR) radiation from the solar corona [1, 42]. For the requirement of 10^{38} accelerated electrons and a solar flare particle acceleration volume of $\approx 1 - 10$ Mm^3, the acceleration mechanism would have to accelerate the whole population of the solar corona in order to achieve the observed emission characteristics. No such mechanism is known or plausible. A number of theories have been put forward in an attempt to solve this problem: i) re-acceleration of already slowed down electrons in the chromosphere [11]. However, observations show that a large part of the accelerated electrons drifts towards the coronal loops rather than the chromosphere [3]; ii) formation of an electric circuit of precipitating and returning electrons [99, 100]; iii) dispersive Alfven waves propagating towards loop foot points and accelerating particles in plasmas with transverse density inhomogeneities [21, 84, 85, 87]; iv) acceleration by Langmuir waves in non-uniform plasmas, as the Langmuir spectrum drifts to smaller wave-numbers [37].

Ref.[37] presents a collisional quasi-linear theory study, which confirms that in the case of an inhomogeneous plasma, the generated Langmuir waves show a drift in k-space, which results in an increased number of electrons carrying higher energies. It investigates the interplay between particle collisions as well as Langmuir wave

generation and absorption. Qualitatively, the main argument states that a Langmuir wave, that has been generated by an electron of a given energy, will have a wavenumber k corresponding to that electron's energy. A positive density gradient in the direction of wave propagation will cause a decrease of the wavenumber, and hence higher phase velocity $v_{ph} = \omega/k$. The k-shifted wave is then subject to absorption by a faster electron. The overall effect is an increased number of high energy electrons in the energy spectrum. While the quasi-linear approach allows simulations for long time scales, fully kinetically self-consistent dynamics of the phase space distribution function of the electron population remains inaccessible. Such dynamics is of high relevance to the beam-plasma instability, which is claimed to be responsible for the generation of Langmuir waves. Ref.[35] carried out three-dimensional particle-in-cell (PIC) simulations of a mono-energetic electron beam being injected into plasma. The study successfully showed the characteristic plateau formation, along with noticeable acceleration of electrons. It suggests that the total amount of energy stored in electrons moving faster than the initial beam electrons could be (depending on simulational parameters e.g. magnetic field strength) of the order of $10-30\%$. However, Ref.[35] did not take density gradients or collisions into account, which may well alter the obtained results.
In this paper, fully relativistic, electromagnetic, collisionless 3D particle-in-cell simulations of an electron beam being injected into a Maxwellian, magnetised, non-uniform plasma are performed. This work extends Ref.[37] by the inclusion of self-consistent plasma kinetics, while it lacks the effect of collisions. Ref.[35] is extended by the inclusion of the effect of a density gradient.
In section 5.2, the parameters of the numerical runs are discussed. Section 5.3 presents results from simulations of an unbound (spatially infinite extent) beam into 3 different background plasma density profiles: i) a uniform background density; ii) a weak gradient; iii) a strong gradient. The results are then compared. In section 5.4, a study of a localized beam injected into a uniform background, as well as a strong gradient case is analysed. Conclusions are drawn in section 5.5.

5.2 Simulation Setup

All simulations, presented in this paper, use EPOCH, a fully electromagnetic, relativistic particle-in-cell code that was developed by the Engineering and Physical Sciences Research Council (EPSRC)-funded collaborative computational plasma

physics (CCPP) consortium of UK researchers.
We are considering a 3D Maxwellian plasma. The background magnetic field along the x-direction is kept constant $B = B_x = 0.003$ T= 30 G, setting the electron gyrofrequency to $\omega_{ce} = 5.28 \times 10^8$ Hz rad everywhere. The background temperature is $T = 10^6$ K in each direction and isotropic, corresponding to a thermal electron velocity of $v_{th} \approx 3.9 \times 10^6$ m/s $\approx 0.013c$. Due to computational limitations, the maximum background plasma density is $n_0 = 10^{14}$ m^{-3}, giving $\omega_{pe} = 5.64 \times 10^8$ Hz rad. This sets $\frac{\omega_{ce}}{\omega_{pe}} = 0.935 \approx 1$. Further, the corresponding electron Debye length is $\lambda_{De} = 6.9 \times 10^{-3}$ m. The simulation setup is such that $x_{max} = 10000\lambda_{De}$ and $y_{max} = z_{max} = 10\lambda_{De}$, while the grid size is λ_{De}.
A beam of accelerated electrons is injected at simulation time $t = 0$. It carries a momentum of $p_b = p_{b,x} = m_e\gamma\frac{c}{2}$ with the Lorentz factor $\gamma \approx 1.155$, while $p_y = p_z = 0$. The beam is mono-energetic. The beam electrons are not replenished, i.e. there is only an injection at $t = 0$ and no further electrons are being added at any other point in the simulation. As a result of the above defined quantities, at $x = 0$, the plasma beta is $\beta = 3.86 \times 10^{-4}$. The mass ratio used is $m_i/m_e = 1836$. We will consider cases where the beam density is uniform in the plasma box, as well as cases where the beam is spatially localized. Each particle species (background electrons, ions, and beam electrons) is represented by 100 pseudo particles per cell. The boundaries of the simulation box in the perpendicular directions (y and z) are periodic for waves and particles alike, however, along the x-axis boundaries are periodic for particles, but we use open boundaries for waves. On one hand, this allows us to keep the total number of beam particles constant throughout the simulation. On the other hand, waves that were generated at the boundaries of the simulation box and travel through the boundary will not be re-introduced at the other side. This is particularly important in runs with density gradients, because, if periodic boundary conditions were being used, these waves would encounter a sudden (non-physical) change in background density at the boundary and interact via refraction. Moreover, these waves would spread out into the simulation box and interfere with the results. This does introduce loss of energy that is carried by waves that escape the simulation box, but the loss does not turn out to be significant. In order to be able to compare runs with different background plasma frequencies, we will normalize all units (where appropriate) to the above defined quantities. Time is normalized to ω_{pe}^{-1}, space to c/ω_{pe}, electric field to $\omega_{pe}cm_e/e$.

5.3 Unbound Beam Injection

In this section, a beam of constant density is injected evenly distributed in the simulation box. The background density profiles are being varied in order to study the effects of density gradients on the acceleration mechanism. The density profiles can be represented by

$$n_e(x) = n_{w,s} \exp[2x/L] \tag{5.1}$$

with L and $n_{w,s}$ being chosen for each run such that the density increase from the left boundary to the right is a factor of 3 for the *weak gradient* case (corresponding to n_w), respectively 10 for the *strong gradient* case (corresponding to n_s). This density profile is similar to the one chosen in Ref.[37]. Additionally, we consider a run with *constant background density*, n_c. For the constant density case, a beam to plasma ratio of $n_b/n_c = 0.05$ was chosen. The parameters $n_{w,s}$ and n_b were determined by making sure that n_b and the average Langmuir wave growth rate, $\gamma_{LM} \propto n_b/n_e$, are equal in all runs. This ensures that the runs are comparable, as the same amount of energy is injected into the plasma in all runs, while the overall growth rate for the Langmuir waves is also equal in all runs. Naturally, in the non-zero gradient runs, local growth rates will differ from the overall rate. Furthermore, EPOCH requires the grid size to be smaller or equal to the Debye length. The grid size is set to be constant throughout the box and its value was set in the previous section. As a result, the density at the right edge of the simulation box is set to the maximum density, $10^{14}\mathrm{m}^{-3}$, fulfilling the requirement everywhere. This yields $n_b = 1.954 \times 10^{12}\mathrm{m}^{-3}$ for all runs.

5.3.1 Constant Background Plasma

The constant background density is $n_c = 3.91 \times 10^{13}$ m^{-3}. Injecting a uniform beam into the plasma generates a constant flow of electrons throughout the simulation box. As the background distribution is Maxwellian, the beam will introduce a return current throughout the box from the start of the simulation. This current will cause a standing wave, visible in the E_x-component of the electric field. The frequency of this wave is the local electron plasma frequency. It is possible to start from a zero current situation by introducing a backward drift of the background plasma to balance out the current produced from the beam electrons. However, the local backwards drift would be a function of the local beam-to-background electron ratio, $v_e = -v_b n_b/n_e$, and in the case of background density gradients, it would also cause

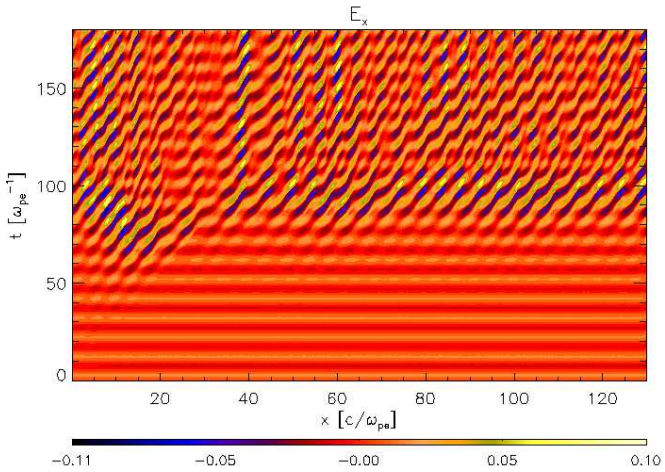

Figure 5.1: Time-distance plot for E_x for constant background density and uniform beam injection along the x-direction; $y = z = 5\lambda_{De}$.

different parts of the background plasma to drift at different velocities, which would influence the simulation results. Effectively, denser regions would be drifting slower than less dense ones, which would distort the density profile more and more over the course of the simulation, making the analysis of the role of the density gradient impossible. Therefore, we would like to keep simulations with different background density profiles as comparable as possible, changing only a minimal amount of parameters. Conveniently, it turns out that the amplitude of the wave, which is being generated by the non-zero initial current, is overpowered by the generated Langmuir waves in all runs, when given enough time for the beam-plasma instability to take effect.

Electric Field Evolution

Movie 1 in Ref.[62] shows the evolution of the beam and background densities over the course of the simulation. We can see that despite the constant density ratios everywhere, wave growth occurs first from the left side of the simulation box. This is probably due to the not 100% smooth periodic boundaries, which might prove just enough distortion to jump start the Langmuir wave growth. Fig.5.1 shows the time-distance plot for the x-component of the electric field along the x-direction; $y = z = 5\lambda_{De}$. Clearly, there is only little excitation of the electric field in the early stages of the simulation, where only effects due to the non-zero initial current take place. After $\approx 70\omega_{pe}^{-1}$ waves are being generated due to the beam-plasma insta-

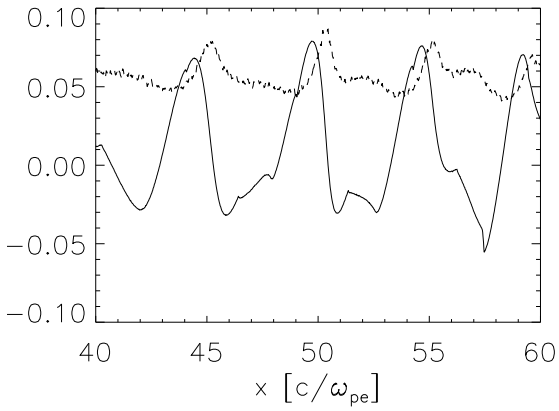

Figure 5.2: $E_x(x)$ (solid) and $n_e(x)$ (dashed) at $t = 100\omega_{pe}^{-1}$, zoomed in and arbitrary units on the y-axis for clarity.

bility. The Langmuir waves can be clearly distinguished due to their propagation, opposed to the stationary nature of the waves generated by the non-zero current. Fig.5.2 compares snapshots of E_x (solid) and n_e (dashed) at $t = 100\omega_{pe}^{-1}$. It can be deduced that the shown waves are electrostatic, as they clearly follow Gauss' law, $\nabla \cdot \mathbf{E} = \rho/\epsilon_0$. Maxima and minima in the electron density profile correspond to the points of maximum gradient in the E_x profile. The fact that the waves fulfil Gauss's law shows that the waves are electrostatic, i.e. Langmuir waves. Fig. 5.3 shows the 2D-Fourier transform spectrum of Fig. 5.1. Predominantly, waves are being excited at the average plasma frequency, $\tilde{\omega}_{pe}$. Note that ω_{pe} always refers to the value given in the section 5.2 and is chosen in order to be able to compare time scales in different runs, whereas $\tilde{\omega}_{pe}$ is run-specific and allows investigation of e.g. run-specific dispersion relations. The figure shows a maximum roughly at the intersection of the two curves representing the dispersion relation of Langmuir waves, $\omega = \sqrt{\tilde{\omega}_{pe}^2 + 3v_{th}^2 k^2}$, and resonance condition for the beam plasma instability, $\omega = kv_b$.

Distribution Function Dynamics

In this section, the dynamics of the electron velocity distribution function is discussed. According to quasi-linear theory, a distribution that is unstable to the beam-plasma instability will generate Langmuir waves, while the electron distribution function relaxes to a plateau shape. The essential requirement for wave growth is that the distribution function in phase space shows a positive slope in the forward

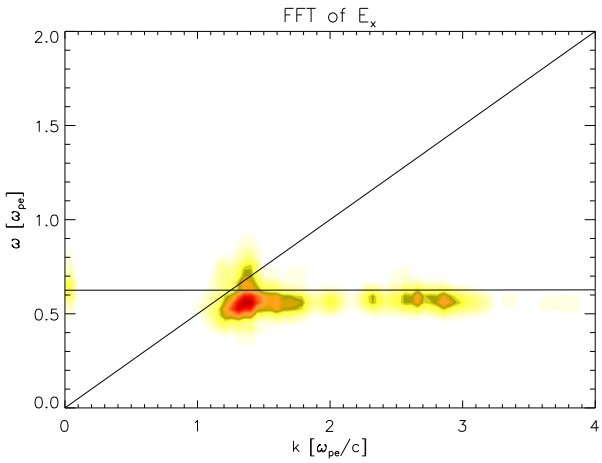

Figure 5.3: Fast-Fourier transform of E_x for constant background density and uniform beam injection. The curves represent the dispersion relation for Langmuir waves, $\omega = \sqrt{\tilde{\omega}_{pe}^2 + 3v_{th}^2 k^2}$ ('horizontal' curve), and the resonance condition for the beam plasma instability, $\omega = kv_b$.

direction with respect to the magnetic field, $\frac{\partial f(v)}{\partial v_\parallel} > 0$. As soon as the plateau is formed, this condition is no longer fulfilled and no more waves can be generated via this instability. The electron velocity distribution function allows us to deduce the distribution of electrons with respect to their kinetic energy, see Fig.5.4. The figure shows snapshots of $f(E_{kin}, t)$ at different times in the simulation. The chosen times are representative of the initial situation, the phase of wave generation and a formed plateau at a later stage in the simulation. The initial distribution shows a Maxwellian background distribution as well as the mono-energetic beam, represented by the diamond. From Fig.5.1 we can see, that the Langmuir wave growth starts around $70\omega_{pe}^{-1}$. The distribution function at this stage (Fig.5.4b) shows a clear deviation from the initial distribution, namely broadening of both the beam and the background distribution and a tendency towards plateau formation. At $t = 120\omega_{pe}^{-1}$, there is already a plateau formation clearly visible (Fig.5.4c). The plateau stabilizes and is still present at much later times in the simulation (Fig.5.4d). Clearly, from the point of wave generation, the amount of high energy electrons increases, which is in line with results in Ref.[35]. Further, it can be clearly seen that some electrons are even accelerated beyond their initial injection speed and, therefore, gain energy.

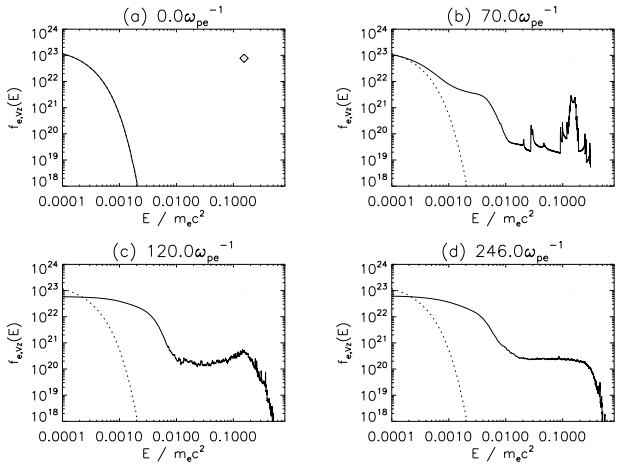

Figure 5.4: Snapshots of the electron distribution function (solid) with respect to energy for constant background density and uniform beam injection. Dotted curves track the initial distribution at $t = 0$. For clarity, the beam population is stressed by a diamond in the top left panel.

5.3.2 Weak Gradient Case

According to quasi-linear theory, the background density gradient is expected to alter results significantly [37]. Wave dissipation and refraction should be enhanced. The weak gradient case shows an increase of background plasma density from the left edge of the simulation box to the right by a factor of 3, $n_{e,R}/n_{e,L} = 3$. The shape of the density profile is defined by Eq.5.1, with $n_w = 2.147 \times 10^{13}$ m^{-3} and $L = 18204.8\lambda_{De}$.

Electric Field Evolution

It is conceivable from movie 2 in Ref.[62], that wave growth starts earliest at the left edge of the simulation box, i.e. where wave growth is most likely. Eventually, waves are being generated everywhere in the plasma. It can be immediately seen that the initial oscillations due to the non-zero initial current is no longer uniform. However, it is still overpowered by the Langmuir wave power. The introduction of a density gradient varies the Langmuir wave growth rate accordingly. Therefore, it is to be expected that wave growth on in the left part of the simulation box (where the density is now lower) should occur earlier than in the previous section. Fig.5.5 shows the evolution of E_x. We can observe waves as early as $\approx 40\omega_{pe}^{-1}$ in the less dense left part of the simulation box, while further to the right waves are being

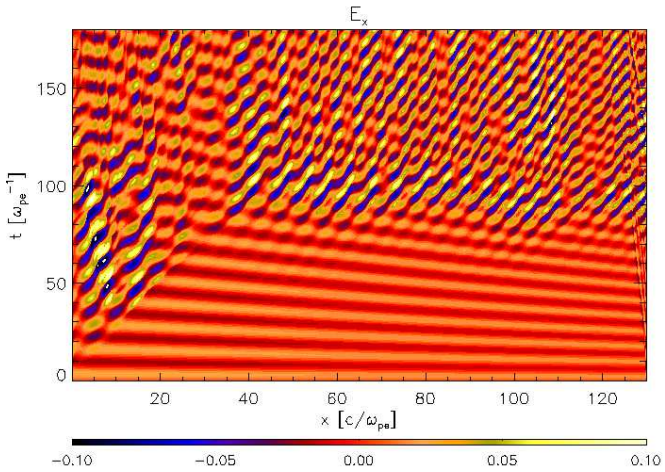

Figure 5.5: As in Fig.5.1 but for the weak gradient case.

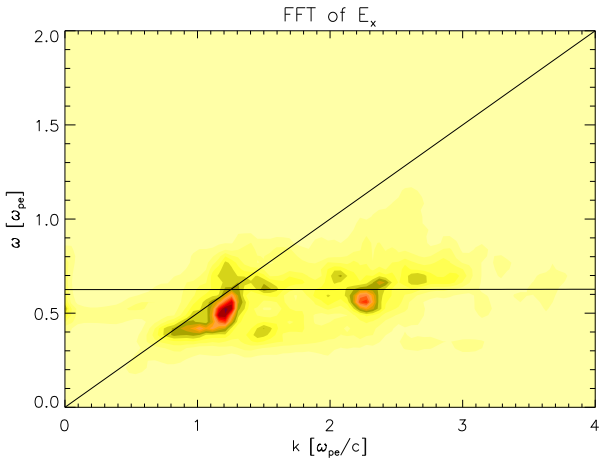

Figure 5.6: As in Fig.5.3 but for the weak gradient case.

generated at a later stage in the simulation. Fig.5.6 is the Fourier transform of Fig.5.5. It shows that wave growth is no longer as confined in (ω,k)-space as it used to be for the constant density case. This is to be expected as the maximum growth will occur at all intersection points of the Langmuir wave dispersion relation with the beam mode. The Langmuir wave dispersion relation is a function of the local plasma frequency and therefore, also a function of density. In Fig.5.6 the 'horizontal' curve follows the dispersion relation according to the mean plasma frequency, in order to give some kind of indicator as to what frequencies are present. Different local plasma frequencies will give intersection points with the beam mode. As wave growth occurs earlier in less dense regions, the wave power is expected to be stronger in the lower frequencies, which is consistent with what can be gathered from Fig.5.6.

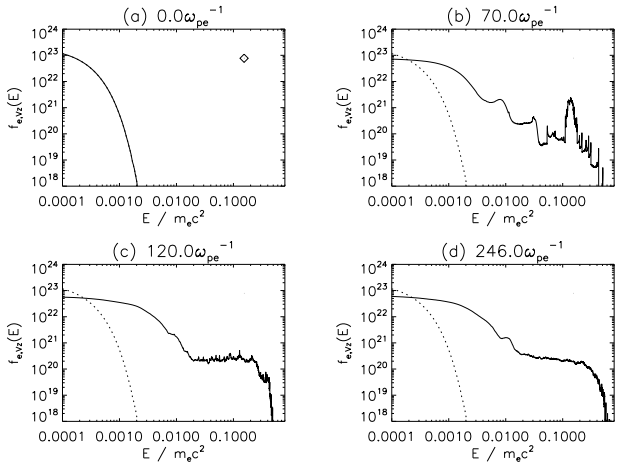

Figure 5.7: As in Fig.5.4 but for the weak gradient case.

Distribution Function Dynamics

Fig.5.7 shows the electron distribution function for the weak gradient case. The overall distribution shows evolution similar to the constant density one. There seems to be an increased broadening of the background distribution, i.e. heating of the background plasma.

5.3.3 Strong Gradient Case

The strong gradient case is defined as a 10-fold increase of density from the left edge of the simulation box to the right, $n_{e,R}/n_{e,L} = 10$. The relevant parameters for Eq.5.1 are $n_s = 10^{13}$ m^{-3} and $L = 8685.89\lambda_{De}$. Movie 3 in Ref.[62] shows the evolution of the densities. Figs.5.8-5.10 show results corresponding to the strong gradient case. Fig.5.8 shows a yet more complex picture of the E_x-component. The increased density gradient gives rise to a wider range of excited frequencies, see Fig.5.9. General behaviour of the distribution functions is along the lines of the weak gradient, but heating is yet more pronounced. Additionally, the fraction of accelerated electrons is larger, which is shown more evidently in the following section.

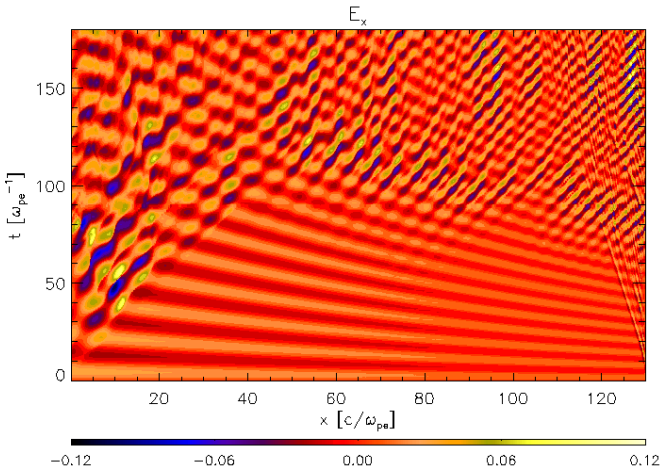

Figure 5.8: As in Fig.5.1 but for the strong gradient case.

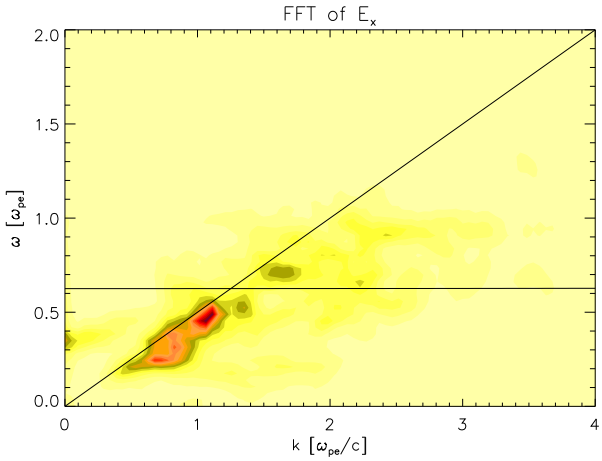

Figure 5.9: As in Fig.5.3 but for the strong gradient case.

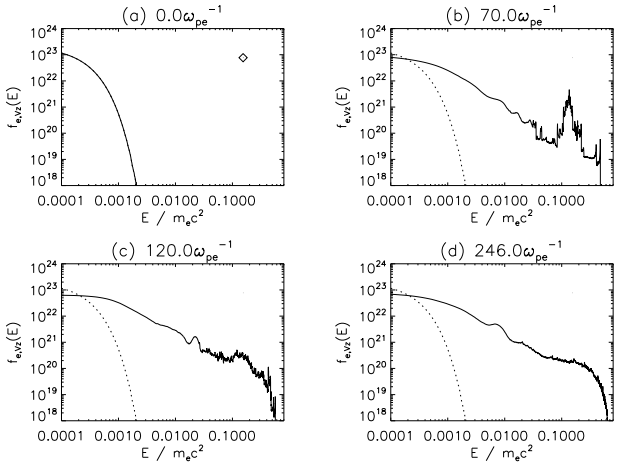

Figure 5.10: As in Fig.5.4 but for the strong gradient case.

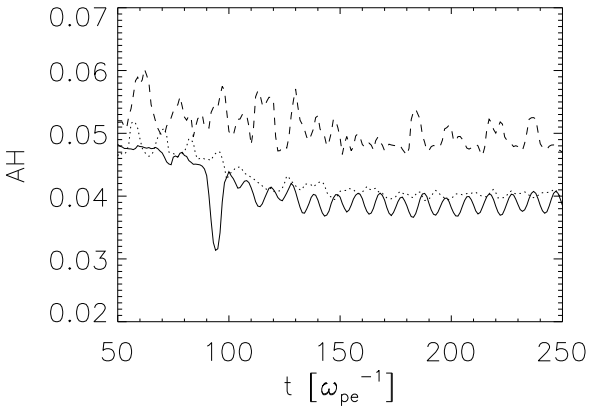

Figure 5.11: Fraction of electrons with energies higher than $(15v_{th})^2 m_e\gamma$, as calculated by use of Eq.5.2, over time for constant background density (solid), weak gradient (dotted), strong gradient (dashed).

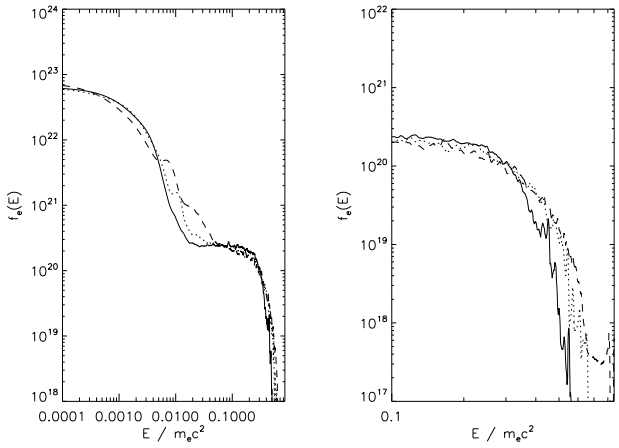

Figure 5.12: Left: Final simulation snapshots of Figs.5.4 (solid), 5.7 (dotted), 5.10 (dashed) plotted for comparison. Right: Zoomed in on high energy tail for clarity.

5.3.4 Comparison

In order to quantify the acceleration efficiency, we calculate the amount of electrons that have energies higher than $E^*_{kin} = (15v_{th})^2 m_e \gamma$. This number is calculated as a share of the total number of electrons in the system and followed over time, i.e.

$$AH = \frac{\int_{E^*_{kin}}^{E^{max}_{kin}} f(E_{kin})\,\mathrm{d}E_{kin}}{\int_{0}^{E^{max}_{kin}} f(E_{kin})\,\mathrm{d}E_{kin}}. \tag{5.2}$$

Early stages of the simulation, when effects due to the non-zero initial current dominate, are disregarded. The corresponding graph is shown in Fig.5.11. Clearly, the gradient has the effect of increasing the fraction of accelerated particles. While the weak gradient curve (dotted) tends to sit just on top of the constant density one (solid), the strong gradient case (dashed) lies much higher. Fig.5.12 shows that the gradient not only increases the share of accelerated particles, but accelerates particles to higher energies, respectively velocities.

Fig.5.13 shows the time evolution of respective energies for the various runs. Fig.5.13a shows a total energy conservation check. It plots the quantity $[E(t) - E(0)]/E(0) = \Delta E/E(0)$, giving the change of total energy normalized to the initial total energy in the system as a function of time. We obtain similar results for all runs, with a maximum energy error of $\Delta E/E(0) \approx 10^{-6}$, which is a satisfactory value for the energy conservation. The panels (b), (c) and (d) of Fig.5.13 show the interplay between kinetic energies of particles and Langmuir wave energy. It should

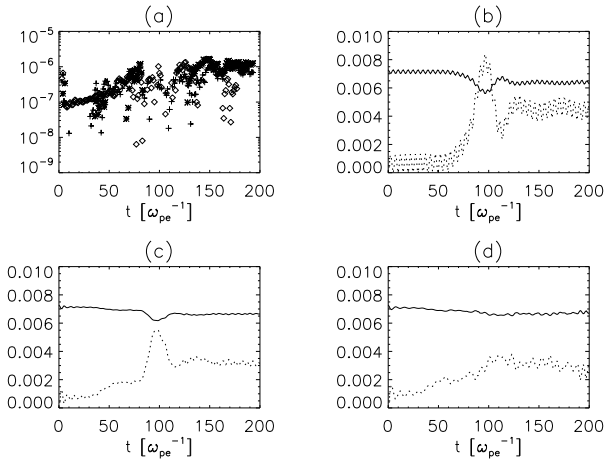

Figure 5.13: (a): $[E(t) - E(0)]/E(0)$ for constant background (diamond), weak gradient (cross), strong gradient (asterisk). (b): kinetic particle energy (solid) and Langmuir wave energy (dotted) for constant background. Langmuir wave energy multiplied by a factor 5 for clarity. (c): as top right but for weak gradient. (d): as top right but for strong gradient.

be noted, that for clarity of the plot, wave energies have been multiplied by a factor 5. Fig.5.13 shows that, the particle energy is (partially) converted into wave energy and then transferred back to the particles. From Fig.5.13b and Fig.5.13c, it should be noted, that at around $\approx 100\omega_{pe}^{-1}$ the Langmuir wave energy has a pronounced peak. This is the consequence of Langmuir wave growth via the beam plasma instability seen in Figs 5.1 and 5.5. In the strong gradient case (Fig.5.13d) Langmuir wave growth seems less vigorous (see Fig.5.8). However, as can be seen in Fig.5.15 this is offset by the effect of drift in k-space towards lower wavenumbers k. Note that despite the fact that Langmuir waves are accelerating electrons, the net electron kinetic energy is decreasing. This is because the initial beam energy is converted to produce Langmuir waves. However, overall the drift in k-space produces a significant population of highly super-thermal electrons. The k-space drift will be discussed in section 5.4.

5.4 Localized Beam Injection

In the previous section, it was established that the background density gradient has a clear effect on the fraction of accelerated electrons. It was also shown, that Langmuir waves were being generated via the beam-plasma instability. Ref.[37] shows that in their study Langmuir waves would drift to smaller wavenumbers k, allowing them

to increase their phase speed, $v_{ph} = \omega/k$, and, therefore, being subject to absorption by faster electrons. In the previous section, it was impossible to tell if such a drift was actually present. The reason being, that due to the non-localized nature of the beam, waves were being generated everywhere in the plasma. Hence, at every point along x waves of different k were *excited*, interfering with travelling waves from other sources in the plasma, which would *drift* to the wavenumber in question. In order to analyse if such a drift takes place, a localized beam was injected and left free to penetrate the plasma. A case with constant background density (as section 5.3.1) was considered along with the strong gradient case used in section 5.3.3. The beam peak density is given by the beam density in the previous sections. However, the beam has a finite width and its density profile is given by

$$n_b(x) = n_b \exp[-[(x - x_{max}/25)/(x_{max}/40)]^8]. \tag{5.3}$$

5.4.1 Constant Background Plasma

Injection of a spatially localized beam generates a current at the beam injection region. Everywhere else in the box, the initial parameters correspond to a zero-current state. Therefore, in the beam injection region, a standing wave can be observed from the start of the simulation. This wave oscillates at the electron plasma frequency. It is undesirable to include information from this standing wave when performing a Fourier analysis, thus we consider only the region to the right of the beam injection, i.e. the region the beam (and waves) is (are) travelling into. We also cut off redundant regions on the right, where the waves never make it to during the course of the simulation. Fig.5.14 shows the results of the simulation. Fig.5.14a shows the E_x component. The plot shows clear waves that are being excited on the left edge (or just beyond) and travelling towards the right. It is already noticeable that the slopes of the waves change as they propagate. Fig.5.14b shows the background density evolution, maintaining the correlation to the electric field via Gauss's law. Fig.5.14c shows the time evolution of the spatial Fourier transform of E_x. In the case of constant background density, we expect wavenumber drifts to be a result of non-linear wave-wave interactions (see Ref.[37] and references therein). We can see a clear tendency of wave power being shifted, as well as damped i.e. re-absorbed by plasma particles, leading to energy redistribution among electrons. It should be

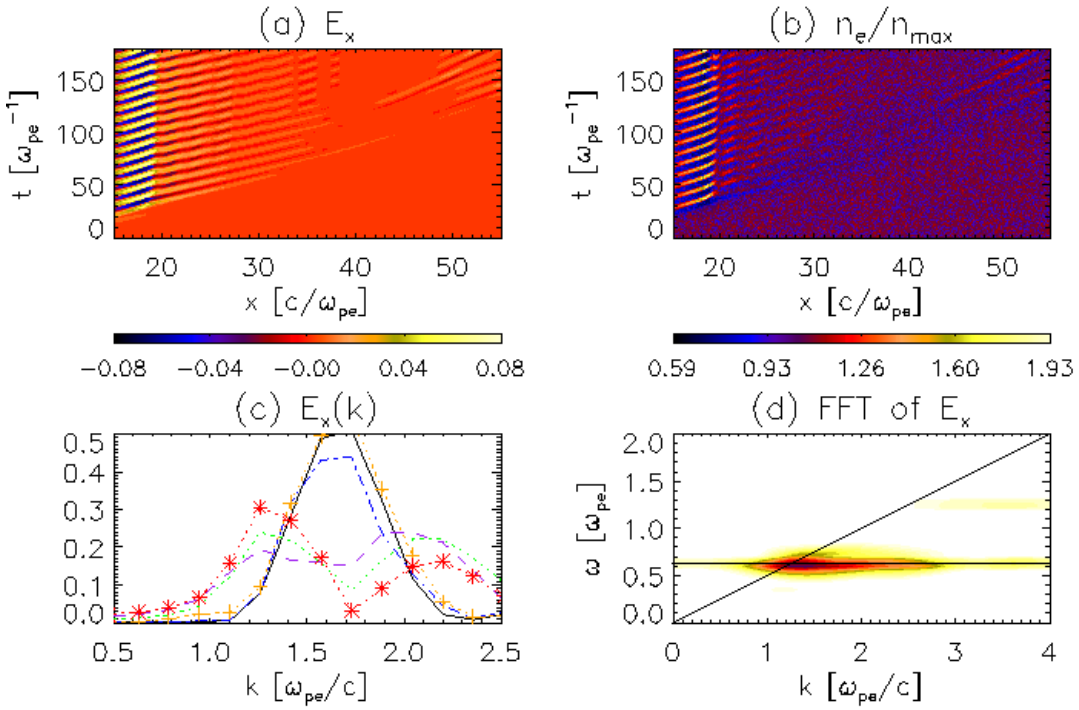

Figure 5.14: Localized beam injection with constant background density. (a): time-distance plot for E_x component. (b): time-distance plot for background electron density. (c): $E_x(k)$ for $t = 42\omega_{pe}^{-1}$ (solid, black), $t = 60\omega_{pe}^{-1}$ (dashed, purple), $t = 87\omega_{pe}^{-1}$ (dash-dotted, blue), $t = 105\omega_{pe}^{-1}$ (dotted, green), $t = 122\omega_{pe}^{-1}$ (dotted with +, orange), $t = 140\omega_{pe}^{-1}$ (dotted with *, red). Y-axis in arbitrary units. (d): 2D Fourier transform of $E_x(x,t)$. Note that for clarity in panel (d), the color scheme is inverse to the ones in the upper row and units are arbitrary.

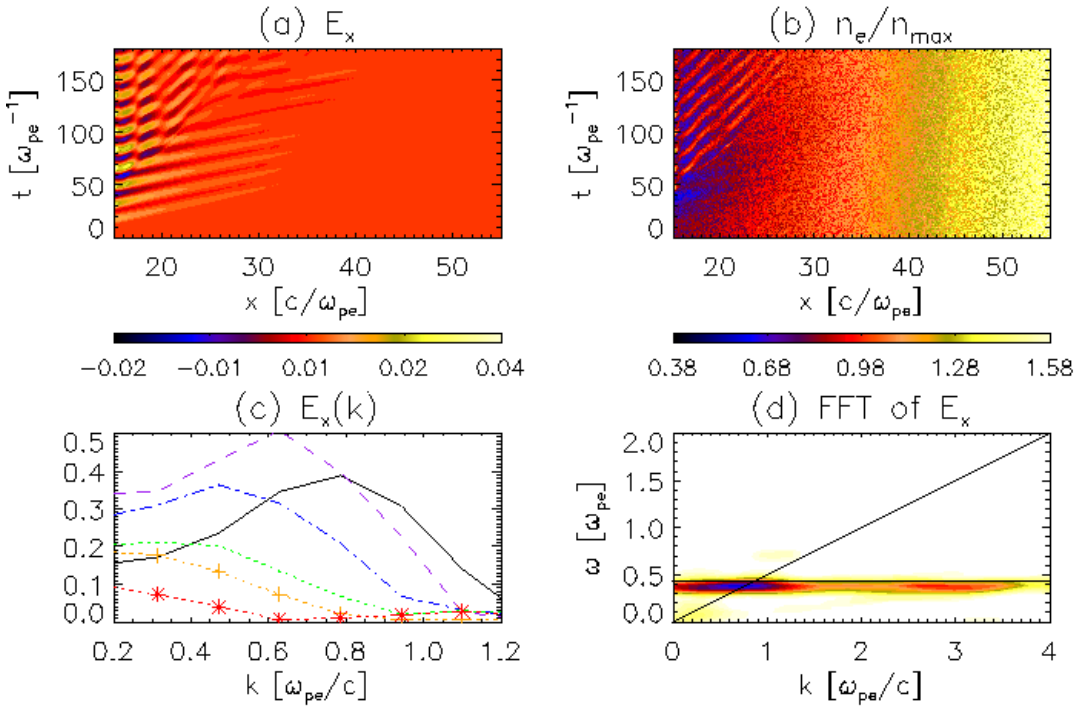

Figure 5.15: As Fig.5.14 but for the strong gradient case.

noted that, this is similar to the results in Ref.[35]. Fig.5.14d shows the full 2D Fourier transform of $E_x(t)$ (i.e. of Fig.5.14a). The curves follow Langmuir wave dispersion relation and the beam resonance condition. The majority of waves are clearly being generated at the intersection of the curves.
Movie 4 in Ref.[62] shows the evolution of the densities for a localized beam injection into constant background plasma. Clearly the beam is dispersed as it propagates due to quasi-linear relaxation. At one occasion the beam density even overcomes that of the background, resulting in a strong signal in the top panels of Fig.5.14. Soon the peak density of the beam is reduced and wave growth is no longer favourable, hence, Fig.5.14 shows propagating waves, but no new wave generation.

5.4.2 Strong Gradient Case

The introduction of a background density gradient is expected to have a strong influence on the outcome of this study, as it amplifies the roles of wave dissipation and refraction. Fig.5.15 shows that - similar to the constant density case - waves are being generated on the left edge of the plot (or just beyond) and propagate towards

the right. However, we can immediately see, that those waves are no longer allowed to propagate as far, due to the density gradient. The key feature of the plot is Fig.5.15c, where one can clearly see, that the k-drift shows a clear shift to smaller wavenumbers over time. The wave power drifts from $\approx 0.6\omega_{pe}/c$ to $\approx 0.4\omega_{pe}/c$, where evident damping occurs. Also, in line with Fig.5.15d, excited wavenumbers are smaller due to the shifted resonance condition in the region of interest. Movie 5 of Ref.[62] shows the evolution of the densities. Similar to the constant case, the beam is dispersed and its peak density is strongly decreased as it propagates through the plasma.

5.5 Conclusions

The main goal of this study was to explore a mechanism that offers a potential solution to the problem of high intensity hard x-ray (HXR) emission observable during solar flares. This study seeks to extend previous work done in the field. A previous collisional quasi-linear theory study [37] showed the importance of a background plasma density gradient, while a previous PIC analysis [35] offered a fully kinetically self-consistent investigation. This study extends Ref.[37] by the use of a self-consistent, fully kinetic approach and extends Ref.[35] by introduction of a background plasma density gradient. The observed HXR spectra are thought to be evidence of a large population of high energy electrons, which are thought to be a result of Langmuir wave generation and absorption. This study sheds light on how a background density gradient influences the electron acceleration process in the fully kinetic regime. 3D fully relativistic, electromagnetic particle-in-cell (PIC) simulations with realistic mass ratio were performed. A mono-energetic beam of high energy electrons was injected into a magnetized, Maxwellian, homogeneous and inhomogeneous plasma. The initial electron distribution function in phase space has a bump in the forward direction, making the system unstable to the beam-plasma instability. Quasi-linear theory suggests that such a situation will allow Langmuir wave growth with subsequent plateau formation in the distribution function. Both effects were successfully demonstrated in our simulations. Waves were identified to be electrostatic by fulfilling Gauss's law. Generation of waves was shown to happen at the resonance of the dispersion relation for Langmuir waves and the beam mode. The main focus of the present study was to investigate the role of the background density gradient in the context of the acceleration of electrons.

Three different cases with unbound beam injection were investigated: a) a constant background; b) a weak density gradient, $n_{e,R}/n_{e,L} = 3$; c) a strong gradient case, $n_{e,R}/n_{e,L} = 10$. It could be shown that the strong gradient case produced the largest fraction of electrons that have velocities above $15v_{th}$. The weak gradient case also showed an increased number of high energy electrons. Further, two runs with localized beam injections were performed in order to analyse wave properties such as wavenumber drifts. The spatially localized beam was injected into both a constant background density profile, as well as a strong gradient one. The evolution of the wave power with respect to the wavenumber k was analysed. It was shown that the Langmuir wave power indeed drifts to smaller wavenumbers, which is in line with a previous quasi-linear theory study [37]. It should be noted, that computational constraints only allow us an investigation of a density rise of a factor $n_{e,R}/n_{e,L} = 10$, whereas in a real situation, where electrons race down coronal loops from a flare region towards the chromosphere, the density increase would be a factor of $\approx 10^4$. The cumulative effect of this much larger density increase would be a much larger number of accelerated electrons, which could potentially account for the observed HXR radiation. Despite the fact that the main focus of this paper was the HXR emission in the solar flare context, all findings are also likely to be applicable to the Earth bow-shock [38, 58, 96].

6 Summary and Outlook

This thesis treats particle acceleration and related electromagnetic wave generation and absorption in homogeneous and inhomogeneous plasmas. Plasma parameters were chosen to be representative of the solar chromosphere and corona. Wave absorption was treated as an effect of electron-neutral collisions and the resulting heating was the primary interest in chapter 2. Wave generation was considered in the context of plasma instabilities (in this case via beam injection into magnetized plasma, e.g. beam-plasma instability, ECM, ...) and studied in chapters 3, 4 and 5. Additionally, chapter 5 quantified particle acceleration due to wave-particle interaction within the context of solar flares.

Chapter 2 formulated a model for the heating of solar chromospheric internetwork regions. Qualitatively, the chromosphere was split into slabs of plasma, while in each slab physical parameters were kept constant. The parameters within the slabs were chosen in accordance with the VAL C model of Ref.[88]. Electromagnetic (EM) waves that originate from the photospheric blackbody radiation are thought to be absorbed in the chromosphere. Instead of solving radiative transfer equations, the plasma slab model was used to study the proposed mechanism by means of calculation of (frequency dependent) reflection and transmission coefficients on the slab edges and absorption coefficients within the slabs according to Ref.[77]. The irradiance spectrum of the solar photosphere was well described by a blackbody and its frequency (respectively wavelength) dependence was given by the Planckian brightness function with a temperature corresponding to the photospheric surface, i.e. 5762K. The absorption mechanism was provided by the electron-neutral collisions. Electrons oscillate in the EM wave field and electron-neutral collisions damp the EM wave. The electron cyclotron resonance could be ignored. However, there is a possibility of additional contributions to collisions due to microturbulence. This effect has been taken into account by introduction and variation of a parameter in the calculation of the absorption coefficients. Generally, the applicability of the proposed model was justified by the fact that the solar irradiance spectrum that arises from the photosphere is excellently described by a blackbody in the relevant frequency interval and previous plausible works (see e.g. Ref.[28]) had used assumptions of local

thermodynamic equilibrium (LTE) in models for the photosphere likewise, which is known to be imperative for the use of the Planckian brightness function. Nevertheless, an important note is that chromospheric radiative *losses* can only be described by consideration of non-LTE effects. The strong radiation fields of the chromosphere is known to affect the occupation rate of atomic energy levels, resulting in radiative loss [54]. However, the steady inflow of energy from the photosphere allows for the chromospheric *heating* to be considered as a LTE process.
Given the uncertain nature of the collision cross-section due to the plasma microturbulence, it was shown that for plausible physical parameters, the heating flux produced by the absorption of EM waves in the chromosphere is between 20% and 45% of the chromospheric radiative loss flux requirement. It is also established that there is a value for the collision cross-section, $5 \times 10^{-18}\mathrm{m}^2$, which produces the maximal heating flux of 1990 Wm^2. Further conclusions could be drawn from calculated results: i) plasma resistivity measurements in the current sheet of the Magnetic Reconnection Experiment in Ref.[80] suggested that the resistivity can be of an order larger than the Spitzer resistivity, i.e. an order of magnitude higher than expected. Along with our findings, it would not be unlikely that collisional cross-sections in the chromosphere could take on anomalous values; ii) it is evident from Ref.[73] that on timescales of a month and longer, the total solar irradiance shows good correlation with the Mg-index (chromospheric excess radiation relative to the photosphere). This is in accordance with the presented model, since it was taking the photospheric spectrum as the source of free energy that is injected into the chromosphere. On shorter timescales, however, effects from sunspots, faculae and plages would not average out in the spectrum and result in decorrelation; iii) our model showed only a weak dependency of the absorption coefficients on the magnetic field strength. Hence, unlike in the photosphere, brightness of chromospheric radiation should not be decreasing with an increase in magnetic field. Ref.[69] showed observational evidence of chromospheric brightness is weakly increasing with the magnetic field. This was shown by measurements of CaIII K line core contrast. In the photosphere this contrast initially increases up until values of 0.02T, but decreases rapidly for higher field strengths. The rise of brightness with increasing field could be a result of high densities in flux tubes in the low field strength regime, while for higher fields a slower rise was due to quenched wave activity [73]. The average horizontal flow speeds were shown to be subdued by strong magnetic fields in granules [78].

Chapter 3 focused on the generation of electromagnetic waves from an electron beam injected into magnetized plasma. It aimed to explore the novel mechanism of elec-

tromagnetic wave generation by the perpendicular component of the beam injection momentum. In chapter 3, the mechanism is introduced and put in a general context (e.g. applications in magnetrons, radars), while in chapter 4 a parametric study is performed for parameters corresponding to solar type III radio bursts. Ref.[83] had shown that oblique beam injection with respect to the background magnetic field results in EM wave generation. Therefore, in this thesis 1.5D particle-in-cell simulations of a hot, low density electron beam injected into magnetized, maxwellian plasma with a density gradient were carried out. The choice of 1.5D prohibited any kind of wave generation from the conventional plasma emission [27], because it would require at least two spatial dimensions. Further, the lack of density cavity formation made it impossible to generate EM waves from the antenna mechanism [45]. In chapter 3, the beam was injected completely perpendicularly to the background magnetic field, turning off all electrostatic Langmuir wave generation. As a result, all of the previously well known emission mechanisms were 'turned off'. However, the EM field components showed clear wave formation, confirming that the perpendicular beam momentum evokes EM waves. Additionally, it also results in a bump in the perpendicular direction of the electron distribution function in phase space, giving rise to the electron cyclotron maser (ECM) instability. The ECM is known to produce waves at the electron cyclotron frequency [92]. For the considered parameters, the cyclotron frequency at the beam injection region is far below the local plasma frequency, which causes generated waves to decay again. The generation-and-decay process continues until a stable wave packet can be formed and drifts along the density gradient to higher frequencies. Eventually, the frequency of the wave packet reaches frequencies of the order of the plasma frequency, which allows the wave packet to escape. For the used simulation parameters, the ECM is expected to generate z-mode waves, which are able to propagate slightly below the plasma frequency. The observed behaviour of the wave packet suggests that it is indeed a z-mode wave, as the propagation clearly starts below the plasma frequency. The generation of emission was not expected to be continuous - even though the quasi-linear relaxation and correlated plateau formation of the electron distribution function was not achieved - due to the fact that the beam was injected at time $t = 0$ only and beam electrons were not replenished. In a real situation featuring a beam of finite spatial and temporal extent, the mechanism would be triggered along the propagation path of the beam and, therefore, produce characteristic emission spectra of e.g. type III radio bursts. It should be noted, that in a real 3D environment, all other previously known mechanisms of EM wave generation from beam injection (which, in our simulations, have been turned off by the choice of parameters) will

contribute to the overall emission as well.

Chapter 4 presented a parametric study of the new found mechanism. In particular, effects of the beam injection angle as well as different background plasma density gradients were investigated. These different density gradients were studied: a) a constant background density b) a weak gradient c) the default case as used by Ref.[83] and d) a strong gradient. The main behaviour of the emission mechanism was not changed by the choice of an alternate density profile. However, as the stable wave packet rose in frequency, cut-off frequencies for steeper gradients could be reached earlier, while a weaker gradient has the opposite effect. No emission could escape the beam injection region, when the background plasma density was kept constant, as the necessary frequencies were not reached within the simulated time. Thus we conclude, that the density gradient plays an integral part in the EM emission generation.

The beam injection angle with respect to the background magnetic field was varied in order to investigate correlations with the EM field generation. It could be shown that the intensity of the perpendicular EM field wavelet transform of E_y was proportional to the corresponding beam kinetic energy. Further, for a $\theta = 90°$ injection there were no Langmuir waves excited (as stated in chapter 3), but as soon as the parallel component of the beam momentum was non-zero, Langmuir waves were generated. The degree of linear polarization of the escaping wave packet was found to be very sensitive to the beam pitch angle. For the $\theta = 90°$-case, the wave was determined to be left-hand polarized. This is in line with z-mode wave generation in the sense that the stable wave packet is actually formed below the plasma frequency. Ref.[90] predicts the polarization of the z-mode for $\omega < \omega_{pe}$ to be left-handed.

Definite proof of whether or not the z-mode is actually excited was suggested to be obtained by producing different numerical runs and producing (ω, k)-pairs and compare these to predictions of dispersion relations as in Ref.[90]. This was not within the scope of the presented thesis. The evolution of the distribution function in phase space, when plotted in cartesian coordinates, shows gyration of the beam around the magnetic field; when plotted on a plane of parallel and perpendicular momentum axes, positive gradients as well as subtle dynamics of the distribution function was observed. The requirement for the cyclotron maser instability, $\frac{\partial f}{\partial p_\perp} > 0$, is fulfilled throughout the simulation. However, one should note that additional studies have shown that the ECM is competing with EM generation from perpendicular currents [68]. A definite analysis of which mechanism contributes how much to the overall emission is subject to further studies, which were not part of this thesis. Further, the 1.5D geometry could be extended to 3D in order to quantify how the presented

mechanism competes against the conventional mechanisms.

The thesis closed with a study of particle acceleration in association with wave generation. While in the previous chapters the main focus was put on the wave generation and absorption processes, in chapter 5, closer attention was devoted to the evolution of particle distribution functions in momentum space. Specifically, a possible solution to the unexplained high intensity hard x-ray (HXR) emission observable during solar flares was investigated. The observed HXR spectra are thought to be evidence of a higher-than-usual population of high energy electrons, which are thought to be a result from electron acceleration in the flare region. This electrons race down on magnetic field lines towards chromosphere and generate Langmuir waves. This Langmuir wave generation and subsequent re-absorption results in an overall increased number of electrons in the high energy tail of the distribution function. In particular, the work presented here aimed to investigate the role of the background density gradient and its effect on the overall acceleration mechanism. This was achieved by use of 3D fully relativistic, electromagnetic particle-in-cell (PIC) simulations with realistic ion to electron mass ratio. Previous studies in this field were extended in the following way: i) Ref.[37] is a collisional quasi-linear study that showed the importance of background plasma density gradients. This thesis extends Ref.[37] by the use of a self-consistent approach; ii) Ref.[35] offered a fully kinetically self-consistent investigation, but did not take background plasma density gradients into account. It was extended by introducing such gradients. A beam of accelerated electrons was injected into a magnetised, maxwellian, homogeneous and inhomogeneous background plasma. The monoenergetic beam formed a bump in the forward direction of the electron distribution function in phase space. The distribution was shown to be unstable to the beam-plasma instability, resulting in Langmuir wave growth. The waves were shown to be generated at the intersection of the dispersion relation of Langmuir waves with the beam resonance condition. In line with quasi-linear theory, the electron distribution relaxed by formation of a plateau. For a ubiquitous beam injection, three background density profiles of different gradient strengths were investigated: i) a constant background density; ii) a weak gradient, $n_{e,R}/n_{e,L} = 3$; iii) a strong gradient, $n_{e,R}/n_{e,L} = 10$, where $n_{e,L}$ and $n_{e,R}$ denote densities on the left and right edge of the simulation box. It was shown that the strongest gradient showed the maximum amount of electrons accelerated beyond $15v_{th}$. The weak gradient showed a slight increase compared to the constant density case.
Further, injection of a localized beam was studied in order to check whether or not

the wave power of generated waves drift to lower wavenumbers, as shown in Ref.[37]. The localized beam was injected into a constant background plasma as well as the strong gradient case. It was shown that there is a clear drift in wavenumber present in both cases, however, the strong gradient enhanced the drift. Despite the fact that the presented results aim at the HXR emission in the solar flare context, it is also likely to be relevant in the earth bow-shock [38, 58, 96].

The natural next step in this research would be the inclusion of collisions along with the 3D PIC simulations with background plasma density gradients. Ref.[37] and references therein show that the electron distribution function in phase space does show a power law behaviour rather than a distinct bump (which is the initial condition for all runs in this thesis), when the electrons are racing down from the flare region. Collisional processes allow the particles to lose their energies. The collision frequency is $\nu_c \propto 1/v^3$ allowing slower electrons to lose their energy faster. Consequently, the electron distribution function will form a bump on the collisional timescales. This however poses the question of how best to implement collisions, as the collisional timescales for solar parameters require very long run times, which can certainly not be achieved with the resources available to the author.

Bibliography

[1] M. J. Aschwanden. Particle acceleration and kinematics in solar flares - A Synthesis of Recent Observations and Theoretical Concepts (Invited Review). *Space Sci. Rev.*, 101:1–227, January 2002. doi: 10.1023/A:1019712124366.

[2] M. J. Aschwanden. *Physics of the Solar Corona. An Introduction with Problems and Solutions (2nd edition).* Chichester, UK: Praxis Publishing Ltd, 2005.

[3] T. S. Bastian, G. D. Fleishman, and D. E. Gary. Radio Spectral Evolution of an X-Ray-poor Impulsive Solar Flare: Implications for Plasma Heating and Electron Acceleration. *Astrophys. J.*, 666:1256–1267, September 2007. doi: 10.1086/520106.

[4] G. Bekefi and T. J. Orzechowski. Giant microwave bursts emitted from a field-emission, relativistic-electron-beam magnetron. *Physical Review Letters*, 37:379–382, July 1976. doi: 10.1103/PhysRevLett.37.379.

[5] N. Bello González, M. Franz, V. Martínez Pillet, J. A. Bonet, S. K. Solanki, J. C. del Toro Iniesta, W. Schmidt, A. Gandorfer, V. Domingo, P. Barthol, T. Berkefeld, and M. Knölker. Detection of Large Acoustic Energy Flux in the Solar Atmosphere. *Astrophys. J.*, 723:L134–L138, November 2010. doi: 10.1088/2041-8205/723/2/L134.

[6] R. F. Benson, P. A. Webb, J. L. Green, D. L. Carpenter, V. S. Sonwalkar, H. G. James, and B. W. Reinisch. Active Wave Experiments in Space Plasmas: The Z Mode. In J. W. Labelle and R. A. Treumann, editors, *Geospace Electromagnetic Waves and Radiation*, volume 687 of *Lecture Notes in Physics, Berlin Springer Verlag*, page 3, January 2006.

[7] C. K. Birdsall and A. B. Langdon. *Plasma Physics via Computer Simulation.* McGraw-Hill, New York, 1985.

[8] D. Biskamp. Anomalous resistivity and viscosity due to small-scale magnetic turbulence. *Plasma Physics and Controlled Fusion*, 26:311–319, January 1984. doi: 10.1088/0741-3335/26/1B/004.

[9] D. Biskamp. *Magnetohydrodynamic Turbulence.* February 2008.

[10] J. Boris. In *Proceedings of the Fourth Conference on Numerical Simulation Plasmas*, Washington, 1970. Naval Research Laboratory.

[11] J. C. Brown, R. Turkmani, E. P. Kontar, A. L. MacKinnon, and L. Vlahos. Local re-acceleration and a modified thick target model of solar flare electrons. *A&A*, 508:993–1000, December 2009. doi: 10.1051/0004-6361/200913145.

[12] P. K. Browning, M. Gordovskyy, A. Stanier, A. W. Hood, and S. Dalla. Flare particle acceleration and magnetohydrodynamic instabilities. *Plasma Physics and Controlled Fusion*, 53(12):124030, December 2011. doi: 10.1088/0741-3335/53/12/124030.

[13] I. H. Cairns and D. B. Melrose. A theory for the 2f(p) radiation upstream of the earth's bow shock. *Journal of Geophysical Research*, 90:6637–6640, July 1985. doi: 10.1029/JA090iA07p06637.

[14] P. J. Cargill, L. Vlahos, G. Baumann, J. F. Drake, and Å. Nordlund. Current Fragmentation and Particle Acceleration in Solar Flares. *Space Sci. Rev.*, 173: 223–245, November 2012. doi: 10.1007/s11214-012-9888-y.

[15] J. Chae, P. R. Goode, K. Ahn, V. Yurchysyn, V. Abramenko, A. Andic, W. Cao, and Y. D. Park. New Solar Telescope Observations of Magnetic Reconnection Occurring in the Chromosphere of the Quiet Sun. *Astrophys. J.*, 713:L6–L10, April 2010. doi: 10.1088/2041-8205/713/1/L6.

[16] G. D. Chagelishvili, A. D. Rogava, and D. G. Tsiklauri. Effect of coupling and linear transformation of waves in shear flows. *Phys. Rev. E*, 53:6028–6031, June 1996. doi: 10.1103/PhysRevE.53.6028.

[17] G. A. Dulk, T. S. Bastian, and G. Chanmugam. Radio emission from AM Herculis - The quiescent component and an outburst. *Astrophys. J.*, 273: 249–254, October 1983. doi: 10.1086/161363.

[18] A. G. Emslie, H. Kucharek, B. R. Dennis, N. Gopalswamy, G. D. Holman, G. H. Share, A. Vourlidas, T. G. Forbes, P. T. Gallagher, G. M. Mason, T. R. Metcalf, R. A. Mewaldt, R. J. Murphy, R. A. Schwartz, and T. H. Zurbuchen. Energy partition in two solar flare/CME events. *Journal of Geophysical Research (Space Physics)*, 109:A10104, October 2004. doi: 10.1029/2004JA010571.

[19] R. E. Ergun, C. W. Carlson, J. P. McFadden, G. T. Delory, R. J. Strangeway, and P. L. Pritchett. Electron-Cyclotron Maser Driven by Charged-Particle Acceleration from Magnetic Field-aligned Electric Fields. *Astrophys. J.*, 538: 456–466, July 2000. doi: 10.1086/309094.

[20] T. Z. Esirkepov. Exact charge conservation scheme for Particle-in-Cell simulation with an arbitrary form-factor. *Computer Physics Communications*, 135: 144–153, April 2001. doi: 10.1016/S0010-4655(00)00228-9.

[21] L. Fletcher and H. S. Hudson. Impulsive Phase Flare Energy Transport by Large-Scale Alfvén Waves and the Electron Acceleration Problem. *Astrophys. J.*, 675:1645–1655, March 2008. doi: 10.1086/527044.

[22] L. Fletcher, B. R. Dennis, H. S. Hudson, S. Krucker, K. Phillips, A. Veronig, M. Battaglia, L. Bone, A. Caspi, Q. Chen, P. Gallagher, P. T. Grigis, H. Ji, W. Liu, R. O. Milligan, and M. Temmer. An Observational Overview of Solar Flares. *Space Sci. Rev.*, 159:19–106, September 2011. doi: 10.1007/s11214-010-9701-8.

[23] A. Fossum and M. Carlsson. High-frequency acoustic waves are not sufficient to heat the solar chromosphere. *Nature*, 435:919–921, June 2005. doi: 10.1038/nature03695.

[24] H. P. Furth, J. Killeen, and M. N. Rosenbluth. Finite-Resistivity Instabilities of a Sheet Pinch. *Physics of Fluids*, 6:459–484, 1963. doi: 10.1063/1.1706761.

[25] D. E. Gary and G. J. Hurford. Solar radio burst spectral observations, particle acceleration, and wave-particle interactions. *Washington DC American Geophysical Union Geophysical Monograph Series*, 54:237–246, 1989.

[26] D. E. Gary, J. L. Linsky, and G. A. Dulk. An unusual microwave flare with 56 second oscillations on the M dwarf L726-8 A. *Astrophys. J. Lett.*, 263: L79–L83, December 1982. doi: 10.1086/183928.

[27] V. L. Ginzburg and V. V. Zhelezniakov. On the Possible Mechanisms of Sporadic Solar Radio Emission (Radiation in an Isotropic Plasma). *Soviet Astron.*, 2:653, October 1958.

[28] B. Gustafsson, B. Edvardsson, K. Eriksson, U. G. Jørgensen, Å. Nordlund, and B. Plez. A grid of MARCS model atmospheres for late-type stars. I. Methods and general properties. *Astron. Astrophys.*, 486:951–970, August 2008. doi: 10.1051/0004-6361:200809724.

[29] R. J. Hamilton and V. Petrosian. Stochastic acceleration of electrons. I - Effects of collisions in solar flares. *Astrophys. J.*, 398:350–358, October 1992. doi: 10.1086/171860.

[30] S. S. Hasan and A. A. van Ballegooijen. Dynamics of the Solar Magnetic Network. II. Heating the Magnetized Chromosphere. *Astrophys. J.*, 680:1542–1552, June 2008. doi: 10.1086/587773.

[31] M. A. Heald and C. B. Wharton. *Plasma Diagnostics With Microwaves*. New York: Krieger, 1978.

[32] J. D. Huba. *NRL Plasma Formulary*. Washington DC: Naval Research Laboratory, 2009.

[33] D. B. Jess, M. Mathioudakis, P. K. Browning, P. J. Crockett, and F. P. Keenan. Microflare Activity Driven by Forced Magnetic Reconnection. *Astrophys. J.*, 712:L111–L115, March 2010. doi: 10.1088/2041-8205/712/1/L111.

[34] W. Kalkofen. Wave heating of the solar chromosphere. *J. Astrophys. Astron.*, 29:163–166, March 2008. doi: 10.1007/s12036-008-0020-3.

[35] M. Karlický and E. P. Kontar. Electron acceleration during three-dimensional relaxation of an electron beam-return current plasma system in a magnetic field. *A&A*, 544:A148, August 2012. doi: 10.1051/0004-6361/201219400.

[36] E.-H. Kim, I. H. Cairns, and P. A. Robinson. Mode conversion of Langmuir to electromagnetic waves at magnetic field-aligned density inhomogeneities: Simulations, theory, and applications to the solar wind and the corona. *Physics of Plasmas*, 15(10):102110, October 2008. doi: 10.1063/1.2994719.

[37] E. P. Kontar, H. Ratcliffe, and N. H. Bian. Wave-particle interactions in non-uniform plasma and the interpretation of hard X-ray spectra in solar flares. *A&A*, 539:A43, March 2012. doi: 10.1051/0004-6361/201118216.

[38] V. V. Krasnoselskikh, T. Dudok de Wit, and S. D. Bale. Determining the wavelength of Langmuir wave packets at the Earth's bow shock. *Annales Geophysicae*, 29:613–617, March 2011. doi: 10.5194/angeo-29-613-2011.

[39] K. R. Lang. *The Cambridge Encyclopedia of the Sun*. August 2001.

[40] I. Lerche. Resistive Effects in the Turbulent Photosphere and Chromosphere. *Astrophys. & Space Sci.*, 10:486–499, March 1971. doi: 10.1007/BF00649691.

[41] R. P. Lin. The Emission and Propagation of 40 keV Solar Flare Electrons. I: The Relationship of 40 keV Electron to Energetic Proton and Relativistic Electron Emission by the Sun. *Solar Phys.*, 12:266–303, May 1970. doi: 10.1007/BF00227122.

[42] R. P. Lin and Rhessi Team. Rhessi observations of particle acceleration in solar flares. *Advances in Space Research*, 32:1001–1010, September 2003. doi: 10.1016/S0273-1177(03)00302-8.

[43] LOFAR. URL www.astron.nl.

[44] D. W. Longcope and C. C. Kankelborg. Coronal Heating by Collision and Cancellation of Magnetic Elements. *Astrophys. J.*, 524:483–495, October 1999. doi: 10.1086/307792.

[45] D. M. Malaspina, I. H. Cairns, and R. E. Ergun. The $2f_p$ radiation from localized Langmuir waves. *Journal of Geophysical Research (Space Physics)*, 115:A01101, January 2010. doi: 10.1029/2009JA014609.

[46] D. M. Malaspina, I. H. Cairns, and R. E. Ergun. Antenna Radiation near the Local Plasma Frequency by Langmuir Wave Eigenmodes. *Astrophys. J.*, 755:45, August 2012. doi: 10.1088/0004-637X/755/1/45.

[47] G. Mann, T. Classen, and H. Aurass. Characteristics of coronal shock waves and solar type II radio bursts. *A&A*, 295:775, March 1995.

[48] G. Mann, F. Jansen, R. J. MacDowall, M. L. Kaiser, and R. G. Stone. A heliospheric density model and type III radio bursts. *Astron. Astrophys.*, 348: 614–620, August 1999.

[49] D. J. McLean. Radioheliograph observations of harmonic type III solar bursts. *Australian Journal of Physics*, 24:201, February 1971.

[50] D. B. Melrose. *Instabilities in Space and Laboratory Plasmas*. August 1986.

[51] D. B. Melrose and G. A. Dulk. Electron-cyclotron masers as the source of certain solar and stellar radio bursts. *Astrophys. J.*, 259:844–858, August 1982. doi: 10.1086/160219.

[52] D. B. Melrose, R. G. Hewitt, and K. G. Ronnmark. Terrestrial kilometric radiation - The cyclotron theory. *J. Geophys. Res.*, 87:5140–5150, July 1982. doi: 10.1029/JA087iA07p05140.

[53] D. B. Melrose, G. A. Dulk, and R. G. Hewitt. Electron-cyclotron maser emission - Relative growth and damping rates for different modes and harmonics. *J. Geophys. Res.*, 89:897–904, February 1984. doi: 10.1029/JA089iA02p00897.

[54] D. Mihalas. *Stellar atmospheres /2nd edition/*. San Francisco: W. H. Freeman and Co., 1978.

[55] J. A. Miller, T. N. Larosa, and R. L. Moore. Stochastic Electron Acceleration by Cascading Fast Mode Waves in Impulsive Solar Flares. *Astrophys. J.*, 461: 445, April 1996. doi: 10.1086/177072.

[56] G. E. Moreton. Hα Observations of Flare-Initiated Disturbances with Velocities ˜1000 km/sec. *Astronom. J.*, 65:494, 1960. doi: 10.1086/108346.

[57] NASA. URL solarscience.msfc.nasa.gov.

[58] T. G. Onsager and R. H. Holzworth. Measurement of the electron beam mode in earth's foreshock. *J. Geophys. Res.*, 95:4175–4186, April 1990. doi: 10.1029/JA095iA04p04175.

[59] E. N. Parker. Dynamics of the Interplanetary Gas and Magnetic Fields. *Astrophys. J.*, 128:664, November 1958. doi: 10.1086/146579.

[60] R. Pechhacker and D. Tsiklauri. Electron cyclotron maser emission mode coupling to the z-mode on a longitudinal density gradient in the context of solar type III bursts. *Physics of Plasmas*, 19(11):110702, November 2012. doi: 10.1063/1.4769104.

[61] R. Pechhacker and D. Tsiklauri. The effect of electron beam pitch angle and density gradient on solar type III radio bursts. *Physics of Plasmas*, 19(11): 112903, November 2012. doi: 10.1063/1.4768429.

[62] R. Pechhacker and D. Tsiklauri. Three-dimensional particle-in-cell simulation of electron acceleration by Langmuir waves in an inhomogeneous plasma. *Physics of Plasmas*, 21(1):012903, January 2014. doi: 10.1063/1.4863494.

[63] P. L. Pritchett, R. J. Strangeway, C. W. Carlson, R. E. Ergun, J. P. McFadden, and G. T. Delory. Free energy sources and frequency bandwidth for the auroral kilometric radiation. *Journal of Geophysical Research*, 104:10317–10326, May 1999. doi: 10.1029/1998JA900179.

[64] J. C. Raymond, S. Krucker, R. P. Lin, and V. Petrosian. Observational Aspects of Particle Acceleration in Large Solar Flares. *Space Sci. Rev.*, 173:197–221, November 2012. doi: 10.1007/s11214-012-9897-x.

[65] M. J. Reiner, K. Goetz, J. Fainberg, M. L. Kaiser, M. Maksimovic, B. Cecconi, S. Hoang, S. D. Bale, and J.-L. Bougeret. Multipoint Observations of Solar Type III Radio Bursts from STEREO and Wind. *Solar Phys.*, 259:255–276, October 2009. doi: 10.1007/s11207-009-9404-z.

[66] P. A. Robinson and I. H. Cairns. Fundamental and Harmonic Emission in Type III Solar Radio Bursts - III. Heliocentric Variation of Interplanetary Beam and Source Parameters. *Solar Phys.*, 181:429–437, August 1998.

[67] J. I. Sakai, T. Kitamoto, and S. Saito. Simulation of Solar Type III Radio Bursts from a Magnetic Reconnection Region. *Astrophys. J.*, 622:L157–L160, April 2005. doi: 10.1086/429665.

[68] H. Schmitz and D. Tsiklauri. The effect of initial conditions on the electromagnetic radiation generation in type III solar radio bursts. *Physics of Plasmas*, 20(6):062903, June 2013. doi: 10.1063/1.4812453.

[69] C. J. Schrijver, J. Cote, C. Zwaan, and S. H. Saar. Relations between the photospheric magnetic field and the emission from the outer atmospheres of cool stars. I - The solar CA II K line core emission. *Astrophys. J.*, 337:964–976, February 1989. doi: 10.1086/167168.

[70] J. D. Scudder. Ion and electron suprathermal tail strengths in the transition region: Support for the velocity filtration model of the corona. *Astrophys. J.*, 427:446–452, May 1994. doi: 10.1086/174155.

[71] R. R. Sharma and L. Vlahos. Comparative study of the loss cone-driven instabilities in the low solar corona. *Astrophys. J.*, 280:405–415, May 1984. doi: 10.1086/162006.

[72] A. Y. Shih, R. P. Lin, and D. M. Smith. RHESSI Observations of the Proportional Acceleration of Relativistic ¿0.3 MeV Electrons and ¿30 MeV Protons in Solar Flares. *Astrophys. J. Lett.*, 698:L152–L157, June 2009. doi: 10.1088/0004-637X/698/2/L152.

[73] S. K. Solanki. Solar Cycle Variation of Chromospheric Radiation. In P. Heinzel, I. Dorotovič, & R. J. Rutten, editor, *The Physics of Chromospheric Plasmas*, volume 368 of *Astronomical Society of the Pacific Conference Series*, pages 481–+, May 2007.

[74] J. O. Stenflo. Distribution functions for magnetic fields on the quiet Sun. *Astron. Astrophys.*, 517:A37+, July 2010. doi: 10.1051/0004-6361/200913972.

[75] T. H. Stix. *The Theory of Plasma Waves*. 1962.

[76] A. Taflove and S. Hagness. *Computational Electrodynamics*. Artech House, 3rd edition, 2005.

[77] D. L. Tang, A. P. Sun, X. M. Qiu, and P. K. Chu. Interaction of electromagnetic waves with a magnetized nonuniform plasma slab. *IEEE Transactions on Plasma Science*, 31:405–410, June 2003. doi: 10.1109/TPS.2003.811648.

[78] A. M. Title, T. D. Tarbell, K. P. Topka, S. H. Ferguson, R. A. Shine, and SOUP Team. Statistical properties of solar granulation derived from the SOUP instrument on Spacelab 2. *Astrophys. J.*, 336:475–494, January 1989. doi: 10.1086/167026.

[79] C. Torrence and G. P. Compo. A Practical Guide to Wavelet Analysis. *Bulletin of the American Meteorological Society*, 79:61–78, January 1998. doi: 10.1175/1520-0477(1998)079⟨0061:APGTWA⟩2.0.CO;2.

[80] F. Trintchouk, M. Yamada, H. Ji, R. M. Kulsrud, and T. A. Carter. Measurement of the transverse Spitzer resistivity during collisional magnetic reconnection. *Physics of Plasmas*, 10:319–322, January 2003. doi: 10.1063/1.1528612.

[81] D. Tsiklauri. The Sun as a MHD generator: application of a new heating mechanism for the coronal loops and closed magnetic structures. *Astron. Astrophys.*, 441:1177–1181, October 2005. doi: 10.1051/0004-6361:20053167.

[82] D. Tsiklauri. A mechanism for parallel electric field generation in the MHD limit: possible implications for the coronal heating problem in the two stage mechanism. *Astron. Astrophys.*, 455:1073–1080, September 2006. doi: 10.1051/0004-6361:20064816.

[83] D. Tsiklauri. An alternative to the plasma emission model: Particle-in-cell, self-consistent electromagnetic wave emission simulations of solar type III radio bursts. *Physics of Plasmas*, 18(5):052903, May 2011. doi: 10.1063/1.3590928.

[84] D. Tsiklauri. Particle acceleration by circularly and elliptically polarised dispersive Alfven waves in a transversely inhomogeneous plasma in the inertial and kinetic regimes. *Physics of Plasmas*, 18(9):092903, September 2011. doi: 10.1063/1.3633531.

[85] D. Tsiklauri. Three dimensional particle-in-cell simulation of particle acceleration by circularly polarised inertial Alfven waves in a transversely inhomogeneous plasma. *Physics of Plasmas*, 19(8):082903, August 2012. doi: 10.1063/1.4745614.

[86] D. Tsiklauri and R. Pechhacker. Heating of solar chromosphere by electromagnetic wave absorption in a plasma slab model. *Physics of Plasmas*, 18(4): 042901, April 2011. doi: 10.1063/1.3581052.

[87] D. Tsiklauri, J.-I. Sakai, and S. Saito. Particle-In-Cell simulations of circularly polarised Alfvén wave phase mixing: A new mechanism for electron acceleration in collisionless plasmas. *A&A*, 435:1105–1113, June 2005. doi: 10.1051/0004-6361:20042436.

[88] J. E. Vernazza, E. H. Avrett, and R. Loeser. Structure of the solar chromosphere. III - Models of the EUV brightness components of the quiet-sun. *Astrophys. J. Supl. Ser.*, 45:635–725, April 1981. doi: 10.1086/190731.

[89] I. I. Vintizenko, A. I. Zarevich, and S. S. Novikov. Relativistic magnetron with distributed output of microwave radiation. *Technical Physics Letters*, 31: 388–390, May 2005. doi: 10.1134/1.1931776.

[90] A. J. Willes and I. H. Cairns. Generalized Langmuir waves in magnetized kinetic plasmas. *Physics of Plasmas*, 7:3167–3180, August 2000. doi: 10.1063/1.874180.

[91] R. M. Winglee. Fundamental and harmonic electron cyclotron maser emission. *J. Geophys. Res.*, 90:9663–9674, October 1985. doi: 10.1029/JA090iA10p09663.

[92] R. M. Winglee and G. A. Dulk. The electron-cyclotron maser instability as a source of plasma radiation. *Astrophys. J.*, 307:808–819, August 1986. doi: 10.1086/164467.

[93] C. S. Wu and L. C. Lee. A theory of the terrestrial kilometric radiation. *Astrophys. J.*, 230:621–626, June 1979. doi: 10.1086/157120.

[94] C. S. Wu and X. M. Qiu. Emissions of second-harmonic auroral kilometric radiation. *J. Geophys. Res.*, 88:10072–10080, December 1983. doi: 10.1029/JA088iA12p10072.

[95] K. Yee. Numerical solution of inital boundary value problems involving maxwell's equations in isotropic media. *IEEE Transactions on Antennas and Propagation*, 14:302–307, May 1966. doi: 10.1109/TAP.1966.1138693.

[96] P. H. Yoon, C. S. Wu, A. F. Vinas, M. J. Reiner, J. Fainberg, and R. G. Stone. Theory of 2 omega$_{pe}$ radiation induced by the bow shock. *J. Geophys. Res.*, 99:23481, December 1994. doi: 10.1029/94JA02489.

[97] S. Yu, J. G. Doyle, A. Kuznetsov, G. Hallinan, A. Antonova, A. L. MacKinnon, and A. Golden. Electron-beam-induced Radio Emission from Ultracool Dwarfs. *Astrophys. J.*, 752:60, June 2012. doi: 10.1088/0004-637X/752/1/60.

[98] Chengxun Yuan, Zhongxiang Zhou, Xiaoli Xiang, Hongguo Sun, and Shaozhi Pu. Propagation of broadband terahertz pulses through a dense-magnetized-collisional-bounded plasma layer. *Physics of Plasmas*, 17(11):113304, 2010. doi: 10.1063/1.3515895.

[99] V. V. Zharkova, K. Arzner, A. O. Benz, P. Browning, C. Dauphin, A. G. Emslie, L. Fletcher, E. P. Kontar, G. Mann, M. Onofri, V. Petrosian, R. Turkmani, N. Vilmer, and L. Vlahos. Recent Advances in Understanding Particle Acceleration Processes in Solar Flares. *Space Sci. Rev.*, 159:357–420, September 2011. doi: 10.1007/s11214-011-9803-y.

[100] V. V. Zharkova, N. S. Meshalkina, L. K. Kashapova, A. T. Altyntsev, and A. A. Kuznetsov. Effect of a self-induced electric field on the electron beam kinetics and resulting hard X-ray and microwave emissions in flares. *Geomagnetism and Aeronomy*, 51:1029–1040, December 2011. doi: 10.1134/S0016793211080329.